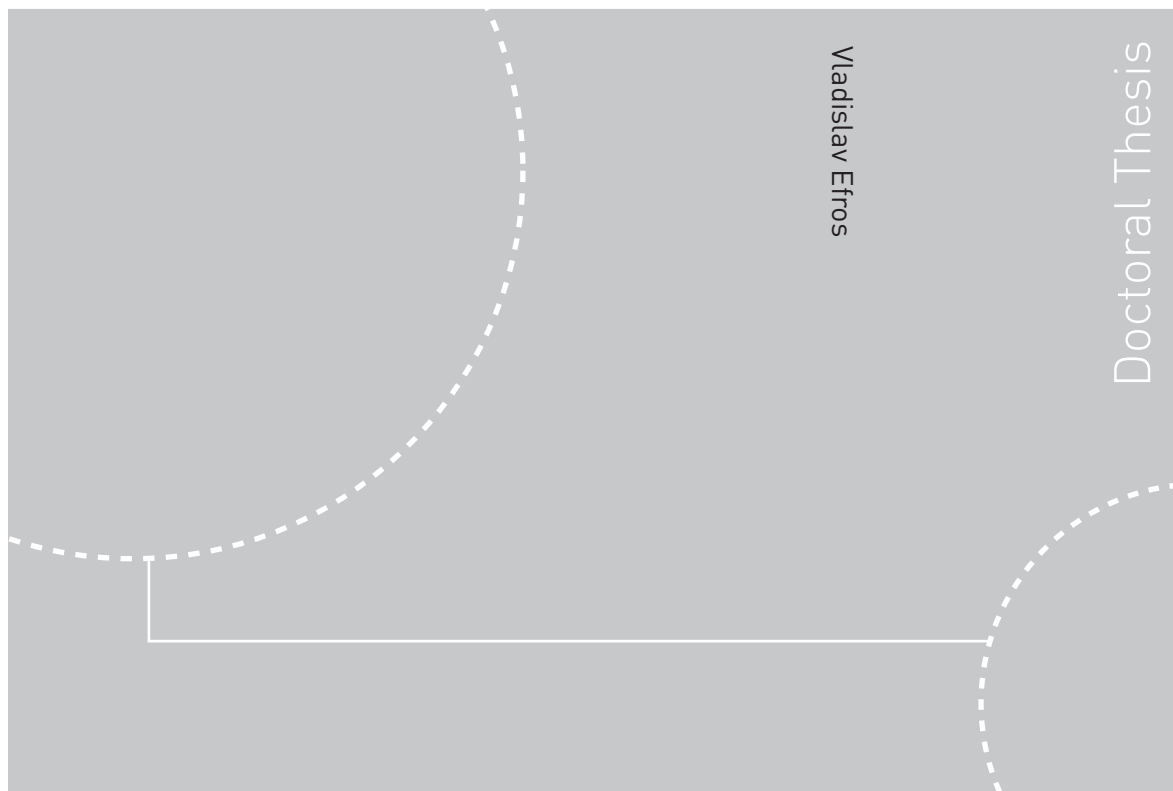


ISBN 978-82-471-2654-7 (printed ver.)
ISBN 978-82-471-2655-4 (electronic ver.)
ISSN 1503-8181



Doctoral theses at NTNU, 2011:64

Vladislav Efros
**Structure of turbulent boundary
layer over a 2-D roughness**

Doctoral theses at NTNU, 2011:64

NTNU
Norwegian University of
Science and Technology
Thesis for the degree of
philosophiae doctor
Faculty of Engineering Science and Technology
Department of Energy and Process Engineering

Vladislav Efros

Structure of turbulent boundary layer over a 2-D roughness

Thesis for the degree of philosophiae doctor

Trondheim, February 2011

Norwegian University of
Science and Technology
Faculty of Engineering Science and Technology
Department of Energy and Process Engineering



NTNU

Norwegian University of Science and Technology

Thesis for the degree of philosophiae doctor

Faculty of Engineering Science and Technology
Department of Energy and Process Engineering

©Vladislav Efros

ISBN 978-82-471-2654-7 (printed ver.)
ISBN 978-82-471-2655-4 (electronic ver.)
ISSN 1503-8181

Doctoral Theses at NTNU, 2011:64

Printed by Tapir Uttrykk

Abstract

The roughness is an important parameter in wall-bounded flows, as most surfaces are rough. The main effect of the roughness is to increase the drag as the near wall is affected by the roughness. In recent years a lot of efforts has been used to find out what effect has the roughness on the outer layer. In other words is there any differences in outer layer, boundary layer or channel flow, between rough and smooth-surface?

Jimenez (2004) suggests that for $\delta/k > 40$ there are no differences, in agreement with Townsend's hypothesis, the roughness merely acts to increase the surface stresses, without changing the structure in the flow.

This was challenged by Krogstad *et. al* (1999) who showed, for boundary layer over $2 - D$ roughness, there is a difference in the outer layer due to the roughness. However for a channel flow Krogstad *et. al* (2004) has found no differences.

The main impediment is how to obtain a reliable estimate for the friction velocity, u_τ , which is the main scaling parameter of principal interest. In channel flow the u_τ may be obtained directly from the stream-wise pressure gradient. A common technique for boundary layer over smooth surface is the Clauser chart. This method is subjected to large uncertainties for rough surface, because the number of unknowns is increased from one, C_f , for smooth surface to three, (C_f, ϵ , the shift in origin and $\Delta u/u_\tau$ shift in velocity), for rough surface.

The need for an independent measurement of the wall shear stress has led to the present work.

A floating-balance has been designed to obtain the shear stress on the rough surface. The balance was tested in channel flow, adverse pressure gradient flow and zero pressure gradient boundary layer and the velocity field was investigated using a two-component LDA system. The results showed that the shear stress, from balance, was underestimated by $\sim 4\%$.

Turbulent boundary layer is a complicated nonlinear system; Clauser (1956) compared it with a black box. A better understanding of this system may be obtained by changing one of its inputs and to examine its output.

An experimental investigation on the response of a turbulent boundary layer to sudden change in roughness, from smooth to rough, using floating balance to measure the shear stress is also a part of the present work.

The structure of the turbulent boundary layer over $2 - D$ roughness was inves-

tigated using LDA and PIV system. All the moments up to third order were determined from the LDA measurements. From the PIV measurements two-point correlations in $x - y$ plane were obtained. The effect of large scales on the features of the flow-using POD was also investigated.

Keywords

Floating-element, LDA, Internal boundary layer, high-order moments, PIV, POD.

Acknowledgments

I would like to express my thanks to my supervisor, Prof. Per-Åge Krogstad for all his support and guidance throughout these years. His practical ideas, during the period of building the balance, have been most valuable.

I would also like to thank John Krogstad and Arnt Egil Kolstad, laboratory staff, for helping me to build all kind of devices necessary for the experimental part of this work.

Special thanks to Prof. Hyung Jin Sung and Assoc. Prof. Philipp Schaltter for providing the DNS data.

I also want to thank my colleagues for their help in the lab and for all the good time we had together.

Finally, I would like to thank my family for their love and support during this time. Most of all I would like to express my gratitude to Elen for her patience and love, no matter what.

Nomenclature

Roman

a, b, d distances

A_1, A_2 area

A_{xz} projected area of the floating element in xz plane

B, C constants

c thickness of the gap

C_f skin friction coefficient, $C_f = 2 (u_\tau / U_e)^2$

D width of the floating element, $D=50$ mm

E recovered energy from POD modes

F shear force, $F = \tau_w \cdot A_{xz}$

F_α flatness of component α

F_N force measured by balance

F_p pressure force

G Clauser's shape parameter

g gap between the moving plate and surrounding wall

H shape parameter, $H = \theta / \delta^*$

h channel half height

K calibration constant

k hight of the roughness, $k = 1.7$ mm

L Length of the floating element, $L=350$ mm

L_F lip force

Lx_{pp}	length of R_{pp} in x direction
Ly_{pp}	length of R_{pp} in y direction
M	number of snapshots
M^*	size of the step change, $M^* = z_{01}/z_{02}$
N	normal force
N_{pod}	number of leading POD modes
q	kinetic energy, $q = 1/2 u_i u_i$
R_{pq}	two-point correlation of fluctuating components p and q
R_{uv}	correlation coefficient, $R_{uv} = \langle -uv \rangle / (\sigma_u \sigma_v)$
Re_θ	Reynold number based on the momentum thickness, θ
S_α	skewness of component α
u	stream wise velocity
U_e	free stream velocity
u_τ	friction velocity, $u_\tau = \sqrt{\tau_w / \rho}$
$u_L^{(n)}(x, y)$	reconstructed velocity field from the N leading POD modes
$u_R^{(n)}(x, y)$	residual velocity field
X	distance from the step to the measurement point
z_0	roughness length, for a rough surface $z_0 = (v/u_\tau) \exp[-\kappa(A + \Delta U/u_\tau)]$

Greek letters

β	non-dimensional pressure gradient
ΔP	pressure drop
ΔU^+	vertical shift of the logarithmic curve
ΔX	length
Δ	Clauser's thickness for turbulent layers, $\Delta = \delta^* U_e / u_\tau$
δ	boundary layer thickness, defined as y for which $u = 0.99 U_e$
δ^*	displacement thickness

δ_i	thickness of internal boundary layer
ϵ	shift in origin
κ	von Karman constant=0.41
λ	roughness spacing
λ_{ci}	swirling strength
λ_i	eigenvalue from POD
λ_s	swirling strength with assigned sign based on ω_z
ν	kinematic viscosity of the air
$\omega(\Pi, y/\delta)$	wake function
ω_z	vorticity in (x,y) plane
ϕ_i	POD modes
Π	wake strength
ρ	density of the air
σ_p	standard deviation of component p
τ	total shear stress
θ	momentum thickness
k_s	equivalent sand grain roughness
y	spatial coordinate in spanwise direction

Superscripts

+	normalized with u_τ
p	coefficient in Elliot's formula

Subscripts

l, m	number of velocity components in a snapshot
p, q	general index

Abbreviations

<i>IBL</i>	internal boundary layer
------------	-------------------------

LDA Laser Doppler Anemometry

PIV Particle Image Velocimetry

POD Proper orthogonal decomposition

Contents

Abstract	i
Acknowledgments	iii
1 Introduction	1
1.1 Rough boundary layer	1
1.1.1 The boundary layer concept	1
1.1.2 Boundary layer over smooth surface	2
1.1.3 Boundary layer over rough surface	3
1.2 Skin Friction measurement	5
1.2.1 Direct measurement	5
1.2.2 Momentum balance	6
1.2.3 Wall similarity technique	7
1.3 The response of turbulent boundary layer to sudden perturbations	8
1.3.1 Sudden change in roughness	9
1.4 Motivation	10
1.5 References	11
2 A Skin Friction Balance	13
2.1 Description of the balance	13
2.2 Results	19
2.3 Discussion and Conclusions	24
2.4 References	25
3 Turbulent boundary layer over a step change: smooth to rough. LDV measurements	27
3.1 Experimental set-up	27
3.1.1 Wall-shear stress	29
3.2 Results	31
3.2.1 Mean flow	31
3.2.2 Internal Boundary layer	40
3.2.3 Reynolds stresses	43
3.2.4 Transport equation for Reynolds stresses	50
3.2.5 Higher-order Moments	51

3.2.6	Skewness and Flatness	57
3.2.7	Quadrant decomposition	62
3.2.8	Conclussions	68
3.3	References	69
4	Turbulent boundary layer over a step change: smooth to rough. PIV measurements	73
4.1	Experimental set-up	73
4.2	Results	75
4.2.1	Validation of mean profiles	75
4.2.2	Effects of spatial resolution	79
4.2.3	Two-point correlations	84
4.2.4	Swirling Strength	96
4.2.5	Proper orthogonal decomposition analysis	102
4.2.6	Conclussions	115
4.3	References	116
5	Summary and Conclusions	119
A	List of articles	123

Chapter 1

Introduction

1.1 Rough boundary layer

1.1.1 The boundary layer concept

The concept of boundary layer was introduced by Prandtl and defined as - a thin layer of fluid adjacent to the solid surface within which the viscous effects are dominant. The velocity near the wall is smaller than at a large distance from it. The thickness of this layer is increasing along the flat plate in the downstream region (Schlichting (1968)). The velocity distribution over a flat plate is shown schematically in Figure (1.1). The boundary layer is a thin layer of retarded flow

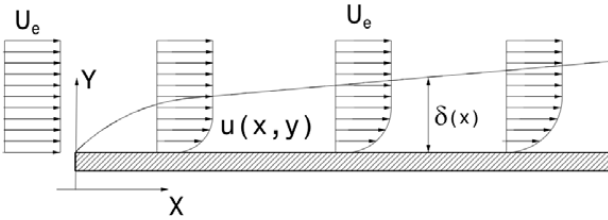


Figure 1.1: Boundary layer over a flat plate (sketch)

of thickness δ which increases from the leading edge in the downstream direction. The nominal thickness, δ , is the distance at which the velocity is $0.99U_e$, U_e being the free stream velocity. The velocity approaches U_e asymptotically and δ is not very easy to measure. Therefore the ill-defined δ is substituted by more precisely defined momentum thickness, θ , or displacement thickness, δ^* .

The displacement thickness, δ^* , is the displacement of the streamlines from the wall compared to inviscid solution, in order to obtain the same mass rate of flow as in the real case. From Figure (1.2) the δ^* can be defined:

$$\int_0^\infty u dy = \int_{\delta^*}^\infty U_e dy \Rightarrow \delta^* = \int_0^\infty \left(1 - \frac{u}{U_e}\right) dy \quad (1.1)$$

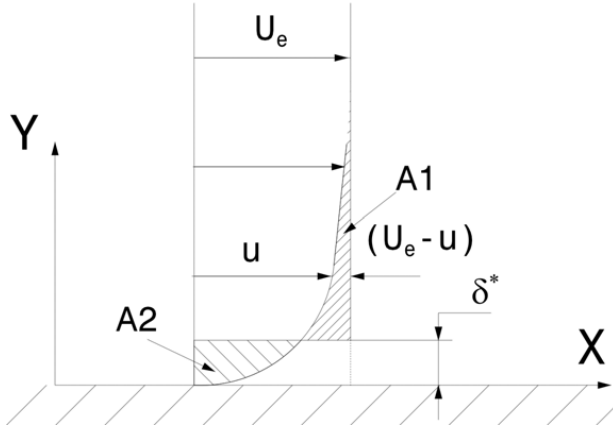


Figure 1.2: Displacement thickness (sketch)

From Figure (1.2) follows that the area A1 is equal with area A2. The momentum thickness, θ , is defined as:

$$\rho U_e^2 \theta = \rho \int_0^\infty (U_e - u) dy \Rightarrow \theta = \int_0^\infty \frac{u}{U_e} \left(1 - \frac{u}{U_e}\right) dy \quad (1.2)$$

All of these thicknesses depend on the shape of velocity distribution. The ratio between the momentum thickness and displacement thickness is called the shape parameter, H .

$$H = \frac{\theta}{\delta^*} \quad (1.3)$$

1.1.2 Boundary layer over smooth surface

The main goal of the present work is to study the structure of the boundary layer over rough-surface but it is good to have an overview over boundary layer in zero pressure gradient over a smooth surface. The boundary layer over smooth surface must be divided into two regions; the inner region in which the viscosity is an important parameter and outer region where flow is independent of the viscosity. In the immediate vicinity of the wall we have

$$\frac{U}{u_\tau} = \frac{y \cdot u_\tau}{\nu} \quad (1.4)$$

where

$$u_\tau = \sqrt{\frac{\tau_{wall}}{\rho}} \quad (1.5)$$

Further from the wall we have the logarithmic law of the wall

$$\frac{U}{u_\tau} = \frac{1}{\kappa} \ln \left(\frac{y \cdot u_\tau}{\nu} \right) + B \quad (1.6)$$

This is universal in the inner layer which for flat plate boundary layer is considered as $y/\delta < 0.2$.

For the outer layer, log region, exist a universal relation between $(U_e - u/u_\tau)$ and y/δ as

$$\frac{U_e - u}{u_\tau} = \frac{1}{\kappa} \ln \left(\frac{y}{\delta} \right) + C \quad (1.7)$$

Outside the log region we have:

$$\frac{U_e - u}{u_\tau} = f \left(\frac{y}{\delta} \right) \quad (1.8)$$

The Karman constant, $\kappa \sim 0.41$ is considered to be universal. The constants B and C are different from author to author, this might be connected with not enough information about turbulent boundary layer.

1.1.3 Boundary layer over rough surface

Practically all surfaces are rough. The first rough-wall flow analysis was conducted by Nicuradze (1933), who investigated the flow in sand-roughened pipes. He found that the flow depended on the relative scale of the roughness k/d (k is roughness scale and d pipe diameter) as well as the Reynolds number (Perry *et al*). Flow dependent on k/d was termed *fully rough* while the flow dependent on both k/d and Reynolds number was termed *transition flow*.

The main effect of the roughness is to increase the friction coefficient, C_f , and to shift data with the ΔU^+ compared to smooth data as shown in Figure (1.3) where ΔU^+ is the vertical shift of the logarithmic curve caused by the roughness and has the form (Clauser 1956)

$$\Delta U^+ = \frac{1}{\kappa} \ln \left(\frac{k u_\tau}{\nu} \right) + const. \quad (1.9)$$

Over either smooth or a rough wall the turbulent boundary layer consists of an outer region (Raupach *et al.*) where the length scale is the boundary layer thickness, δ , and a wall or inner region where the length scale is ν/u_τ for smooth wall and ν/u_τ together with k to characterize the rough wall. The velocity profiles for rough and smooth-surface in outer coordinates are shown in Figure (1.4). The main conclusion from Figure (1.3) and Figure (1.4) is that

- in inner coordinates there is a region where the velocity profile is logarithmic as for the smooth surface but shifted with a value ΔU^+

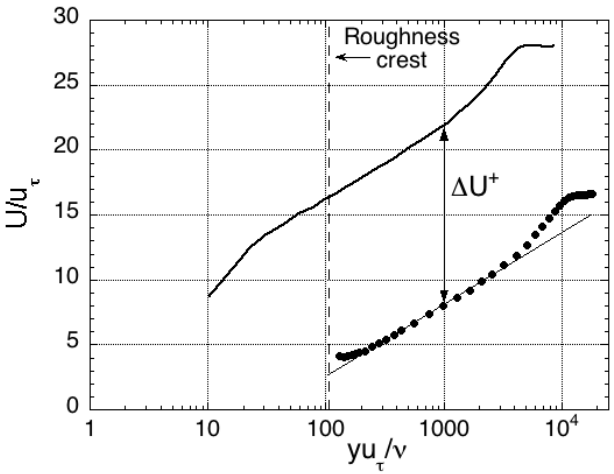


Figure 1.3: Velocity profile in inner coordinates

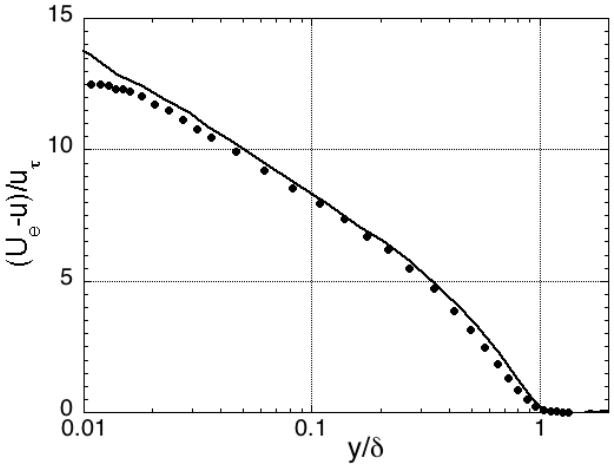


Figure 1.4: Velocity profile in outer coordinates

- in outer coordinates the equation (1.7) is valid for both smooth and rough surface this indicate that the flow is similar in outer layer.

How is that possible a flow with different structure in inner layer could be similar in outer layer?

$U(y)$ is a function of y no doubt but we should be careful in defining the origin of y for rough wall. The origin of y can be taken anywhere between the crest of the roughness and the valley of roughness. The distance, ϵ , defines the origin of y for profiles that will give a logarithmic distribution near the wall (Perry *et al*).

1.2 Skin Friction measurement

Any object moving through a fluid experiences a drag that can be decomposed in pressure drag and skin friction drag. The problem of estimating turbulent skin friction is important in many applications, such as aerospace research or the structure of turbulent boundary layer. The shear stress is an important parameter for the normalization of the velocity profiles. Only with accurate measurement of the shear stress it is possible to establish reliable data for comparison with numerical simulations or models.

Several methods for measuring the shear stress in the wall have been developed. There is not a universal method to measure skin-friction because each problem requires a specific geometry to be adapted and different techniques apply better in different cases. Winter shows a review of the techniques used from 1940 to 1975 and range conditions required on each case. The modern developments are presented by Naughton & Sheplak. The principal skin-friction techniques are:

- Direct measurement
- Liquid tracers
- Momentum balance
- Wall similarity technique
- Microelectromechanical systems (MEMS) technique
- Thin-oil-film techniques

1.2.1 Direct measurement

Direct measurement is a method, which gives the shear stress directly without any assumptions about the flow. The skin friction balance is a direct measurement of the skin friction. This is very simple and well established technique but with many problems in practical application. A principle sketch of skin friction balance is shown in Figure (1.5). The force due to flow with velocity U acting on the balance,

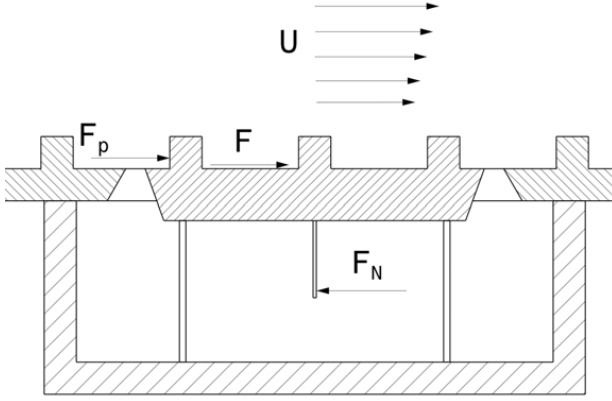


Figure 1.5: Floating element

for rough surface, consist of a frictional force F , $F = \tau_w \cdot A_{xz}$, where τ_w is the wall shear stress acting on the surface of the balance A_{xz} and the pressure forces acting on the frontal area of the roughness, F_p . What we measure is the force F_N or the displacement of the floating element. Usually the measured force is determined as

$$F_N = K \cdot (\tau_w \cdot A_{xz} + F_p) \quad (1.10)$$

where K is a calibration constant, which is determined by applying known loads and measuring the displacement or the force of the floating element.

The main problems (Winter 1977), which should be considered:

- A device to measure very small forces or displacements
- The effect of the gaps around the floating element
- Forces arising from the pressure gradients
- The effects of misalignment of the floating element
- Effects of temperature changes and vibrations from the tunnel
- Effects of leaks

1.2.2 Momentum balance

For the flows in constant area ducts, such as channels or pipes the wall shear stress can be obtained from the pressure gradient.

$$\tau_{wall} = \frac{1}{2} \frac{\Delta P}{\Delta X} h \quad (1.11)$$

where h is either the pipe radius or channel height, ΔP is the pressure drop over a length ΔX (Haritonidis 1989). This method is limited because it applies to a rather special type of flow and because the flow should be fully developed. However it is ideal for calibration. (see Haritonidis 1989)

The application of the momentum balance to developing flow is less satisfactory. In principle it is simple you have to use the momentum integral equation and to solve for τ_{wall} . The main drawback is that the equation contains some derivatives (Brown & Joubert 1969) of slowly varying quantities, such as the momentum thickness of the boundary layer. These derivatives are very difficult to be determined accurately.

1.2.3 Wall similarity technique

It has been accepted that near the wall, for smooth wall and $y^+ < 5$, the velocity distribution is given by $U^+ = y^+$ and hence the value of the skin friction can be determined. This implies that we should measure very close to the wall in the viscous sub-layer. This sub-layer is very thin for high Reynolds number so the velocity cannot be determined correctly. Instead the logarithmic region is used. The log-law for smooth surface is presented below:

$$\frac{U}{u_\tau} = \frac{1}{\kappa} \ln \left(\frac{y u_\tau}{\nu} \right) + B \quad (1.12)$$

The main problem with equation 1.12 is the universality of constants, κ and B . The equation 1.12 is determined from the dimensional analysis while the constants κ and B are determined experimentally. Several authors have challenged the constants κ and B , Österlund & Johansson determined $\kappa=0.38$ and $B=4.1$.

The log law for rough surface, which is different from the meteorological community, may be written

$$\frac{U}{u_\tau} = \frac{1}{\kappa} \ln \left(\frac{[y + \epsilon] u_\tau}{\nu} \right) + B - \Delta U^+ \quad (1.13)$$

Here ϵ is the shift in origin of the effective wall location and ΔU^+ is the shift in the log law due to the roughness effect on the mean flow. The two additional unknowns, ϵ and ΔU^+ , for rough surface makes the fitting procedure more challenging. If u_τ is determined in an independent way, this will decrease the uncertainty of the remaining two variables in the fitting procedure.

Other methods using the wall similarity technique are:

- Heat transfer
- Mass transfer
- Preston tubes

- Stanton tubes

More details about these methods can be obtained from Winter (1977).

The MEMS and thin-oil-film techniques are discussed in details in Naughton & Sheplak (2002). Most of the measurement techniques were developed on the base of smooth surface. If roughness is included then most of technique fail due to the measurement principle used or the impossibility to accommodate to the new geometric condition.

Most of the friction for rough surface is due to pressure drag. For simple roughness geometry, the pressure drag can be measured by pressure tap on one or more roughness elements. This was done by Perry *et al.* (1969) and by Antonia & Luxton (1971) for square transverse bars. For a more general rough surface it is necessary to use a balance to measure the force acting on a small area of surface. The direct measurement of skin friction on a rough surface was performed earlier by Karlsson (1980) or Acharya *et al* (1986).

1.3 The response of turbulent boundary layer to sudden perturbations

The turbulent boundary layer involve a complex combination of phenomena, the relatively simple case is the constant pressure boundary layer (Clauser 1956). We are interested to know what happens to the flow when the boundary layer is subjected to a sudden perturbation. The flow subjected to sudden perturbations is very often observed in nature. For example, when breezes encounter the coastline, the sudden change in roughness can have an important effect on the flow (Smits & Wood 1985). Another possible perturbations can be a sudden change in pressure gradient or the curvature of the surface, blowing or suction of the flow applied along a surface to control the flow. Apart from the practical reasons; the study of behavior of a perturbed boundary layer is a way for better understanding of the structure of turbulent boundary layer. The mechanism of the boundary layer is very complicated and difficult to understand. Our goal is to try to understand it by applying a sudden perturbation and to try to see what is the response to this imposed condition. Following Tani (1968) there are two methods of introducing the perturbations into boundary layer:

- The perturbation is applied as a sudden change in pressure or of a wall roughness
- The perturbation is introduced of an obstacle in the flow or by the application of injection or suction over a short region of the wall

1.3.1 Sudden change in roughness

Surface roughness can change from smooth to rough or rough to smooth. The work presented in this thesis is connected with the perturbation as a sudden change of a wall roughness, from smooth to rough.

The change in surface roughness is presented in Figure (1.6). When the turbulent

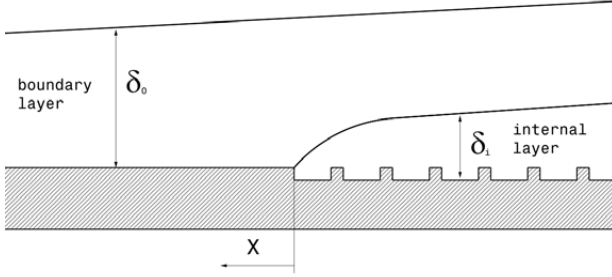


Figure 1.6: Sudden change in roughness

boundary layer flow run over a discontinuity in roughness is not anymore in equilibrium. The region affected by the step change in roughness is called internal boundary layer, δ_i . The boundary layer, upstream the step, is considered to be fully developed and described by the equation (see Smits & Wood 1985):

$$\frac{U}{u_\tau} = \frac{1}{\kappa} \ln \left(\frac{y}{z_0} \right) \quad (1.14)$$

where z_0 is the roughness length. For a smooth wall we have:

$$z_{0_{smooth}} = \left(\frac{\nu}{u_\tau} \right) \exp [-\kappa B] \quad (1.15)$$

For a rough surface,

$$z_{0_{rough}} = \left(\frac{\nu}{u_\tau} \right) \exp \left[-\kappa \left(B + \frac{\Delta U}{u_\tau} \right) \right] \quad (1.16)$$

The size of the step change can be measured by $M^* = z_{01}/z_{02}$, Smits & Wood (1985), or by $M = \ln M^*$, where 1 and 2 refers to the upstream and downstream values. For $M < 0$ we have a step change from smooth to rough and for $M > 0$ we have a step change from rough to smooth.

According to Wood (1981) a general correlation for δ_i after a step change in roughness for zero pressure gradient boundary layer is

$$\frac{\delta_i}{z_0} = f_1 \left(M^*, \frac{X}{z_0} \right) \quad (1.17)$$

where X is the distance from the step; z_0 can be either z_{01} or z_{02} . The equation (1.17) applies for the near wall region where δ_i/δ less than 0.2. Another correlation

assuming that $\delta_i \sim x^n$ is

$$\frac{\delta_i}{z_0} = f_2(M^*) \left(\frac{X}{z_0} \right)^n \quad (1.18)$$

At the small scales in the atmosphere, and in the wind tunnel (Garratt (1990)), the internal boundary layer is found to grow as $\sim x^{4/5}$, for a smooth to rough transition and slightly slower growth for the rough to smooth flow.

1.4 Motivation

The roughness is very important parameter for wall-bounded flows. The main effect of the roughness, as mentioned above, is to increase the skin friction and to shift data with ΔU^+ . Although a lot of experiments have been done, one of the first being Nikuradze, the boundary layer over rough surface is far from being elucidated.

The boundary layer over smooth or rough walls consists of outer and inner layer. According to Townsend's hypothesis the turbulence outside the roughness sublayer is unaffected by surface condition. This implies that the Reynolds stresses (Flack *et al.* 2005) normalized with u_τ are universal outside the roughness sub-layer. The roughness sub-layer extends $\sim (3-4)k$ from the wall. This is supported by Flack *et al.* (2005), mesh and sand grain roughness, Volino *et al.* (2007), Wu & Christensen (2007), wall with replicated turbine blade roughness.

For $2-D$ roughness, $k=1.7$ mm and $\lambda/k=8$, Lee & Sung (2007) DNS, Volino *et al.* (2009) have found changes in the turbulence in the outer layer which is consistent with Krogstad & Antonia (1999), $\lambda/k=4$, λ is the roughness spacing.

Following the Jiménez (2004) for $k \ll \delta$ and $k/\delta > 40$ the wall similarity is expected. The similarity is expected when scaling with u_τ which is very difficult to determine correctly. The use of Clauser plot, is subjected to large uncertainties (Acharya *et al.* 1986) because the number of variables to be determined from fitting procedure are: ϵ , ΔU^+ and C_f compared with one, C_f , for smooth surface. To decrease the uncertainty it is necessary to have an independent measurement of C_f .

The development of a floating element for rough surface, which allows to measure independently the C_f , followed by the measurement of the structure of rough turbulent boundary layer using laser Doppler anemometry, LDA, and particle image velocimetry, PIV, will be addressed in present thesis.

1.5 References

- I. Tani, Review of some experimental results on the response of a turbulent boundary layer to sudden perturbations,
Computation of turbulent boundary layers 1968 FOSR-IFR-Stanford Conference. Volume I, (1968), pp. 483-494
- A. J. Smits & D. H. Wood, The response of turbulent boundary layers to sudden perturbations, *Annu. Rev. Fluid Mech* **17**, (1985), pp. 321-358
- D. H. Wood, Internal boundary layer growth following a step change in surface roughness, *Boundary Layer Meteorology* **22**, (1982), pp. 241-244
- J. R. Garratt, The internal boundary layer- a review, *Boundary Layer Meteorology* **50**, (1990), pp. 171-203
- H. Schlichting, Boundary-Layer Theory, *Sixth Edition*
- A. E. Perry, W. H. Schofield, & P. N. Joubert, Rough wall turbulent boundary layers, *J. Fluid Mech* **37**, (1969), pp. 383-413
- M. R. Raupach, R. A. Antonia & S. Rajagopalan, Rough-wall turbulent boundary layers, *Applied Mechanics Reviews* **44**, no 1, (1991), pp. 1-25
- R. J. Volino, M. P. Schultz & K. A. Flack, Turbulence structure in a boundary layer with two-dimensional roughness, *J. Fluid Mech* **635**, (2009), pp. 75-101
- J. W. Naughton, M. Sheplak, Modern developments in shear-stress measurement, *Progress in Aerospace Science* vol **38**, (2002), pp. 515-570
- R. A. Antonia and R. E. Luxton, The response of a turbulent boundary layer to a step change in surface roughness. Part 1. Smooth to rough *J. Fluid Mech*, **48**, part 4, (1971), pp. 721-761
- S. Dhawan, Direct Measurements of Skin Friction, Report 1121
- J. H. Haritonidis, The measurement of Wall Shear Stress, *Advances in Fluid Mechanics Measurements*, **45**, (1989), pp. 229-261
- K. C. Brown & P. N. Joubert, The measurement of skin friction in turbulent boundary layers with adverse pressure gradients, *J. Fluid Mech*, **35**, part 4, (1969), pp. 737-757

Chapter 2

A Skin Friction Balance

The main problem that slowed down the understanding of the roughness effect on the flow has been the difficulty to measure the skin friction. This quantity is very important because it represents the main scaling parameter. In addition, for the rough surface an independent measurement of u_τ is essential for accurate determination of the $\Delta u/u_\tau$ and shift in origin, ϵ .

This led to the development of the skin-friction balance and a set of measurements to investigate how accurate u_τ can be measured.

2.1 Description of the balance

We spent around three years in our endeavor to build a balance to measure shear stress for our rough wall. At the beginning it was a classical balance with springs and non-contact sensor or laser displacement sensor to measure the displacement of the floating element. The main problems with sensors were too much drift and low sensitivity. The main challenge with the balance is the electronic part because the forces or displacements are very small.

The system was designed around a standard, off the shelf, laboratory balance. The balance is shown in the Figure (2.1). The device is a single-pivot type and consists of two main parts:

- The sensing element, which consists of a replica of the test surface (1) is mounted on a thin plate. We have developed our balance for channel flow and two-dimensional boundary layer applications taking advantage of the spanwise homogeneity, so the sensing element is a rectangle with dimensions (DxL) 50x350mm in the streamwise and spanwise directions, respectively. The test plate is mounted on a vertical frame (2), which rests on a knife edge (6). Through the lower part of the frame is an adjustable horizontal bar (3) with two counter weights. The force is then transmitted to the sensing element through the adjustable vertical arm (4). By varying the ratio between arms (2) and (3) the "gain" of the system may be varied. Also

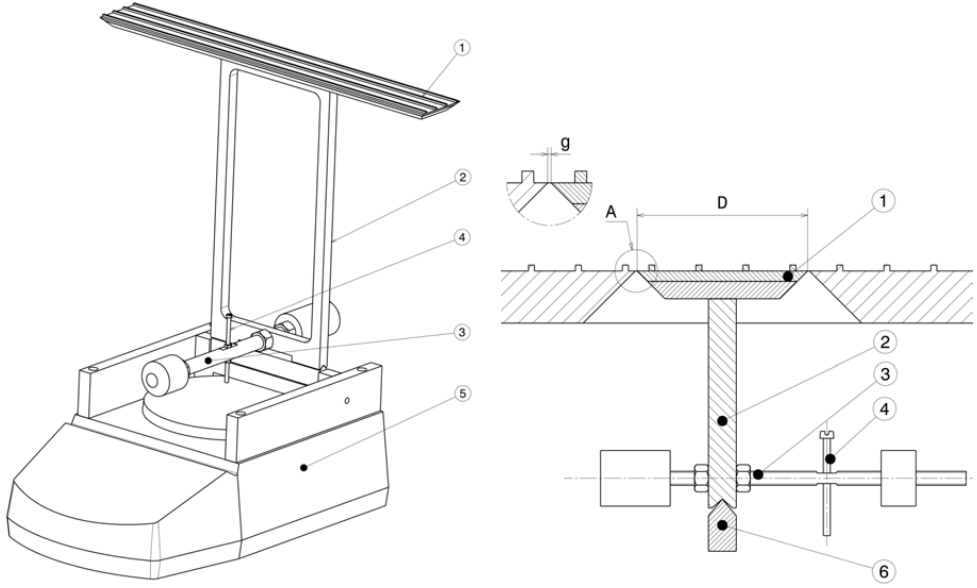


Figure 2.1: The skin friction balance.

balancing counter weights have been used to preload the sensing element of the balance to ensure that the balance always operates in its linear range.

- The balance (5) is a commercial force sensing unit from Ohaus with a sensitivity of 0.001g. Normal loads are of the order of 12g and for these loads the vertical motion of the sensing unit was less than 100 μm as measured using a micrometer dial gauge. The output from the balance was sampled on a computer through a RS232 connection.

In unloaded condition the sensing element was centered in the slot cut in the floor of the wind tunnel. The gap, g , between the movable plate and the surrounding wall was nominally 0.6mm and $g/D \sim 0.012$.

Figure (2.2) shows the setup of the balance in wind tunnel. The whole balance could be positioned very accurately by means of three screws (3) controlling the vertical movement and two screws (1) that could be used to shift the balance in the horizontal plane. In addition the balance (5), Figure (2.1), has two more screw for fine adjustment in vertical direction

Figure (2.3) presents a sketch of the forces acting on the floating element, friction force, F , lip force, L_F , normal force, N , force due to the pressure on frontal area of roughness, F_p , and the force measured by balance, F_N . Following Allen (1976), the sum of moments about the moment center, the following equation was obtained:

$$F_N = \frac{a}{b} \left[F_p \cdot \left(1 + \frac{k}{2a} \right) + F + N \cdot \frac{d}{a} + \left(1 - \frac{c}{2a} \right) \cdot L_F \right] \quad (2.1)$$

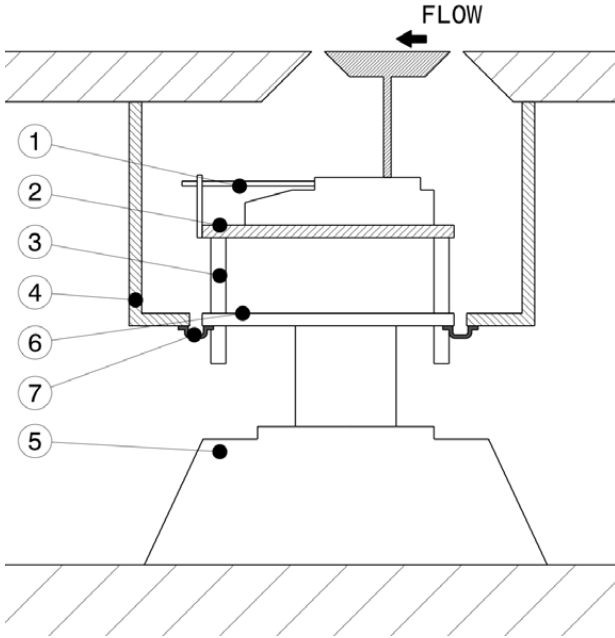


Figure 2.2: The balance setup

The first two terms in equation 2.1 are the terms we want to measure, the first term is zero for a smooth wall, for a rough wall the ratio $F_p/F > 1$, this indicate that the main contribution to skin friction for rough wall is due to the pressure drag. The last two terms, representing the normal force and the lip force, should be zero for an ideal case. Thus this balance measure the total drag due to the pressure and the skin friction drag. The last two terms are main source of errors assuming that the calibration is perfect.

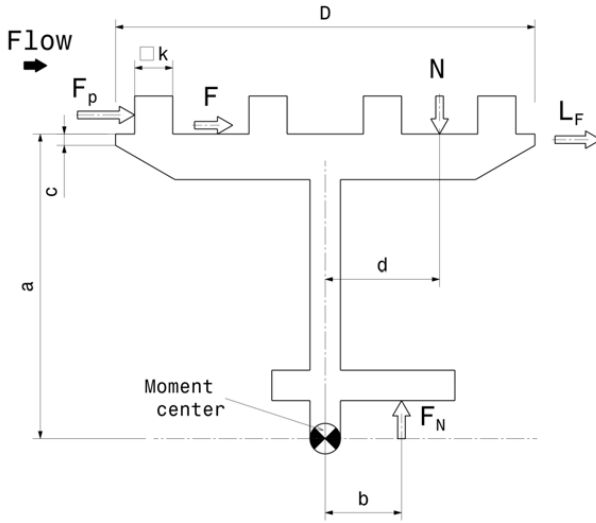


Figure 2.3: Forces acting on floating element

Because the balance is a single-pivot type, any normal force that does not pass through the pivot point will create a moment in addition to that from the skin friction. The moment due to the normal force, N , are different from zero in two cases:

- If the pressure above and below the floating element are not equal (Allen (1976))
- because the balance is a pivot type, any misalignment, $d \neq 0$, will create a momentum due to gravity force.

The moment due to normal force is not very big because the arm, d , usually is very small compared with the length, a , arm for skin friction force.

Under ideal condition, when the protrusion is zero and the flow through the gap around the floating element (Allen (1976)) and the surrounding surface is null, the pressure around the floating element is constant creating no net force on the lip. As long as there is a flow through the gap a net force will be created.

In order to reduce the effects of any flow through the gaps, the balance was mounted in a sealed box (4) fitted under the test surface; see Figure (2.2). To minimize the effect of structural vibrations, a gap exists between the box (4) and the plate (6); see Figure (2.2). This gap is sealed with a polyethylene film (7), Figure (2.2).

The lip force is mainly function of the protrusion of the element above and below the surface. In our case we kept are negative protrusion of ~ 0.06 mm which should be negligible in our case because we have a thick boundary layer (see Allen (1977)). We have a relatively big gap and this turns in our advantage because as

Allen (1977) proved that the balance is less sensitive to protrusion errors at the larger gaps.

The pressure variation across the floating element will create a force in the direction of the skin friction force (see Hakkinen 2004), acting on the sides of the floating element (Figure (2.4)). Hakkinen (2004) has shown that the relative error caused by gap forces can be written as:

$$\varepsilon = \frac{(dp/dx) \cdot D \cdot c}{\tau_w \cdot D} = \frac{(dp/dx) \cdot c}{\tau_w} \quad (2.2)$$

where τ_w is the shear force, $(dp/dx \cdot c \cdot D)$ is the net force, c and D are the thickness of the gap and the length of the floating element. The main conclusion from the equation (2.2) is that the relative error is direct proportional with the gap depth c . This explains why we have a sharp edge on the floating element and the surface around the element (Figure 2.1). This is equivalent to $c \sim 0.1 \text{ mm}$ see Figure (2.3).

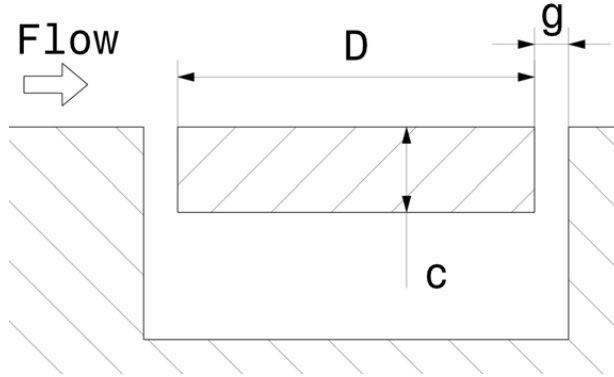


Figure 2.4: Gap forces.

The balance was calibrated in situ in the wind tunnel. The main problem in calibrating the balance was to generate a force, which is acting parallel with the sensing element. Using a calibrating device constructed in a similar way as the arms of the balance, except that it was inverted, solved this problem. The calibration device is presented in Figure (2.5). A frame (1), balanced by the weights (7), mounted on knife-edge supported by frame (2), which sits on the rough wall (4), is in contact with the floating element (5) through the arm (6). The vertical arm has a sharp edge at one end, which is in contact with one bar from the floating element. The container (3) is loaded with known masses necessary for calibrating. In this way the calibration device is transferring the vertical force due to weights to a force in the horizontal direction. The geometry of the calibration device doesn't change during the calibration because the displacement of the floating element is negligible.

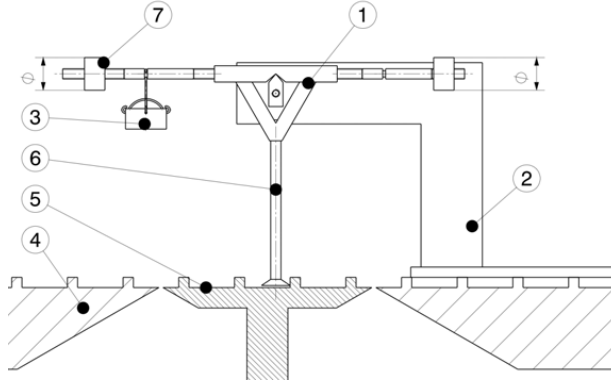


Figure 2.5: The calibration device.

The calibration curve obtained in this way is shown in Figure (2.6). The calibrated output is seen to be very linear with very little scatter. The ratio between the arms (2) and (3) in Figure (2.1) was adjusted to be close to 5:1 and this may be seen to be reflected in the five times higher output from the balance. The linear calibration

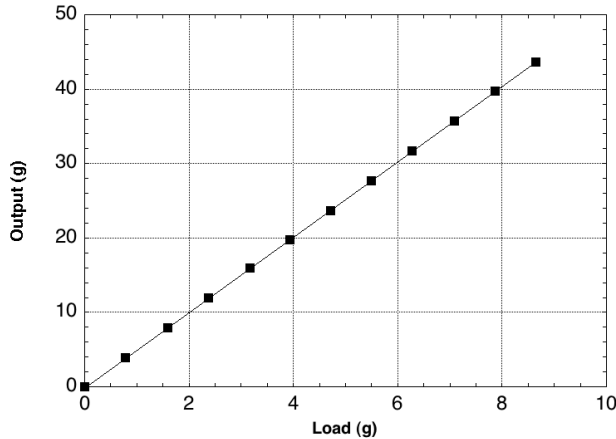
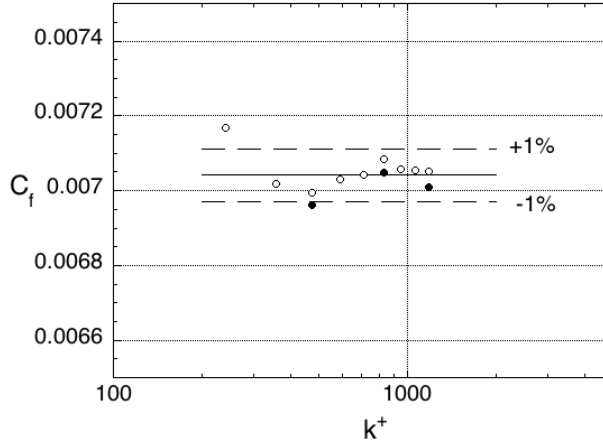


Figure 2.6: The calibration curve.

function fitted to the data was found to have a scatter typically better than 0.34% of full load.

Figure (2.7) shows the C_f as function of k^+ . For fully rough conditions, $k^+ > 60$, the C_f should be constant. The differences between the averaged value, solid line in Figure (2.7), and measured values, not for the first point, are $\sim \pm 1\%$. The differences for the first point is $\sim 2\%$ this is connected with the fact that the measured force, $F=0.0051$ N, is too small.

Figure 2.7: C_f versus k^+ .

2.2 Results

The main source of error is the pressure gradients (Hakkinen 2004); any small pressure gradient could be a significant source of error by creating a pressure difference between upstream and downstream gaps. To check the performances, the balance was exposed to three different pressure gradients.

The experiments were conducted in a closed return wind tunnel. Both the ceiling and the floor was covered with square rods $1.7 \times 1.7 \text{ mm}^2$. The pitch-to height ratio $\lambda/k = 8$ which correspond to "k-type roughness". In addition the upper wall of the wind tunnel is adjustable.

Measurements of velocity field was performed using a Dantec two-components fiber-optic Laser Doppler Anemometry (LDA). In order to do near-wall measurements the probe was tilted at a small angle. The flow was seeded with small particles provided by Safex smoke generator. A total of 100 000 random velocity samples were obtained in coincidence mode for each location during the measurements. The probe was traversed to approximately 30 locations for case 1 and 40 locations for case 2 and 3. All the measurements were taken above the crest of the roughness elements.

To determine the u_τ the balance was used. The data from balance was sampled as long as velocity measurement. The moving average of the data from balance was in the limit of $\pm 0.4\%$.

The variation of the non-dimensional pressure gradient (2.3) is shown in Table 2.2.

$$\beta = h \cdot \frac{1}{\rho \cdot u_\tau^2} \cdot \left| \frac{\Delta P}{\Delta x} \right| \quad (2.3)$$

The first experiment was fully developed channel flow as in Krogstad *et al* (2005).

Table 2.2: Parameters for experiment. The symbols used for the plots.

Case	h [mm]	β	$\Delta P/\Delta x$	C_f	Symbol
1	50	1.027	< 0	0.0148	■
2	300	6.203	> 0	0.0048	●
3	210	0.083	≈ 0	0.0067	Δ

The channel half height was $h=0.05$ m. Being a fully developed channel flow the wall shear stress is easy to obtain by simply measuring the pressure drop along the channel and compared with the wall shear derived from the balance.

$$\tau_{w_{ch}} = h \cdot \frac{\Delta P}{\Delta x} \quad (2.4)$$

where h is the half channel height and dP/dx is the pressure gradient. To measure the pressure-drop, the test section is fitted with taps in the sidewall and along the centerline of the floor.

The axial mean-momentum equation for channel flow is:

$$-\frac{1}{\rho} \frac{dP}{dx} + \nu \frac{d^2 U}{dy^2} - \frac{d}{dy} \langle uv \rangle = 0 \quad (2.5)$$

The integration of equation (2.5) from 0 to y

$$-\frac{y}{\rho} \frac{dP}{dx} - \frac{\tau_w}{\rho} + \left[\nu \frac{dU}{dy} - \langle uv \rangle \right] = 0 \quad (2.6)$$

$$-\frac{1}{u_\tau^2} \frac{y}{\rho} \frac{dP}{dx} - 1 + \left[\frac{dU^+}{dy^+} - \langle uv^+ \rangle \right] = 0 \quad (2.7)$$

where superscript (+) means normalized with the shear stress, u_τ , and the viscous length scale, ν/u_τ . The non-dimensional pressure gradient, β , can be included in equation 2.7 and to obtain:

$$-\langle uv \rangle^+ = 1 + \beta \cdot \left(\frac{y^+}{h^+} \right) - \frac{dU^+}{dy^+} \quad (2.8)$$

For a fully developed channel flow β should be 1, but combining the pressure gradient obtained from the taps and the shear stress obtained from balance, β was found to be slightly higher than one, 1.027. This indicate that the combined error in pressure and shear stress of less than 3%. The expected error from equation (2.2) is 0.2%.

For the adverse pressure-gradient we raised the roof, from $2h=280$ mm to $2h=600$ mm at the exit, to form a diffuser. The angle of the diffuser was around 3.0 degrees. This allowed flow to develop under an adverse pressure gradient. There is no equilibrium condition in this case, so the only verification that can be used is that the normalized shear stress extrapolates to one at the wall.

The last was the zero pressure gradient boundary layer. To obtain almost a zero pressure-gradient flow we changed the rough surface roof with a smooth surface roof and lifted the roof to avoid any interference between the boundary layer on the floor and roof of the tunnel. The roof was adjusted to obtain a zero pressure gradient. The mean velocity profiles for the three cases plotted in inner variables are shown in Figure (2.8). All cases show a linear log region with a different magnitude of wake strength. For the channel flow the shift was found to be, $\Delta U^+ \sim 15$ for $k^+ = 210$, the shift for adverse pressure gradient, $k^+ = 107$, and boundary layer, $k^+ = 116$, was found to be almost the same, $\Delta U^+ \sim 14.4$.

The normal stresses in outer coordinates are shown in Figure (2.9) and Figure

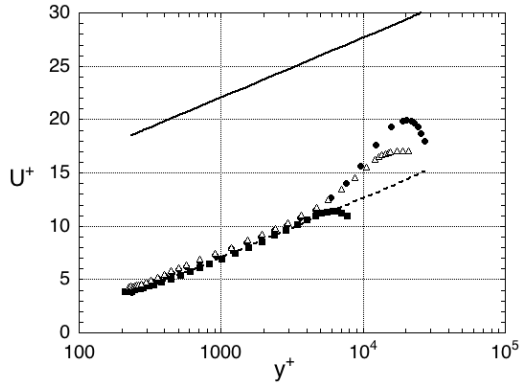


Figure 2.8: Mean velocity, U^+ . – smooth, -- $\Delta U^+ = 15$ Symbols as in Tab.2.2.

(2.10). The stresses, at centerline, are independent of the pressure gradient in the channel. The $\langle uu \rangle^+$ and $\langle vv \rangle^+$, for adverse pressure gradient, are increased throughout most of the outer layer compared with the channel and boundary layer. This is due to the increased turbulence production away from the wall in the case of the adverse pressure gradient. Figure (2.8) indicates that the slope, dU^+/dy , for adverse pressure is higher than for channel and boundary layer in the outer layer. Combined with the increase in $-\langle uv \rangle^+$ in the outer layer, Figure (2.11), this increases the production term for $\langle uu \rangle^+$ which indirectly increase the $\langle vv \rangle^+$. The shear stress profiles are shown in Figure (2.11). For the channel flow we have added the theoretical linear distribution defined by equation (2.8). The agreement is quite good giving confidence to the direct drag measurements. For the adverse pressure gradient the shear stress is seen to grow linearly near the wall as expected and data extrapolates back to 1 at the wall when scaled with shear stress obtained from the balance. For the zero pressure gradient profile, Figure (2.12), we have included the shear stress computed using the method described

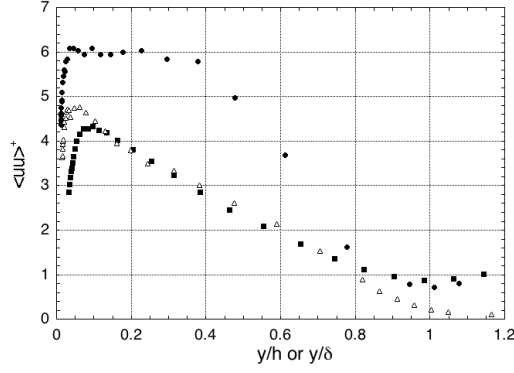


Figure 2.9: Normal stress, uu^+ . Symbols as in Tab.2.2

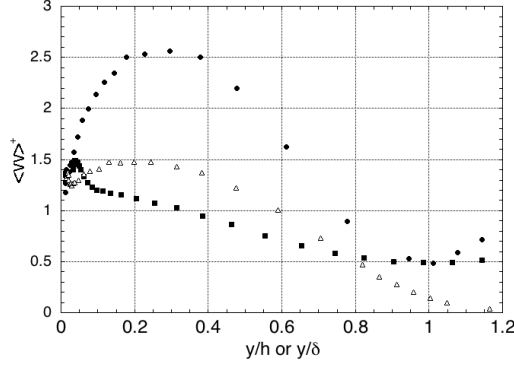


Figure 2.10: Normal stress, vv^+ . Symbols as in Tab.2.2

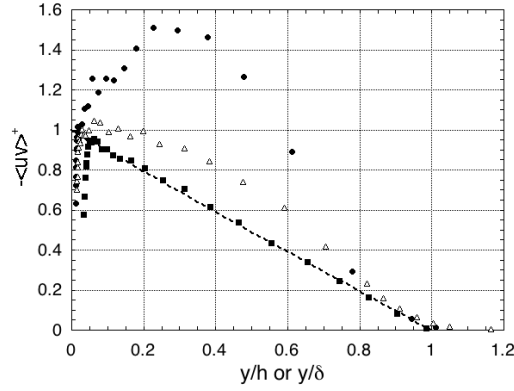


Figure 2.11: Shear stress, uv^+ . Symbols as in Tab.2.2

by Cebeci & Smith (1974),

$$\frac{\tau}{\tau_w} = \mu \cdot \frac{\partial U}{\partial y} - \rho \cdot \langle uv \rangle = 1 + \frac{\left(\int_0^\eta f^2 d\eta - f \int_0^\eta f d\eta \right)}{\int_0^1 f(1-f) d\eta} \quad (2.9)$$

where $f = U/U_e$ and $\eta = y/\delta$. A combined logarithmic law and a wake function was used to represent the mean velocity profile,

$$\frac{U}{u_\tau} = \frac{1}{\kappa} \ln \left(\frac{y u_\tau}{\nu} \right) + B + w \left(\Pi, \frac{y}{\delta} \right) \quad (2.10)$$

where $w(\Pi, y/\delta)$ is the outer wake function and Granville's function was used to represent $w(\Pi, y/\delta)$,

$$w \left(\Pi, \frac{y}{\delta} \right) = \frac{1}{\kappa} \left((1 + 6\Pi) \left(\frac{y}{\delta} \right)^2 - (1 + 4\Pi) \left(\frac{y}{\delta} \right)^3 \right) \quad (2.11)$$

The agreement between the analytical and measured curve is seen to be good.

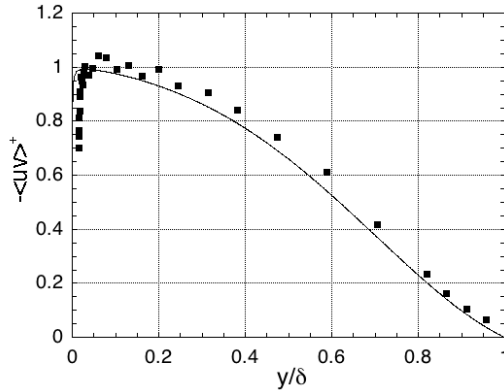
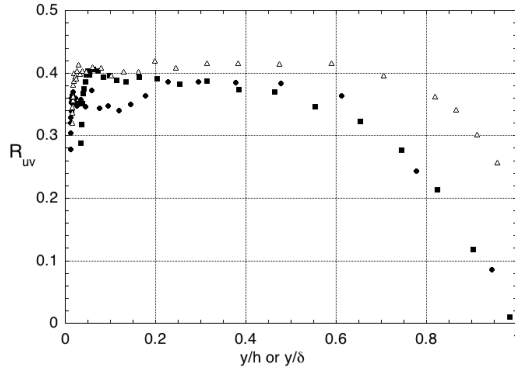


Figure 2.12: The shear-stress distribution, $\langle uv \rangle^+$. The ■ denotes measured data and the solid line denotes the analytical solution.

The correlation coefficient, $R_{uv} = -\langle uv \rangle / \sqrt{\langle uu \rangle \langle vv \rangle}$, looks almost identical for the three flows. The flow for channel and adverse pressure gradient collapse for $y/\delta > 0.2$ see Figure (2.13). This is in agreement with findings of Skåre & Krogstad (1994) that the correlation coefficient is very little affected by the pressure gradient effects.

Figure 2.13: The correlation R_{uv} . Symbols as in Table 2.2

2.3 Discussion and Conclusions

The flow developing along the same rough surface, under fully developed channel flow; an adverse pressure gradient and zero pressure gradient boundary layer conditions, was investigated using a two-component LDA system. The data acquired has been scaled with shear stress obtained from the direct measurement with a floating element.

For the channel flow the comparison was made with theoretical straight-line distribution, the agreement was quite good. For the adverse pressure gradient the data is increasing linearly near the wall and the data set extrapolates back to one at the wall when scaled with balance measurements. The measurements done for the channel flow and zero pressure gradient boundary layer indicate that the normalized shear stress are slightly higher than 1. This suggests that the combined error in the shear stress, determined with balance, and pressure measurements of $\sim 4\%$. The relative error for channel flow, ε , calculated with equation (2.2) and $c = 0.1 \text{ mm}$ is -0.2% while for adverse pressure gradient is $+2.1\%$.

The presented balance, on rough walls, has proven to give reliable results under different conditions. The balance has been used only for rough walls because the shear stress is considered higher than for smooth wall. The C_f obtained in adverse pressure gradient is almost twice the value expected for zero pressure gradient for smooth wall experiments. This imply that in order to get the same output for smooth wall we need to double the area of the floating element.

By using an "off the shelf" micro force measurement unit, with proven accuracy and stability, we have designed a balance with high accuracy and linearity. The results obtained from the balance are accurate and in good agreement with analytical solution.

Despite this, further experiments with smooth surface are needed to establish the source of errors.

2.4 References

- P.-Å. Krogstad, R.A. Antonia and L.W.B. Browne, Comparison between rough- and smooth-wall turbulent boundary layers, *J. Fluid Mech.* **245**, (1992), pp. 599–617
- P.-Å. Krogstad, and R.A. Antonia, Surface roughness effects in turbulent boundary layers, *Exp. Fluids* **27**, (1999), pp. 450–460
- L. Keirsbulck, L. Labraga, A. Mazouz, and C. Tournier, Surface roughness effects on turbulent boundary layer structure, *J. Fluids Eng.* **124**, (2002), pp. 127–135
- K.A. Flack, M.P. Schulz, and T.A. Shapiro, Experimental support for Townsend’s Reynolds number similarity, *Phys. Fluids* **17**, 035102, (2005)
- S.-H. Lee, and H.J. Sung, Direct numerical simulation of the turbulent boundary layer with rod-roughened wall, *J. Fluids Eng.* **584**, (2007), pp. 125–146
- P.-Å. Krogstad, H. I. Andersson, O.M. Bakken, and A. Ashrafian, An experimental and numerical study of channel flow with rough walls, *J. Fluid Mech.* **530**, (2005), pp. 327–352
- A. Acharya and M. P. Escudier, Measurements of the Wall Shear Stress in Boundary Layer Flows, *Turbulent Shear Flows* 4,(1980), pp. 277–286
- R. I. Karlsson, Studies of skin friction in turbulent boundary layers on smooth and rough walls, (1980)
- K. A. Flack, M. P. Schulz and J. S. Connelly, Examination of a critical roughness height for outlet layer similarity, *Phys. Fluids* **19** 095104, (2007)
- J. M. Allen, Experimental Study of Error Sources in Skin-Friction Balance Measurements, *Journal of Fluids Engineering* **99**, (1977), pp. 197–204
- R. J. Hakkinen, Reflections on Fifty Years of Skin Friction Measurement, *AIAA 2004-2111* pp. 1–13
- P. E. Skåre, P.-Å Krogstad, A turbulent equilibrium boundary layer near separation, *J. Fluid Mech.* **272**, (1994), pp. 319–348da
- H. Tennekes and J. L. Lumley, A First Course in Turbulence, *The MIT Press*, (1972)
- T. Cebeci and A. M. O. Smith, Analysis of turbulent boundary layers, *Academic Press, London*, (1974)

Chapter 3

Turbulent boundary layer over a step change: smooth to rough. LDV measurements

The interaction between the inner and outer layer in turbulent boundary layer is not well understood. A sudden change in roughness is used to study how a perturbation develops through the boundary layer and to see if it eventually changes the distributions of Reynolds stresses and high order moments in the outer layer.

3.1 Experimental set-up

The experiments were conducted in a closed return wind-tunnel. The upper wall is adjustable, which allows the adjustment of the pressure gradient. Because the height of the exit section after contraction is only 280 mm we had to adjust the upper wall as shown in Figure (3.1) with zero pressure gradient on the last half ($\sim 3\text{ m}$).

The experimental set-up being investigated consist of a rough wall, the same as used by Krogstad *et al.* (2005), covered with a thin plate Figure (3.1) to make a smooth wall followed by a rough wall of length $X + 200\text{ mm}$. The plate is placed on top of rough elements so that the top of roughness is below the smooth surface with 2 mm the thickness of the smooth plate.

For smooth wall case all the test section was covered with a smooth plate, $X = 0$ means smooth-surface. Decreasing the length of the smooth plate will increase the length, X , of the rough surface. This mean that the length of the smooth surface is decreasing while the length of the rough surface is increasing.

The leading edge of the smooth plate, as shown in Figure (3.1), is bent to create a small ramp for the flow. The boundary layer is allowed to transition naturally without any wire trip.

CHAPTER 3. TURBULENT BOUNDARY LAYER OVER A STEP CHANGE: SMOOTH TO ROUGH. LDV MEASUREMENTS

The experimental test conditions are given in Table (4.1). The rough surface is of the '*k - type*' with a pitch-to-height ratio of 8 and cross section $1.7 \times 1.7 \text{ mm}^2$. The length of the test section was about 6.4 m and all the measurements were taken at the same position $\sim 6.2 \text{ m}$ from the contraction.

Velocity measurements were obtained using a Dantec two-components fiber-optic Laser Doppler Velocimeter. In order to perform near-wall measurements the probe was tilted at a small angle ($\sim 5^\circ$). Additionally a $9.8 : 1$ beam expander was attached to the probe to reduce the size of the measurement volume. The size of the measuring volume: diameter (d) was $123 \mu\text{m}$ and length l of $1600 \mu\text{m}$. The corresponding dimensions in viscous units for $X = 0$ are $d^+ = 4.3$, $l^+ = 55.8$ and for $X = 5.66 \text{ m}$ are $d^+ = 7.4$, $l^+ = 95.7$.

The probe was traversed in vertical direction to approximately 35 positions using a Mitutoyo traverse. The data were collected in coincidence mode, 50 000 samples for $X = 0$ and 100 000 for $X > 0$. The flow was seeded with $\sim 1 \mu\text{m}$ smoke particles. All the measurements were taken above the crest of the roughness element as in the previous study of Krogstad *et al.* (2005).

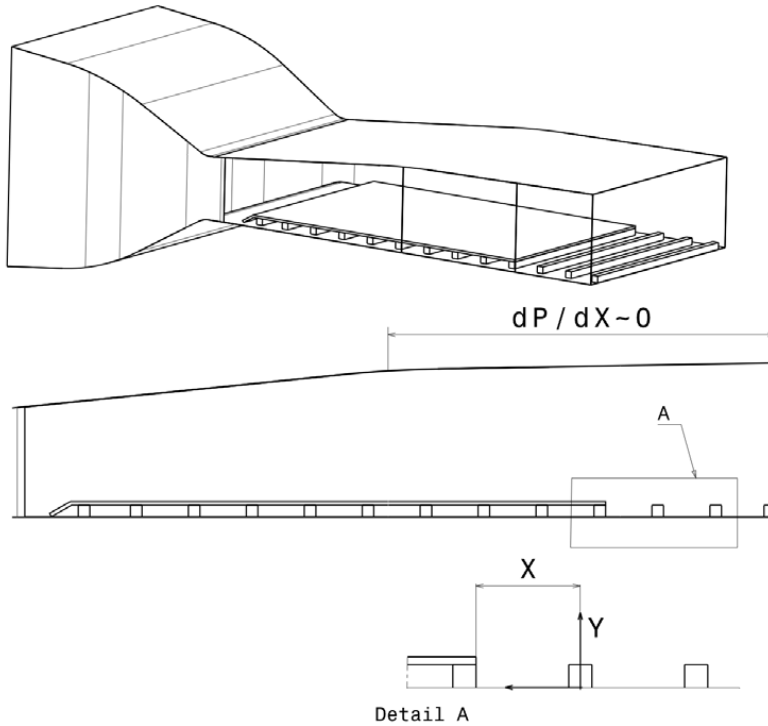


Figure 3.1: Geometry of the surface.

Table 3.1: Parameters for experiment. The symbols used for the plots.

Case	Symbol	X[m]	Wall	U_e	Re_θ	$C_f \times 10^{-3}$	δ^+	k^+	k_s^+/k^+
0	—	DNS	smooth	-	2400	3.39	-	-	-
1	•	0.00	smooth	14.6	13386	2.55	4203	-	-
2	▽	0.19	rough	14.5	14526	10.15	9045	117.3	9.1
3	□	0.70	rough	14.7	15824	9.46	9078	114.4	10.1
4	◇	1.20	rough	15.3	17922	8.38	8953	112.1	8.4
5	▣	1.70	rough	15.8	19187	8.24	8734	115.2	10.0
6	△	2.20	rough	15.2	20832	7.89	8704	106.7	13.3
7	○	2.70	rough	15.4	22094	7.95	9115	110.1	13.7
8	▣	3.20	rough	14.9	22353	7.85	9315	106.2	10.3
9	⊞	3.82	rough	15.3	24802	7.06	9911	103.1	10.9
10	⊠	4.82	rough	15.3	28384	7.28	12057	104.8	10.8
11	⊙	5.66	rough	15.4	32624	6.78	13292	101.6	12.2

3.1.1 Wall-shear stress

The major problem when analyzing rough surface boundary layer experiments is to determine the friction velocity correctly. There are few techniques for rough surfaces based on the modified Clauser plot. The main problem is a large uncertainty because the number of quantities to be determined, for rough surface, is high compared with smooth surface and in addition the method is based on the existence of the logarithmic region. To avoid all this uncertainties we have designed a floating element device (Efros & Krogstad (2009)) to measure the C_f for rough surfaces. The friction velocity on the smooth wall is determined by fitting data to log-law. The C_f obtained from the floating element device is shown in Figure (3.2). There is a sudden jump of C_f from smooth to rough surface, followed by a decrease towards a full rough-surface value. First the velocity field is slowed down by new surface condition and C_f is increasing. Then C_f is decreasing due to flow adjustment the new surface. The trend of C_f denotes that the flow is perturbed by the new surface.

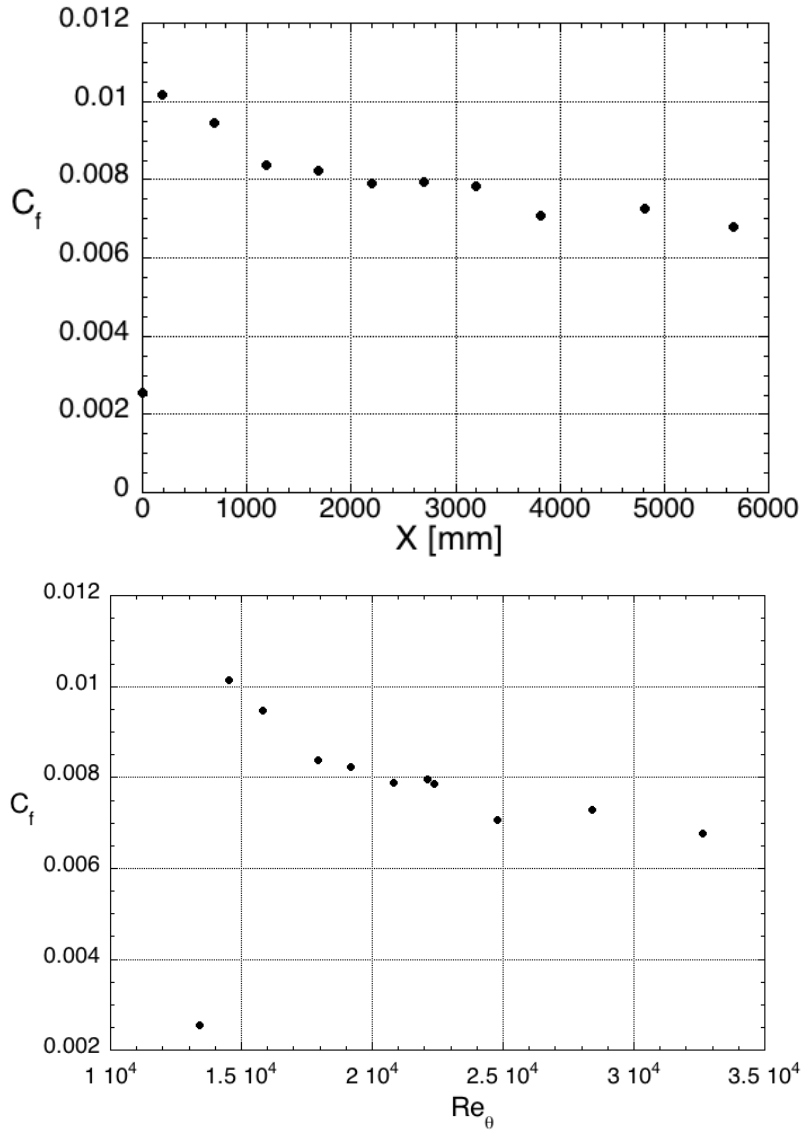


Figure 3.2: Variation of C_f , vs. X and Re_θ .

3.2 Results

3.2.1 Mean flow

The mean velocity profiles for smooth and rough surfaces are presented in Figure (3.3). The mean velocity profile, described by logarithmic-law, was calculated as,

$$\frac{U}{u_\tau} = \frac{1}{\kappa} \ln \left(\frac{[y + \epsilon] u_\tau}{\nu} \right) + B - \Delta U^+ \quad (3.1)$$

where ϵ is the shift in origin from the measurement coordinate system to the effective wall location and ΔU^+ is the shift in the log law due to the roughness effect on the mean flow. In our experiment the log-law constants $k = 0.41$, $B = 5.2$, $\epsilon = 0$ and the origin of y is at the bottom of the groove, see Figure (3.1). The variation of ΔU^+ and δ/k vs. k^+ are depicted in Figure (3.4) and Figure (3.5). The shift in log law is almost constant for all cases.

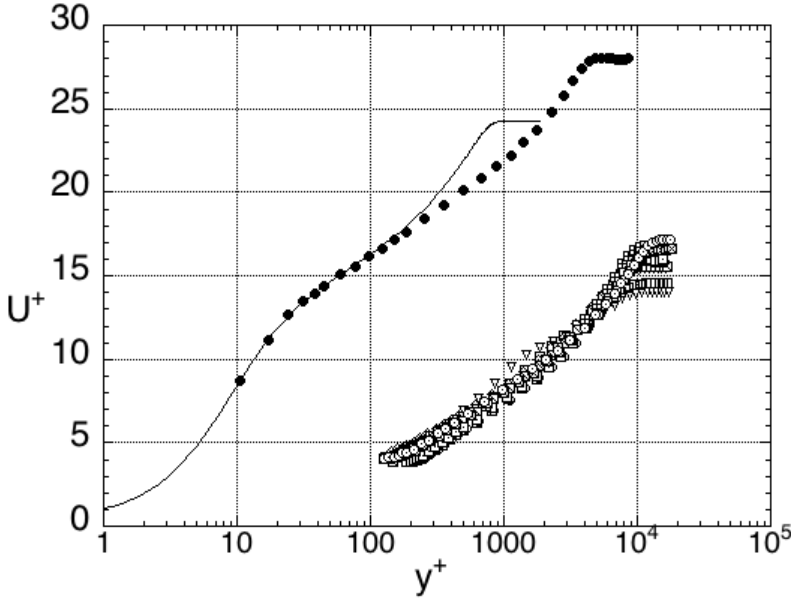


Figure 3.3: Mean-velocity distribution for smooth- and rough-surfaces. Symbols: – DNS smooth, \times 0, ∇ 0.2, \square 0.7, \diamond 1.2, \square 1.7, \triangle 2.2, \circ 2.7, \square 3.2, \boxplus 3.8, \boxstar 4.8, \odot 5.66.

The velocity-defect profiles as a function of y/δ and y/Δ are plotted in Figure (3.6). where $\Delta = \delta^* \cdot U_e/u_\tau$. Note that the thickness of the boundary layer δ cannot be precisely determined (see Rotta; Monin & Yaglom) . A better collapse is obtained

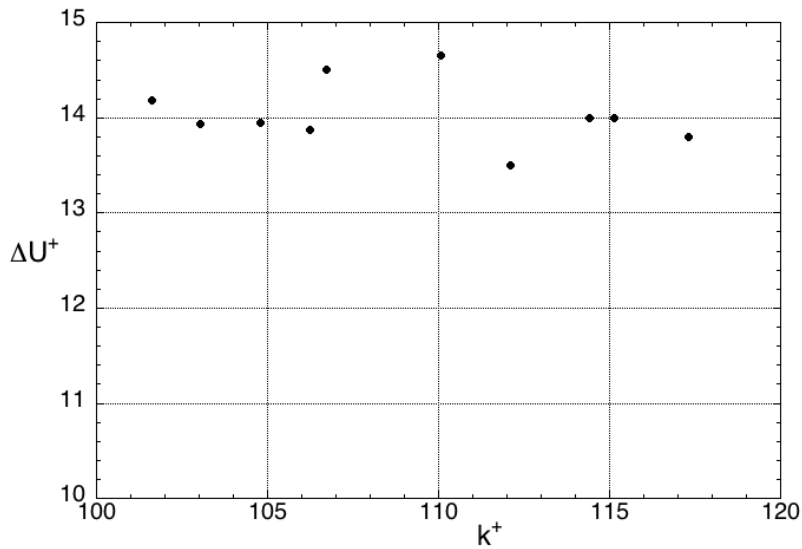


Figure 3.4: Shift in mean velocity, ΔU^+ vs. k^+ .

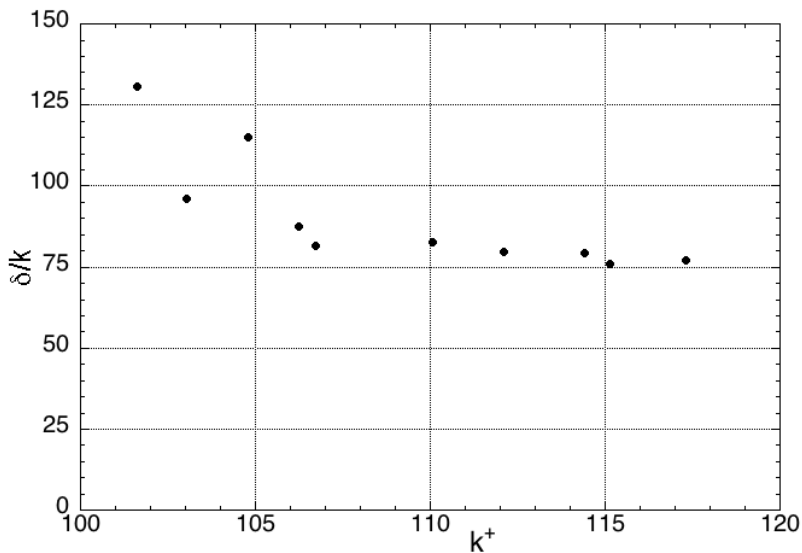


Figure 3.5: The variation of δ/k vs. k^+ .

when the data is plotted as function of y/Δ . This is because:

$$\Delta = \delta^* \frac{U_e}{u_\tau} = \int_0^\infty \left(\frac{U_e - u}{u_\tau} \right) dy \Rightarrow \int_0^\infty \left(\frac{U_e - u}{u_\tau} \right) d\left(\frac{y}{\Delta}\right) = 1 \quad (3.2)$$

and

$$\frac{\Delta}{\delta} = \frac{\delta^*}{\delta} \frac{U_e}{u_\tau} = \frac{1 + \Pi}{\kappa} \quad (3.3)$$

For more details about how to obtain equation (3.3) see Castro (2007). Therefore if the wakes are the same and Re_θ sufficiently high you will always get a complete collapse.

A combination between δ and δ^* is the velocity scale, $(U_e \delta^* / \delta)$, proposed by Zaragola & Smits (1998) which is similar to one proposed by Rotta (1962).

$$U_e \frac{\delta^*}{\delta} = \int_0^\infty (U_e - u) d\left(\frac{y}{\delta}\right) \Rightarrow \int_0^\infty \left(\frac{U_e - u}{u_\tau} \right) d\left(\frac{y u_\tau}{\delta^* U_e}\right) = 1 \quad (3.4)$$

Velocity-defect profiles, using Zaragola & Smits scaling, are presented in Figure (3.7). The collapse of the velocity profiles using Zaragola & Smits scaling is quite good and shows no effect of roughness except near the wall. Again, this method guarantees collapse if $\Pi(y/\delta)$ is the same and can only distinguish differences in the shape of the wake.

The scaling of velocity-defect profiles using U_e as scaling parameter is also included in Figure (3.7). The profiles depicted in Figure (3.7) show no collapse of data. This is in agreement with Akinlade *et al.* (2004), who showed that the roughness is eliminated when the defect profile is scaled with $U_e \delta^* / \delta$ and that the effect of roughness is more evident when the defect profile is scaled with U_e .

The Clauser's shape parameter is defined as,

$$G = \frac{1}{\Delta} \int_0^\infty \left(\frac{U_e - u}{u_\tau} \right)^2 dy \quad (3.5)$$

and has a value of 6.8 for constant pressure turbulent boundary layers (Clauser 1956) and $Re_\theta > 10 \cdot 10^3$ (Bandyopadhyay 1992). For $X > 2.7m$ the value of G for rough surfaces is about 6.5 which is slightly lower than the measured value for smooth surface, $X = 0$, which is 6.7. Using the value of $G = 6.6$ an indirect check was carried out using the equation:

$$H = \left[1 - G \left(\frac{C_f}{2} \right)^{0.5} \right]^{-1} \quad (3.6)$$

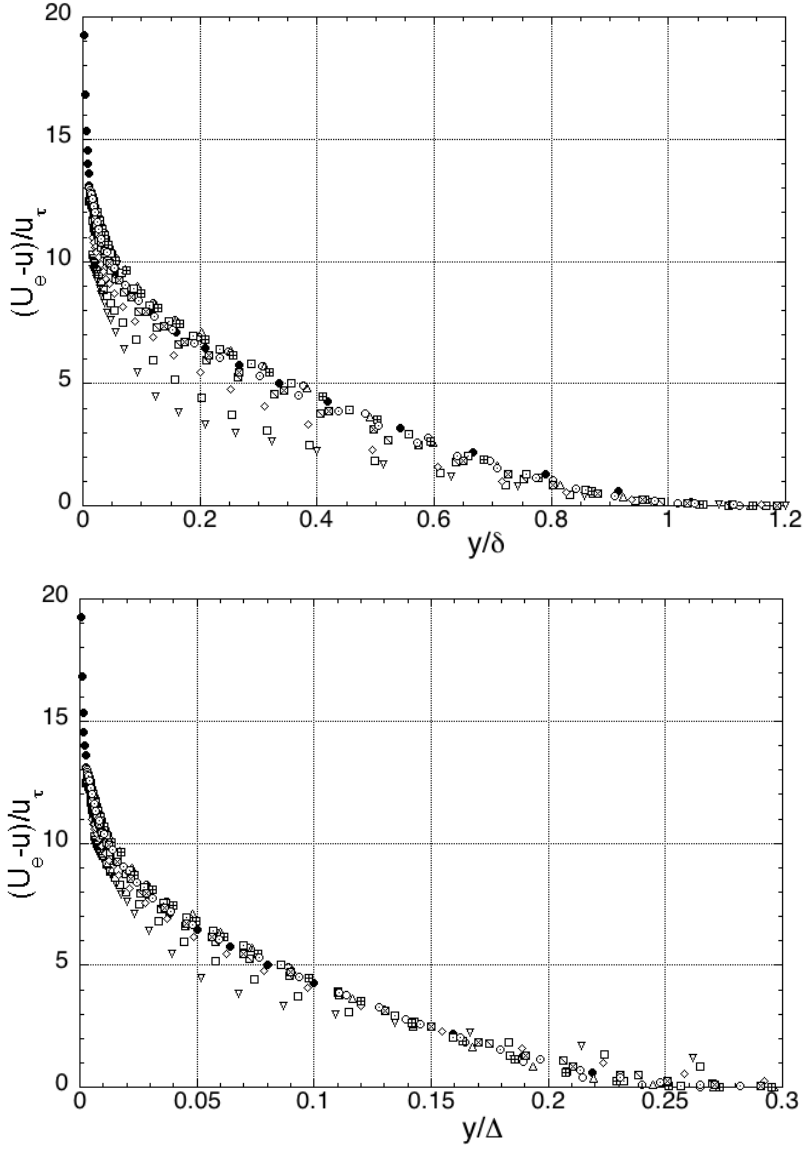


Figure 3.6: Velocity defect profiles , vs. y/δ and y/Δ . Symbols: \bullet $X=0$, ∇ 0.2, \square 0.7, \diamond 1.2, \boxtimes 1.7, \triangle 2.2, \circ 2.7, \boxdot 3.2, \oplus 3.8, \boxtimes 4.8, \odot 5.66.

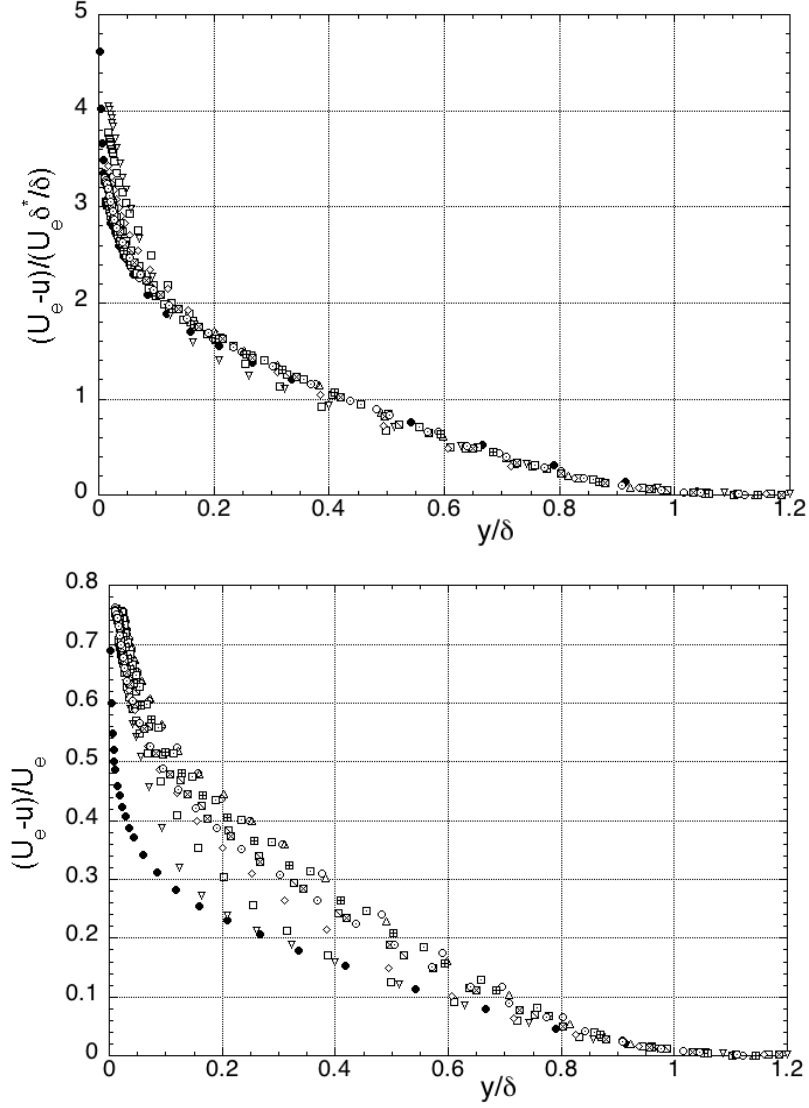


Figure 3.7: Velocity defect profiles. a) Zagarola & Smits scaling b) George & Castillo. Symbols: \bullet $X=0$, ∇ 0.2, \square 0.7, \diamond 1.2, \boxtimes 1.7, \triangle 2.2, \circ 2.7, \square 3.2, \boxplus 3.8, \boxtimes 4.8, \odot 5.66.

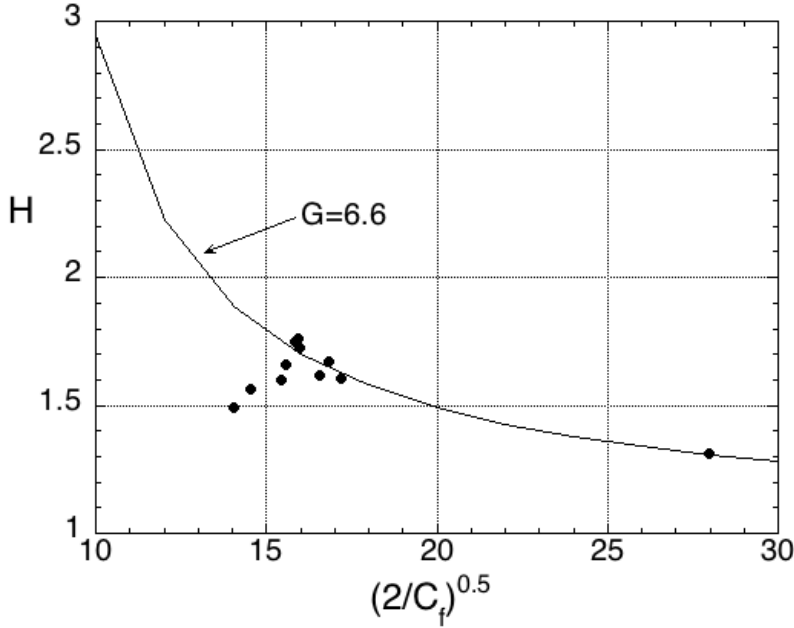


Figure 3.8: Skin-friction results obtained from balance compared with the eqn(3.6)

For $X > 2.2 m$ a good agreement is obtained between equation (3.6) and measured value see Figure (3.8). The Figure (3.8) confirms the relation between H and C_f (see equation (3.6)) but only for fully developed flows.

The displacement thickness δ^* and the momentum thickness θ depicted in Figure (3.9) have almost linear increase with X . The deviation of the displacement thickness, δ^* , from the linear trend shown in Figure (3.9) is in agreement with the velocity defect-law (see Figure (3.6)). This reveals that the retardation of the flow due to the wall effects are constant for $X > 1.7 m$ and flow develops differently.

Following Rotta (1962) the relation between the friction coefficient, C_f , and displacement thickness, δ^* , can be written:

$$\sqrt{\frac{2}{C_f}} = \frac{1}{\kappa} \ln \left(\frac{\delta^*}{k} \sqrt{\frac{2}{C_f}} \right) + const \quad (3.7)$$

The skin friction plotted according to equation (3.7) are shown in Figure (3.10). The data exhibit collapse, with experimental uncertainty, to a line with slope $1/\kappa$. The same correlation was found by Acharya *et. al.* (1986).

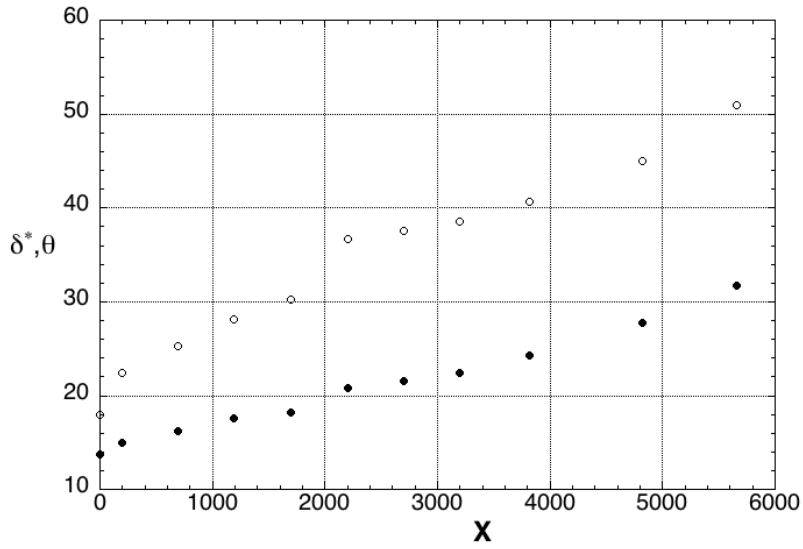
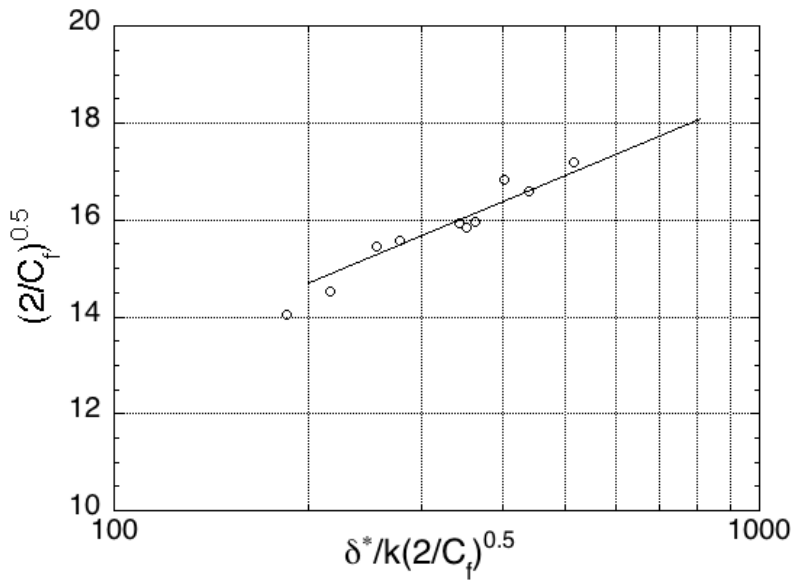
Figure 3.9: Distribution of δ^* (○) and θ (●)

Figure 3.10: Skin friction versus displacement thickness

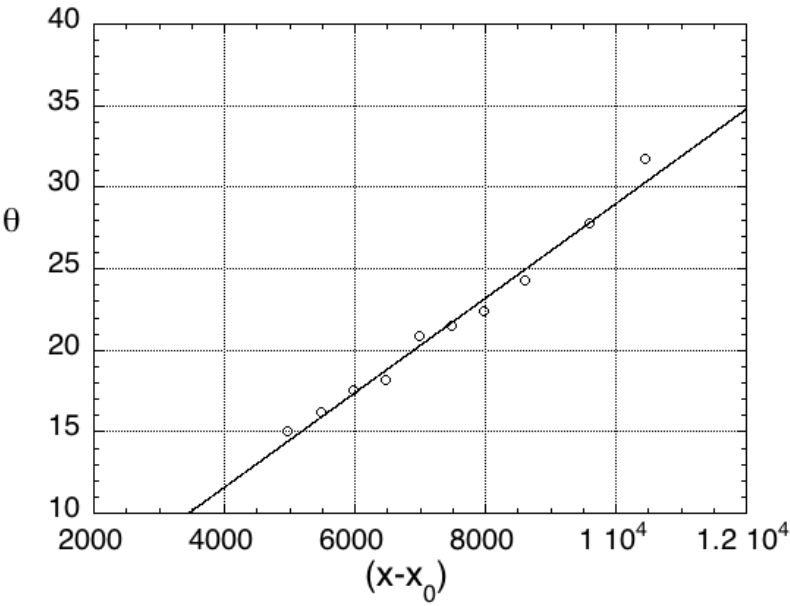


Figure 3.11: Momentum thickness θ .

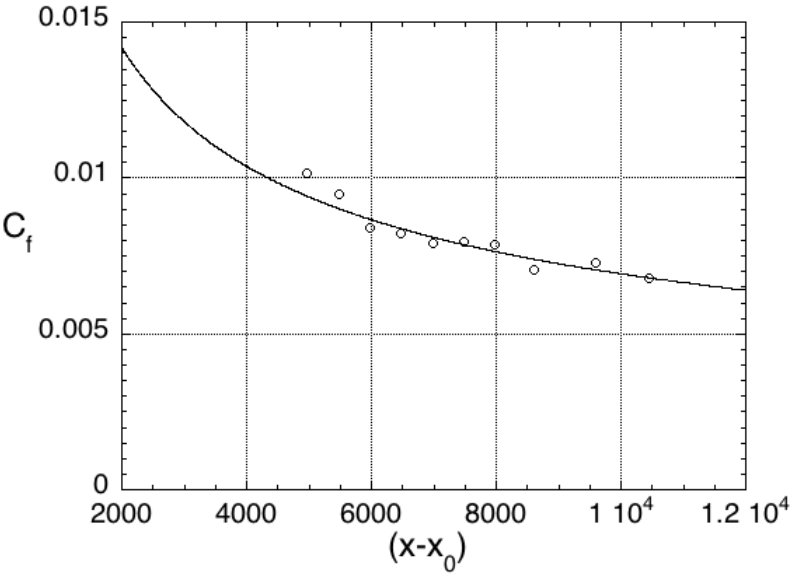


Figure 3.12: Skin friction as function of $(X - X_0)$

Using the relation between θ and δ^* ,

$$\theta = \delta^* \left(1 - G \sqrt{\frac{C_f}{2}} \right) \quad (3.8)$$

in equation (3.7) we can obtain:

$$\sqrt{\frac{2}{C_f}} = -\frac{1}{\kappa} \left[\ln \frac{k}{\theta} + \ln \left(1 - G \sqrt{\frac{C_f}{2}} \right) + \frac{1}{2} \ln \frac{C_f}{2} \right] + const \quad (3.9)$$

This equation gives a relation between skin friction, C_f , and momentum thickness, θ , see Rotta (1962). This mean that being given θ as function of X or $X - X_0$, C_f can be calculated as a function of X or respectively as a function of $X - X_0$. Figure (3.11) presents the $\theta = f(X - X_0)$ data. The $C_f = f(X - X_0)$ using $G = 6.6$ and $\theta = 0.0029(X - X_0)$ obtained as best fit from Figure (3.11) is shown in Figure (3.12). The trend between the calculated and experimental value is quite good except for the first two points. It appears the the skin friction coefficient, C_f , can be computed quite well based on the available distribution of momentum thickness. The shape parameter $H = \delta^*/\theta$ is shown in Figure (3.13). It increases from a value of 1.3 on smooth-surface to a maximum value of 1.76 for $X = 2.2\text{ m}$ and slowly decreasing with further increasing of the X to a value of 1.6.

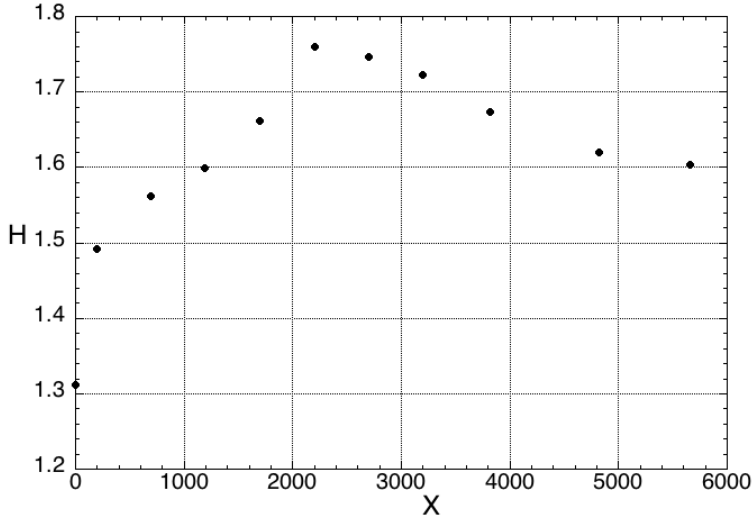


Figure 3.13: The shape parameter H .

3.2.2 Internal Boundary layer

For $X = 0$, we have a fully developed turbulent boundary layer over a smooth surface. Increasing the length, X , of rough surface changes the roughness of the surface. The change in roughness is usually measured by the roughness step M . The roughness step is defined as $M = \ln(z_{01}/z_{02})$ where z_0 is the equivalent roughness length. The value for z_0 was determined using the equation (3.10):

$$z_0 = \frac{\nu}{u_\tau} \exp\left(\kappa \left(\frac{\Delta U}{u_\tau} - B\right)\right) \quad (3.10)$$

The value obtained for $X = 0$ is $z_{01} = 0.0034 \text{ mm}$ and for $X = 5.66 \text{ m}$ is $z_{02} = 0.585 \text{ mm}$. With the value for z_{01} and z_{02} calculated from above we found $M = -5.15$. The value found by Antonia & Luxton (1971a) was $M = -4.6$ which points out that the perturbations due to the rough surface is higher in our case.

After a change in surface roughness an internal boundary layer develops downward of the discontinuity. The internal layer will be in equilibrium with the rough-surface while the outer layer will have the characteristics determined by the smooth-surface. The internal layer depends on the length X and the type of the rough surface. With increasing the length X we expect the internal layer to increase until there is no outer layer determined by the smooth-surface.

The height of the internal boundary layer has been defined and determined in many ways - e.g. Antonia & Luxton (1971a) used half-power method of plotting mean profiles U/U_∞ vs. $y^{0.5}$ and from the 'knee' point, to estimate the position of

the edge of internal boundary layer. Using this method Antonia & Luxton (1971a) obtained a growth rate of internal layer $\delta_i \sim x^{0.72}$. In our case the thickness of internal layer δ_i was determined, similar to Krogstad & Nickels (2006), by fitting the internal and outer layer of stream wise stresses $\langle uu \rangle$ with a straight line. The intersection of these two lines was considered the merging point of the two layers.

A fit to all points is given by $\delta_i \sim x^{0.73}$, which is in good agreement with Antonia & Luxton and close to the result of Krogstad & Nickels (2006) $\delta_i \sim x^{0.7}$. The variation of boundary layer thickness and of internal boundary layer with length, X , of rough surface is presented in Figure (3.14). The Figure (3.14) shows that the internal boundary layer has grown to the edge of the boundary layer at $X \sim 2.7 m$. Figure (3.15) presents the data corresponding to Elliot's (1958) formula for growth

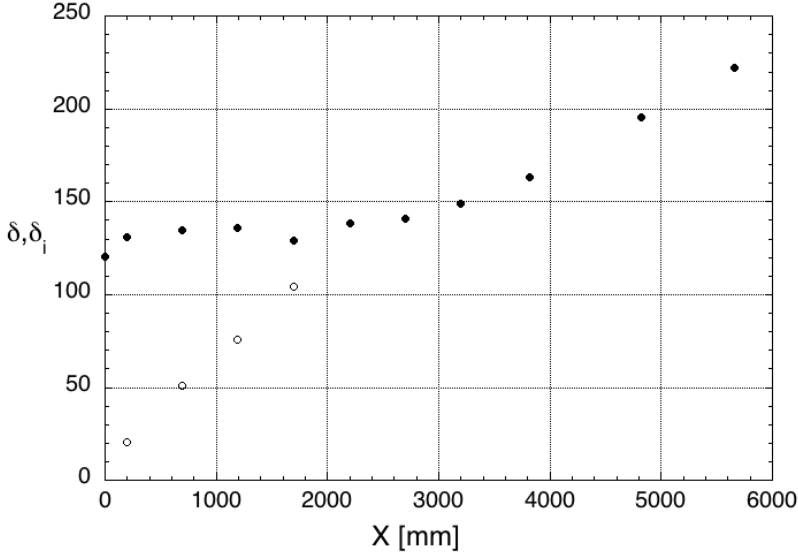


Figure 3.14: The variation of boundary layer thickness δ (●) and internal boundary layer thickness δ_i (○) with X

of the internal boundary layer:

$$\frac{\delta_i}{z_{02}} = a \left(\frac{X}{z_{02}} \right)^p \quad (3.11)$$

The coefficient a was calculated according to the relation (see Pendergrass & Arya 1984).

$$a = 0.75 - 0.03M \quad (3.12)$$

For the present experiment the magnitude of a calculated with equation (3.12) was ~ 0.90 . A better agreement is obtained with $a = 0.37$ see Figure 3.15. This is

CHAPTER 3. TURBULENT BOUNDARY LAYER OVER A STEP CHANGE: SMOOTH TO ROUGH. LDV MEASUREMENTS

in agreement with (Pendergrass & Arya 1984), they found $a = 0.38$. The value for p was 0.8 in Elliot's formula in agreement with Schlichting (1968) who showed that boundary layer thickness, for turbulent boundary layer, increases as $\delta \sim x^{0.8}$. Using equation (3.11), with $a = 0.37$, we obtained a good result with $p = 0.78$, see Figure (3.15), that is in good agreement with the one, $p = 0.79$, obtained by Antonia & Luxton using the same equation (3.11).

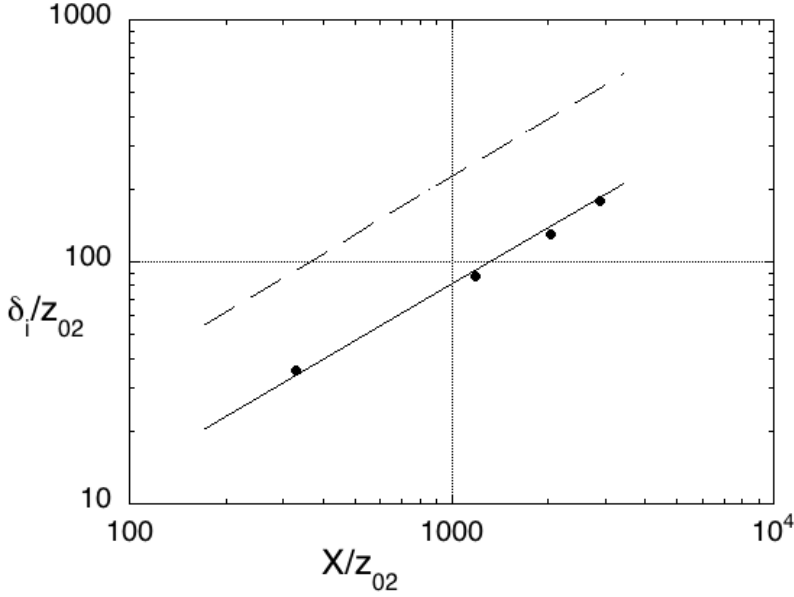


Figure 3.15: Comparison of the experimental development δ_i (•) with the theory of Elliot (1958) $-- \delta_i/z_{02} = 0.90(X/z_{02})^{0.8}$, $- \delta_i/z_{02} = 0.37(X/z_{02})^{0.78}$

3.2.3 Reynolds stresses

The Reynolds stresses normalized with inner and outer variables are shown in Figure (3.16) to Figure (3.18) together with the results of smooth wall DNS by Schlatter *et al.* (2009) at $Re_\theta = 2400$. Figure (3.16) shows the $\langle uu^+ \rangle$ component. The maximum value of $\langle uu^+ \rangle$, for smooth surface, is located at $y^+ \approx 17$ which is in a good agreement with the DNS data. For $X = 5.66m$ we can notice that $\langle uu^+ \rangle$ is increasing from $y^+ \approx 150$ (1.35k) until it reaches a peak at $y^+ \approx 700$ (5.5k). The same can be noticed for $X = 3.8m$ and $X = 4.8m$. From the DNS (see Sung *et al.* 2007) we know that there is a peak near the wall followed by a valley and a second peak further from the wall. Our measurements show the second peak and suggest the possibility to have a minimum at $y^+ \approx 150$. The second peak, for high Reynolds number, was noticed also by Marusic *et al.* 2009 and Metzger *et al.* 2007. Marusic *et al.* 2009 associated the second peak with very large-scale structure, while Metzger *et al.* 2007 associated it with roughness effect. For low Reynolds number, the second peak for rough-surface was noticed in the DNS (Sung *et al.* 2007), but only over the roughness element. It is evident that the second peak for smooth surface is an effect of the high Reynolds number while for the rough-surface we have in addition the effect of the roughness.

Increasing the length of rough-surface X affects the $\langle uu^+ \rangle$ in two ways.

First, the peak, $\max(\langle uu^+ \rangle)$, increases in magnitude with increasing the length X , from 3.5 at $X = 0.2m$ to 5.2 at $X = 5.66m$, and moves from $y^+ \approx 255$ (2.2k) at $X = 0.2$ to $y^+ \approx 723$ (7k) at $X = 5.66m$.

Second, the $\langle uu^+ \rangle$ extends progressively further into outer layer of initially boundary layer over smooth surface as X is increasing. The second observation is valid also for $\langle vv^+ \rangle$ and $\langle uv^+ \rangle$ component. The streamwise Reynolds stresses, $\langle uu^+ \rangle$, in outer variables, show good agreement between the rough-, $X > 1.7m$, and smooth-surfaces in the region $0.15 < y/\delta < 0.9$. This is in agreement with Flack *et al.* (2007) and with the data discussed by Raupach *et al.* (1991).

The fluctuating component v , normal to the wall, provides information about the turbulence transport and production of shear stress. Figure (3.17) shows the $\langle vv^+ \rangle$ component in inner and outer variables. Reynolds number similarity is noticed for $y^+ < 150$, for smooth surface, with good agreement between experiment and DNS.

The change in surface will create a peak in $\langle vv^+ \rangle$ at around $y^+ = 200$ (1.8k), $X = 0.2m$, followed by a drop. The peak near the wall for $X > 0$ is a characteristic of the roughness and is in agreement with DNS of Sung *et al.* (2007). The position of near wall peak for $\langle vv^+ \rangle$ is close to the position of minimum for $\langle uu^+ \rangle$ which indicate that the reduction in $\langle uu^+ \rangle$ has been compensated by the increase in $\langle vv^+ \rangle$. Increasing further the length X of the rough surface will create a plateau which for $X > 2.7m$ will result in a second top, $y/\delta \approx 0.2$. For $X = 5.66m$ the first peak is situated at $y^+ \approx 185$ (1.8k), the minimum is at $y^+ \approx 380$

(3.5k) and the second peak is situated at $y^+ \approx 2500$ (24.8k). The magnitude of first and second peak is almost the same, 1.52 and 1.54, the valley for $\langle vv^+ \rangle$, as position, is close to the second top for $\langle uu^+ \rangle$. In our case the ratio between the first and the second peak is almost one while in DNS of Sung *et al.* (2007) this ratio is 0.5. This suggests that the second peak is increasing with increasing the length of the rough surface, X , and the Reynolds number. According to Fernholz & Finley (1996), for smooth surface, some data display an increase in the outer peak when increasing the Reynolds number, some display to be independent of the Reynolds number.

The Reynolds shear stress $\langle -uv^+ \rangle$ is the dominant part of the shear stress and is a significant part in the production term for the kinetic energy (Fernholz & Finley (1996)). The $\langle uv^+ \rangle$ component in inner and outer variables is shown in Figure (3.18). Similar to $\langle vv^+ \rangle$, for smooth surface, the data collapse well for $y^+ < 150$. The maxim value for $-\langle uv \rangle^+$ obtained from measurements for $X = 0$ is ~ 0.96 which is similar to the value ~ 0.95 obtained by DNS (see Schlatter & Örlü 2010). This indicate that the measurements are not affected by any probe effects (Fernholz & Finley (1996)). The change in surface, $X = 0.2\text{ m}$, will create a peak in $\langle uv^+ \rangle$ close to the position of the first peak in $\langle vv^+ \rangle$. Increasing further the length, X , of the rough surface the $\langle uv^+ \rangle$ will display a plateau similar to the smooth surface. For $X = 5.66\text{ m}$ the plateau extends from $y^+ \approx 200$ (1.8k) to $y^+ \approx 2000$ (19k).

The effect of roughness on outer flow is small when the velocity is scaled with u_τ . To make the effect of roughness more evident the results are normalized with U_e . The longitudinal and vertical stresses normalized with U_e^2 are shown in Figure (3.19). With increase in the length, X , of the rough surface the profiles are shifted upward making a clear distinction between smooth and rough surface. It is observed that the increase in Reynolds stresses is delimited by the thickness of internal layer δ_i . For $X > 2.2\text{ m}$ the flow has fully recovered from the effect of the roughness. Near the wall the peak of $\langle uu \rangle / U_e^2$ is almost constant while the peak for $\langle uv \rangle / U_e^2$ and $\langle vv \rangle / U_e^2$ overshoots the equilibrium value and decreases with increasing X towards the value of full rough surface. The same was noticed by Pendergrass & Arya (1984). The $-\langle uv \rangle$ profiles normalized with U_e^2 are presented in Figure (3.20). The distribution of $-\langle uv \rangle$ shows the same trend as $\langle vv \rangle$ profiles.

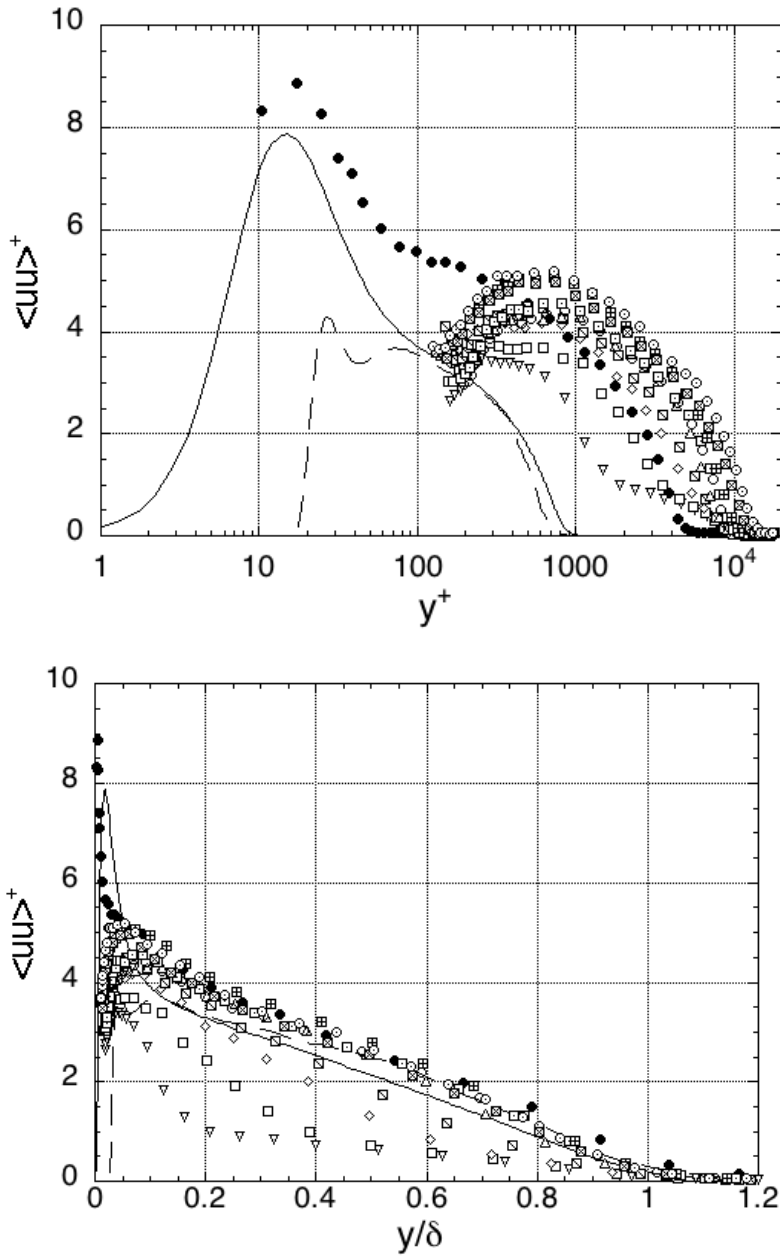


Figure 3.16: Streamwise normal stress, $\langle uu^+ \rangle$ vs. y/δ and y^+ . Symbols: — DNS smooth surface, -- DNS rough surface, • $X=0$, ∇ 0.2, \square 0.7, \diamond 1.2, \square 1.7, \triangle 2.2, \circ 2.7, \square 3.2, \boxplus 3.8, \boxtimes 4.8, \odot 5.66.

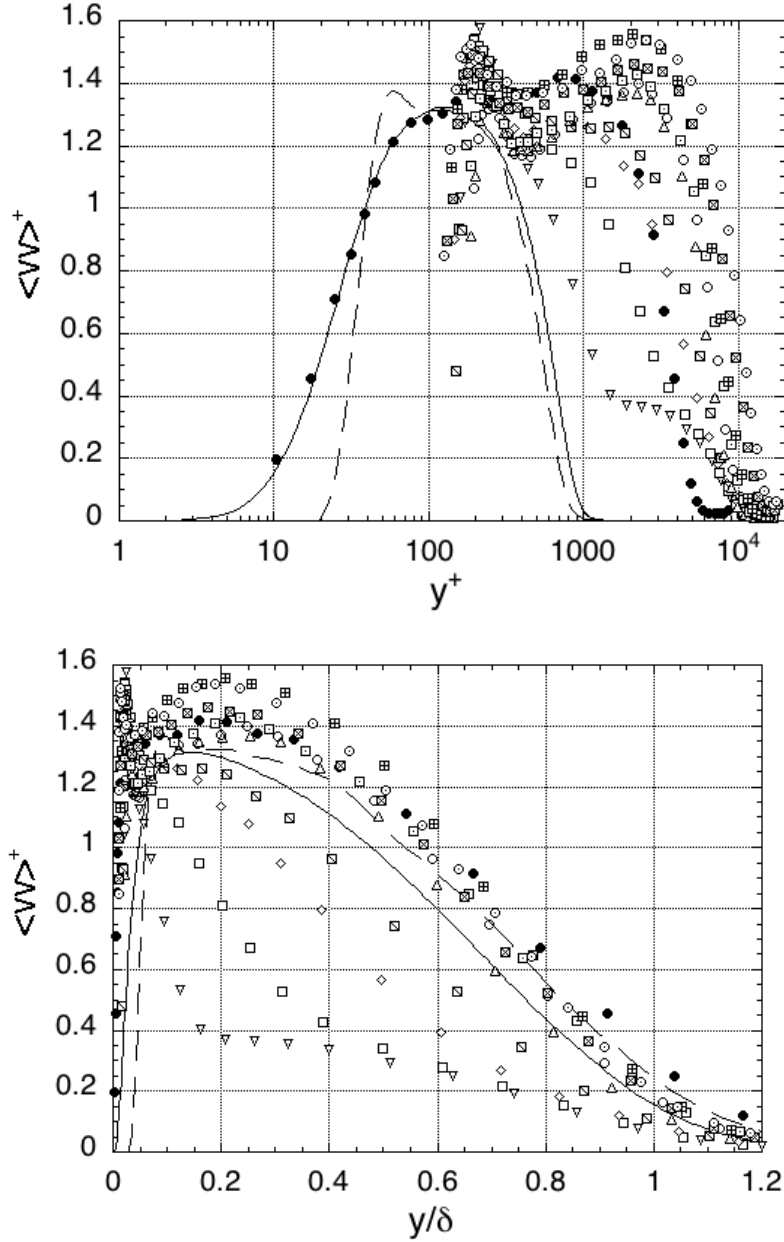


Figure 3.17: Wall-normal stress, $\langle vv^+ \rangle$ vs. y/δ and y^+ . Symbols: — DNS smooth surface, -- DNS rough surface, • $X=0$, ∇ 0.2, \square 0.7, \diamond 1.2, \boxplus 1.7, \triangle 2.2, \odot 2.7, \boxplus 3.2, \boxtimes 3.8, \boxtimes 4.8, \odot 5.66.

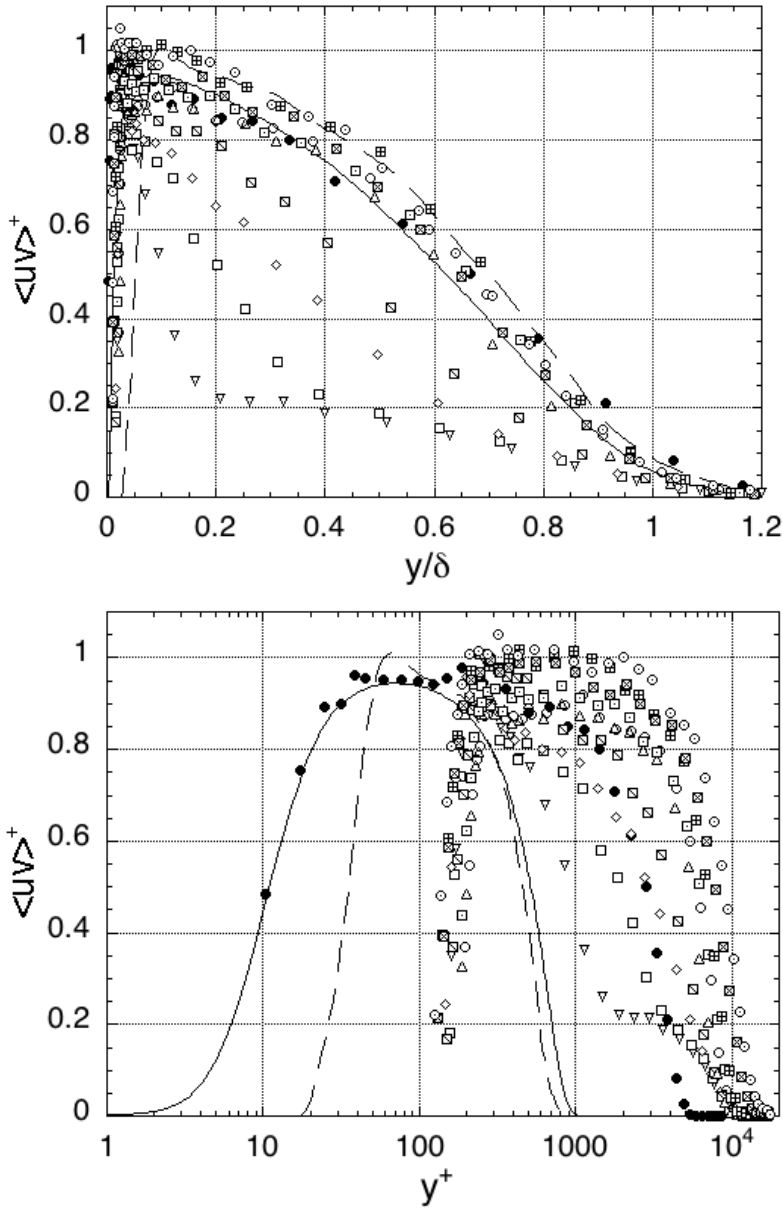


Figure 3.18: Shear stress, $-\langle uv^+ \rangle$ vs. y/δ and y^+ . Symbols: — DNS smooth, -- DNS rough surface, • $X=0$, ∇ 0.2, \square 0.7, \diamond 1.2, \boxtimes 1.7, \triangle 2.2, \circ 2.7, \square 3.2, \boxtimes 3.8, \boxtimes 4.8, \odot 5.66.

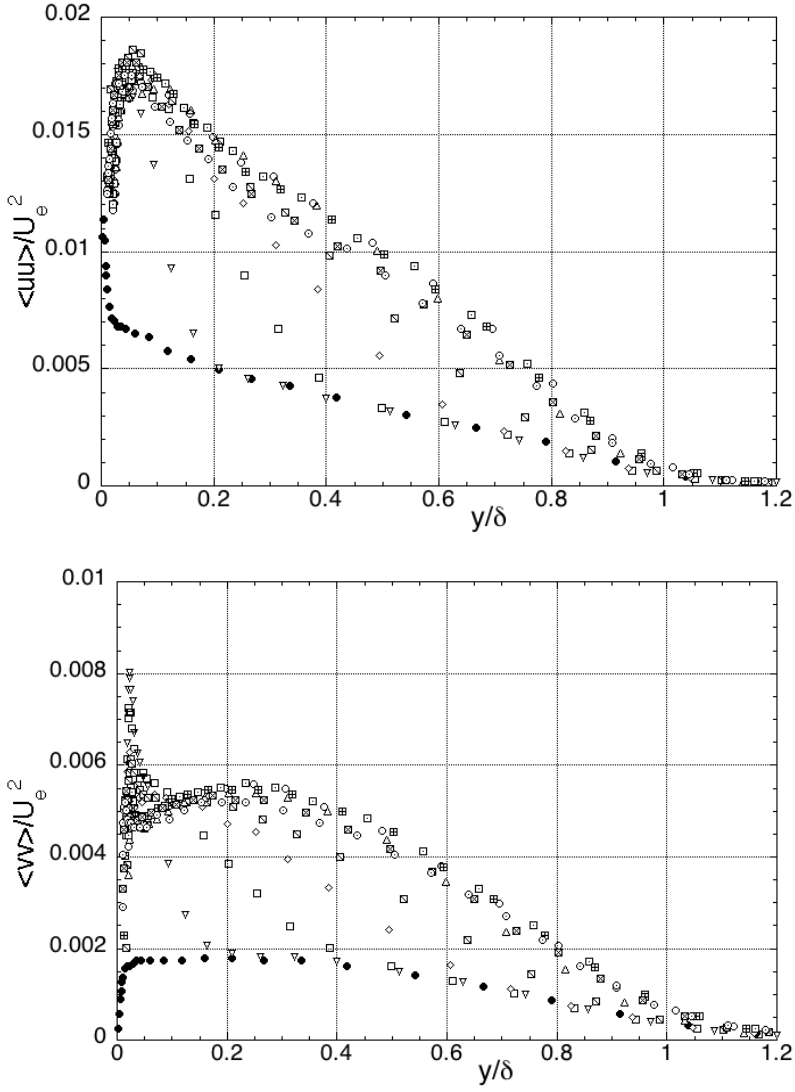


Figure 3.19: Reynolds stresses normalized with U_e^2 . Symbols: \bullet $X=0$, ∇ 0.2, \square 0.7, \diamond 1.2, \boxtimes 1.7, \triangle 2.2, \odot 2.7, \boxplus 3.2, \boxdot 3.8, \boxtimes 4.8, \odot 5.66.

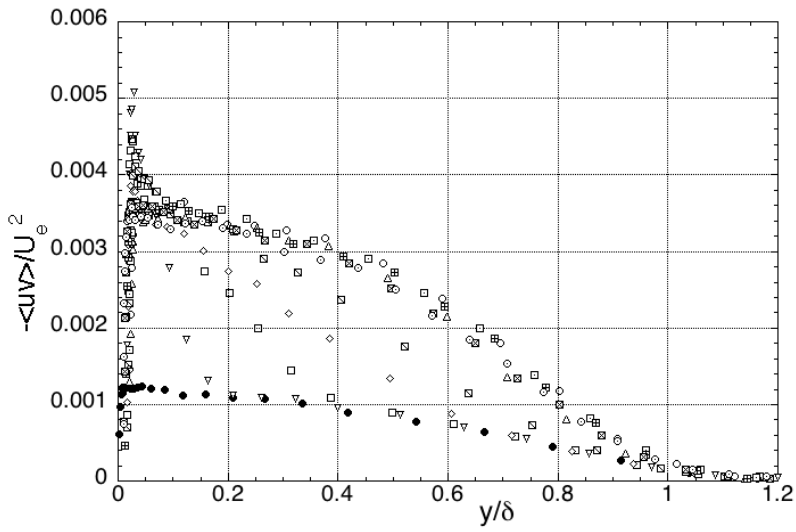


Figure 3.20: Shear stress profiles normalized with U_e^2 . Symbols: \bullet $X=0$, ∇ 0.2, \square 0.7, \diamond 1.2, \boxplus 1.7, \triangle 2.2, \odot 2.7, \boxplus 3.2, \boxtimes 3.8, \boxtimes 4.8, \odot 5.66.

3.2.4 Transport equation for Reynolds stresses

The transport equation for turbulent stresses, $\langle u_i u_j \rangle$, is:

$$\begin{aligned}
 \underbrace{U_k \frac{\partial}{\partial x_k} \langle u_i u_j \rangle}_{\text{Advection}} &= \underbrace{\left\langle \frac{p}{\rho} \left[\frac{\partial u_i}{\partial x_j} + \frac{\partial u_j}{\partial x_i} \right] \right\rangle}_{\text{Pressure-Strain}} \\
 + \underbrace{\frac{\partial}{\partial x_k} \left\{ - \left[\left\langle \frac{p u_j}{\rho} \right\rangle \delta_{ik} + \left\langle \frac{p u_i}{\rho} \right\rangle \delta_{kj} - \langle u_i u_k u_j \rangle \right] + \nu \frac{\partial}{\partial x_k} \langle u_i u_j \rangle \right\}}_{\text{Diffusion}} & \\
 - \underbrace{\left[\langle u_i u_k \rangle \frac{\partial U_j}{\partial x_k} + \langle u_k u_j \rangle \frac{\partial U_i}{\partial x_k} \right]}_{\text{Production}} & \\
 - \underbrace{2\nu \left\langle \frac{\partial u_i}{\partial x_k} \frac{\partial u_j}{\partial x_k} \right\rangle}_{\text{Dissipation}} & \quad (3.13)
 \end{aligned}$$

The turbulent kinetic energy is the sum of all normal Reynolds stresses $q = 1/2 \langle u_i u_i \rangle$. Setting the indices $i = j$ in equation (3.13) and dividing by two we obtain the equation for the turbulent kinetic energy:

$$\begin{aligned}
 \underbrace{U_j \frac{\partial q}{\partial x_j}}_{\text{Advection}} &= \underbrace{\frac{\partial}{\partial x_j} \left\{ - \left\langle u_j \left(\frac{p}{\rho} + \frac{1}{2} u_i u_i \right) \right\rangle + \nu \frac{\partial q}{\partial x_j} \right\}}_{\text{Diffusion}} \\
 - \underbrace{\left\langle u_i u_j \right\rangle \frac{\partial U_i}{\partial x_j}}_{\text{Production}} &- \underbrace{\nu \left\langle \frac{\partial u_i}{\partial x_j} \frac{\partial u_j}{\partial x_j} \right\rangle}_{\text{Dissipation}} \quad (3.14)
 \end{aligned}$$

The pressure-strain term, which appears only in equation (3.13), promotes isotropy of turbulence by redistribution of turbulent fluxes among the normal Reynolds stresses. The diffusive term or the transport term represent the spatial transport of turbulent fluxes or turbulent energy, its integral over the flow volume must be zero. The triple correlation, $\langle u_i u_k u_j \rangle$, is a part of the diffusion term. The triple correlations, $\langle u^3 \rangle$, $\langle u^2 v \rangle$, $\langle u v^2 \rangle$ and $\langle v^3 \rangle$ will be presented in next chapter. The production term is the term that links the Reynolds stresses, $\langle u_i u_j \rangle$, with the mean rate of strain (Cebeci & Smith). This is the only term which provides energy interchange between the mean flow and the fluctuations.

3.2.5 Higher-order Moments

Velocity triple-product is a part of the transport term for Reynolds stresses and turbulent-energy equations. The main role of the transport term is to move energy from one place to another.

The consequence of increasing the length, X , of rough surface, with $U_e \sim \text{const}$, is an increase in Reynolds number, Re_θ . Murlis, Tsai & Bradshaw (1982) mentioned that the triple products normalized by the local shear stress rise slowly with Reynolds number.

The triple-product measurements, normalized with u_{τ} , are presented in Figure (3.21) to Figure (3.24). There are a number of things to be remarked which are common for all cases:

- all profiles show a difference from the smooth-surface case in the vicinity of the wall.
- as the length of rough surface is increased $X > 2.2m$, for $y/\delta > 0.4$, the profiles show good agreement with the smooth-surface data.
- outside the internal boundary layer the slope of higher order moments are very small almost negligible
- the agreement with DNS for smooth surface is quite good

Figure (3.21) shows the $\langle uuu^+ \rangle$ profiles in inner and outer variables. Schultz & Flack (2007) showed that the $\langle uuu^+ \rangle$ over rough surface changes sign and becomes positive near the wall while it stays negative over smooth surface. The trend over rough surface is confirmed by our measurements. The effect of increasing the length, X , of the rough-surface is increase in the near wall peak from 1.5 for $X = 0.2m$ to 3.8 for $X = 5.66m$. Furthermore the smooth-wall $\langle uuu^+ \rangle$ changes sign from positive to negative at $y^+ \approx 18$ ($y/\delta = 0.03$) and for the rough-surfaces it occurs between $y^+ \sim 300$ ($2.5k$) for $X = 0.2m$ and $y^+ = 1000$ ($10k$) for $X = 5.66m$, indicating that the motion correlated with $u > 0$, sweep motion ($u > 0, v < 0$) and outward interaction ($u > 0, v > 0$), is higher for the rough-surface than for the smooth surface. This is in agreement with the results of Flack (2005) and DNS of Sung (2007).

The $\langle uuv^+ \rangle$ and $\langle uvv^+ \rangle$ are part of the transport term, wall-normal direction, for $\langle uu^+ \rangle$ and $\langle -vv^+ \rangle$ components. All the transport terms should be zero at the wall since there is no flow through the surface.

The $\langle uuv^+ \rangle$ profiles in inner and outer variables are depicted in Figure (3.22). A strong negative peak followed by a positive slope, for smooth-surface and rough-surfaces, is observed at $y^+ = 10$ and $y^+ \approx 150$ respectively. The positive slope of $\langle uuv^+ \rangle$ indicates a transport of $\langle uu^+ \rangle$ outward from the wall region. In the outer layer the slope of $\langle uuv^+ \rangle$, for the smooth surface, is almost constant followed by a negative slope after $y/\delta \sim 0.8$ showing a transport of $\langle uu^+ \rangle$ towards

the wall. For $X > 1.2\text{ m}$ in the region $0.3 < y/\delta < 0.65$ the slope, for $\langle uuv^+ \rangle$, is positive and larger than for the smooth surface. It changes sign after $y/\delta \sim 0.65$. Similar behaviour is noticed for $\langle uvv^+ \rangle$ and $\langle vvv^+ \rangle$ in the same region. The $\langle vvv \rangle$ and $\langle uvv \rangle$ are part of the transport term for turbulent kinetic energy. This indicate that the transport of kinetic energy away from the wall is enhanced by the roughness. This is in agreement with DNS of Sung (2007).

Figure (3.23) shows the $\langle uuv^+ \rangle$ profiles in inner and outer variables. The $\langle uuv^+ \rangle$ for smooth surface is negative for most part of the boundary layer except near the wall where it changes sign at $y^+ \approx 22$. It occurs at the same position as $\langle uuv^+ \rangle$ but is opposite in sign. For rough-surfaces, $X < 1.2$, there is a strong negative peak at $y^+ \approx 250$ ($2.2k$ for $X = 0.2$), indicating a transport of $\langle -uv^+ \rangle$ outward from the wall. The peak is increasing with increase in the length, X , of rough surface from -0.7 for $X = 0.2\text{ m}$ to -0.2 for $X = 5.66\text{ m}$.

The $\langle vvv \rangle^+$ profiles, which represent the transport of $\langle vv \rangle$ in wall normal direction, are shown in Figure (3.21). The triple moment $\langle vvv^+ \rangle$, for rough surface, is positive across the entire boundary layer while for smooth-surface it is positive only for $y^+ > 35$. The main differences between smooth and rough-surface, in inner variables, is the existence of a peak near the wall, ($1.8k$ for $X = 0.2\text{ m}$), for rough surface. This indicates that the transport of the $\langle vv^+ \rangle$ from the wall is stronger for the rough surfaces than for the smooth surface.

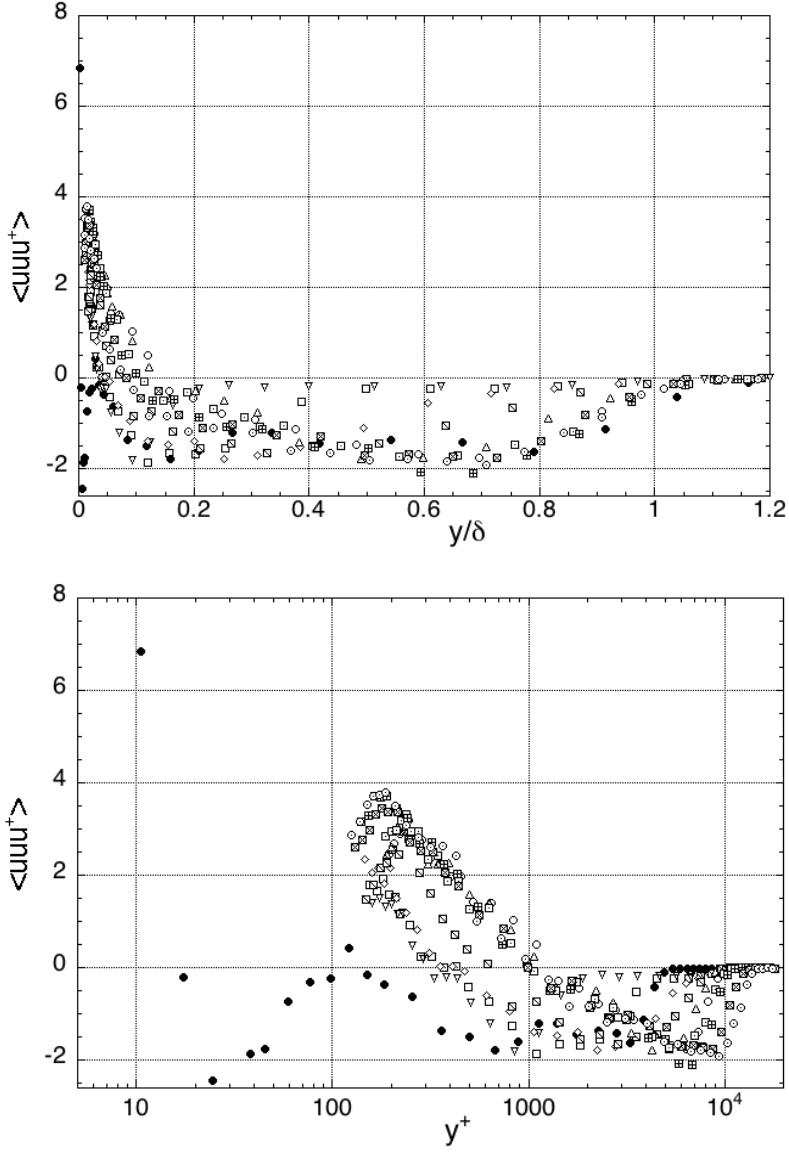


Figure 3.21: Third order moment, $\langle uuu^+ \rangle$ vs. y/δ and y^+ . Symbols: \bullet $X=0$, ∇ 0.2, \square 0.7, \diamond 1.2, \boxminus 1.7, \triangle 2.2, \circ 2.7, \square 3.2, \boxplus 3.8, \boxtimes 4.8, \odot 5.66.

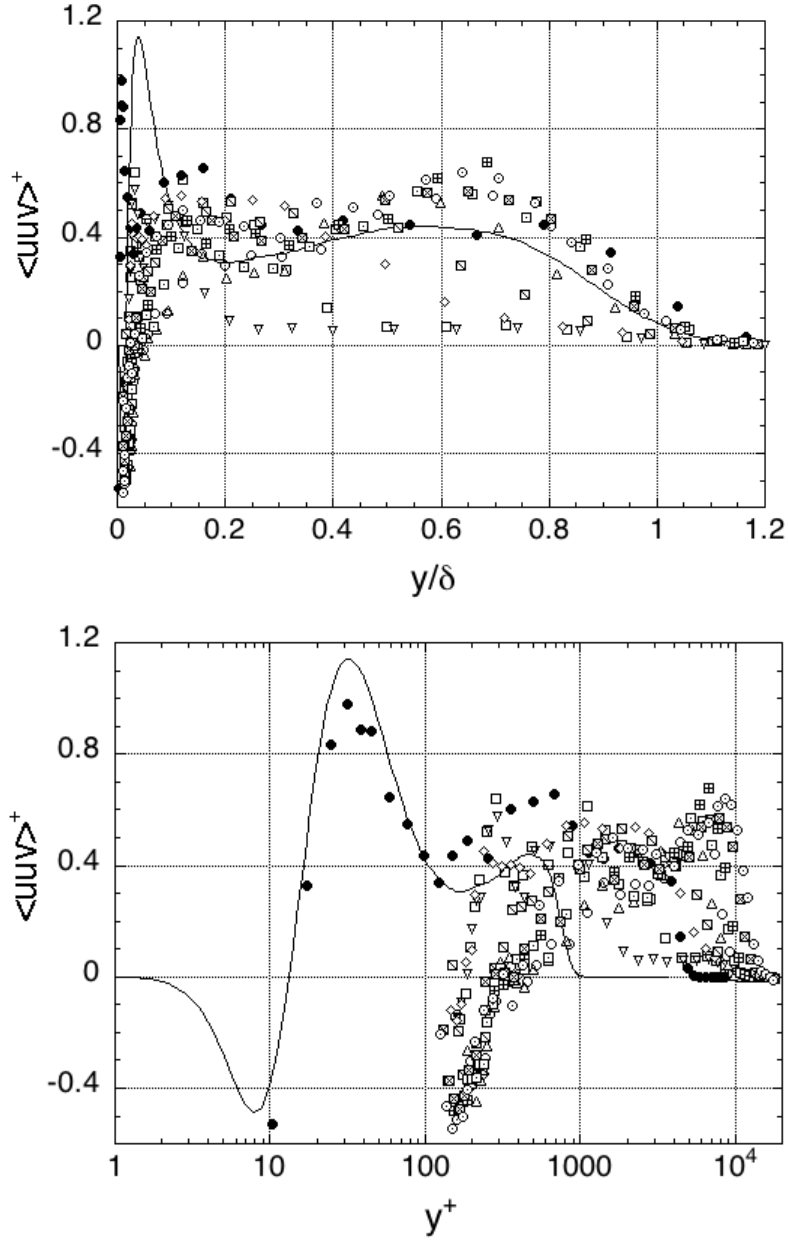


Figure 3.22: Third order moment mixed moment, $\langle uuv^+ \rangle$ vs. y/δ and y^+ . Symbols: — DNS smooth surface, -- DNS rough surface, \bullet $X=0$, ∇ 0.2, \square 0.7, \diamond 1.2, \boxplus 1.7, \triangle 2.2, \circ 2.7, \boxdot 3.2, \boxtimes 3.8, \boxtimes 4.8, \odot 5.66.

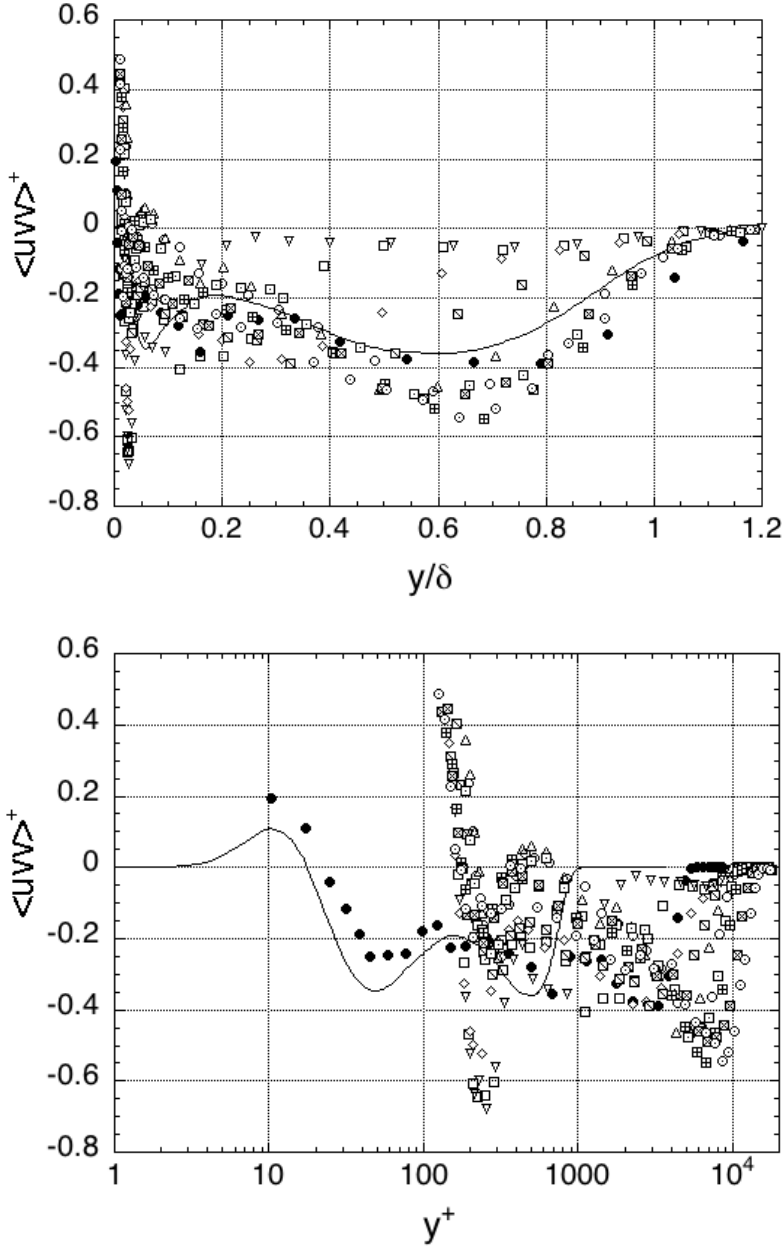


Figure 3.23: Third order moment mixed moment, $\langle uvv^+ \rangle$ vs. y/δ and y^+ . Symbols: — DNS smooth surface, -- DNS rough surface, • $X=0$, ∇ 0.2, \square 0.7, \diamond 1.2, \boxplus 1.7, \triangle 2.2, \odot 2.7, \boxdot 3.2, \boxtimes 3.8, \boxplus 4.8, \odot 5.66.

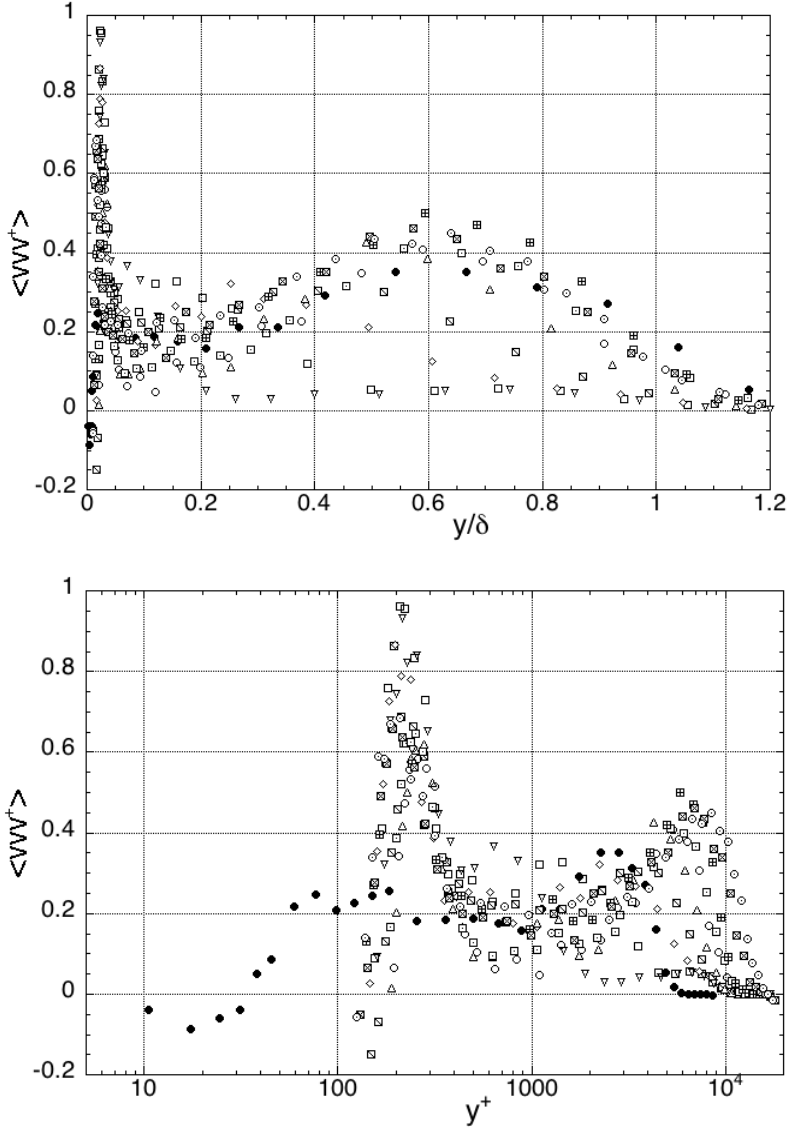


Figure 3.24: Third order moment, $\langle vv v^+ \rangle$ vs. y/δ and y^+ . Symbols: \bullet $X=0$, ∇ 0.2, \square 0.7, \diamond 1.2, \square 1.7, \triangle 2.2, \circ 2.7, \square 3.2, \boxplus 3.8, \boxtimes 4.8, \odot 5.66.

3.2.6 Skewness and Flatness

Skewness and flatness are related to the third and fourth order moments of the probability density function of the velocity fluctuation distribution and are defined as

$$S_\alpha = \frac{\langle \alpha^3 \rangle}{(\langle \alpha^2 \rangle)^{3/2}} \text{ and } F_\alpha = \frac{\langle \alpha^4 \rangle}{(\langle \alpha^2 \rangle)^2} \quad (3.15)$$

where α is one of velocity fluctuations u or v .

The third order moment describes the skewness or the asymmetry of the probability distribution. A positive value of the S_u implies that the positive value of u are more frequent than negative ones (Fernholz & Finley (1996)). $S_u = 0$ implies that the function is symmetric about the origin.

The distribution of skewness factor S_u and S_v for all cases are depicted in Figure (3.25) and Figure (3.26). The S_u for smooth surface is positive near the wall and changes sign at $y^+ \approx 18$ which is the same position with max value for $\langle uu^+ \rangle$ and the point where the ejection start to dominate the sweep events (see Gad-el-Hak & Bandyopadhyay 1994). The S_u and S_v for smooth surface is in agreement with the DNS data of Schlatter (2010) see Figure (3.25) and Figure (3.26). For $X > 0$, S_u is positive near the roughness and change sign with increasing the y^+ , $y^+ \approx 290$ (2.5k) for $X = 0.2 m$ and $y^+ \approx 1000$ (10k) for $X = 5.66 m$. The S_v for smooth surface changes sign from negative to positive at $y^+ \approx 35$. For rough-surfaces, $X > 2.2 m$, S_u change sign at $y^+ \approx 1000$ and S_v changes sign at $y^+ \approx 150$. The $S_u > 0$ and $S_v < 0$ is associated with sweep events and $S_u < 0$ and $S_v > 0$ with ejection events (see Gad-el Hak & Bandyopadhyay (1994)).

The sign of S_u and S_v indicates that near the wall, $y^+ < 20$, for smooth surface the sweeps are predominant mechanism while for rough-surfaces, $y^+ > 100$ both S_u and S_v are positive which are associated with the interaction mechanism.

Fourth order moment, F_u , of the u component is a measure of the frequency of occurrence of events far from the axis (Fernholz & Finley (1996)). The distribution of flatness factor F_u and F_v are shown in Figure (3.27) to Figure (3.28). The flatness has high value in the outer layer indicating that the flow field is highly intermittent in this region. The flatness factor F_u and F_v , for $X > 1.7 m$ and $0.1 < y/\delta < 0.6$, is close to 3, indicating that the flatness is independent of the surface roughness.

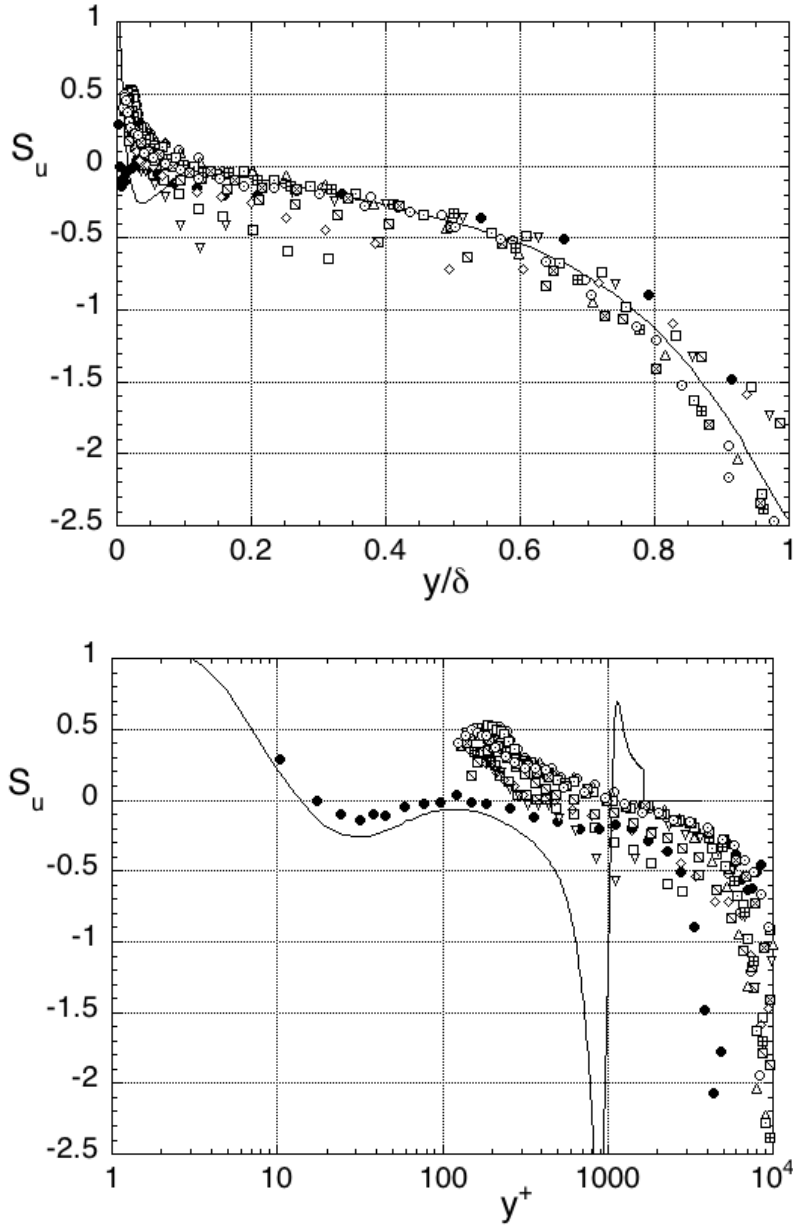


Figure 3.25: Skewness factor, S_u vs. y/δ and y^+ . Symbols: — DNS smooth surface, -- DNS rough surface, • $X=0$, ∇ 0.2, \square 0.7, \diamond 1.2, \boxplus 1.7, \triangle 2.2, \circ 2.7, \boxminus 3.2, \boxtimes 3.8, \boxdot 4.8, \odot 5.66.

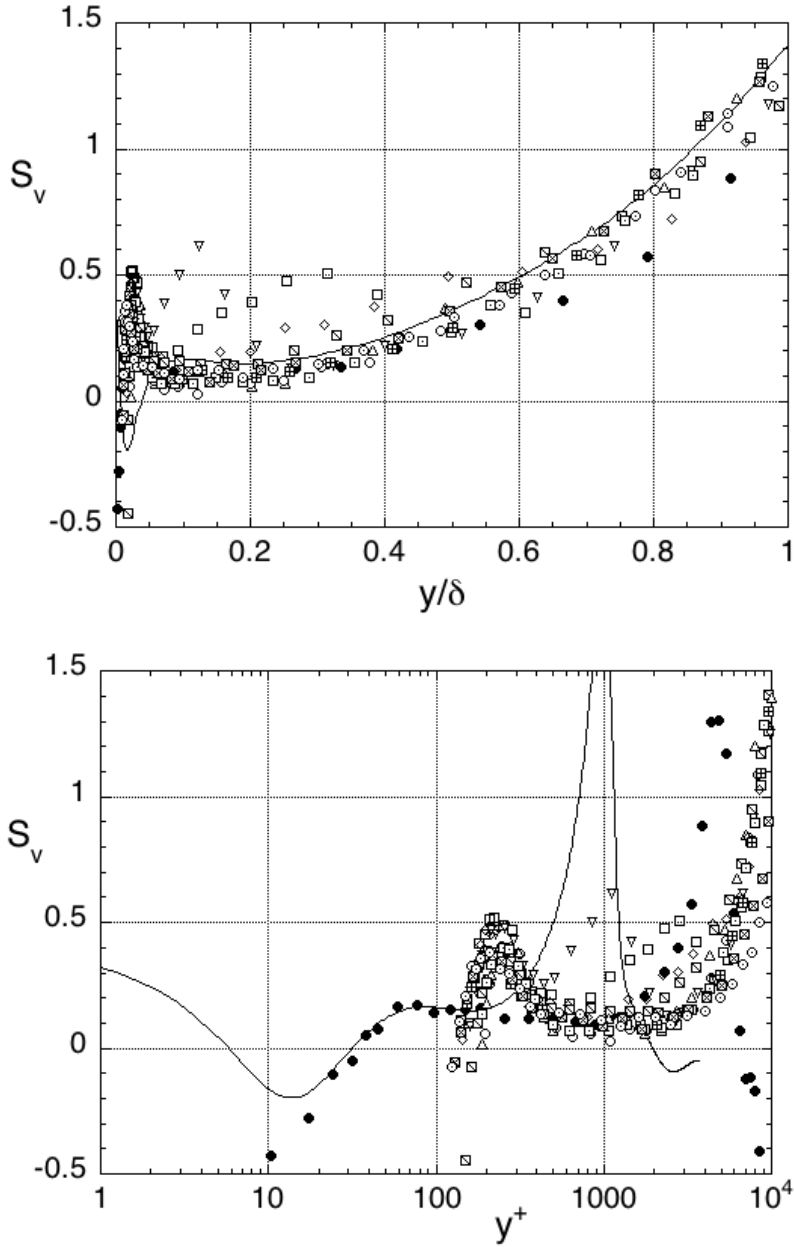


Figure 3.26: Skewness factor, S_u vs. y/δ and y^+ . Symbols: — DNS smooth surface, -- DNS rough surface, \bullet $X=0$, ∇ 0.2, \square 0.7, \diamond 1.2, \boxtimes 1.7, \triangle 2.2, \circ 2.7, \boxdot 3.2, \boxplus 3.8, \boxtimes 4.8, \odot 5.66.

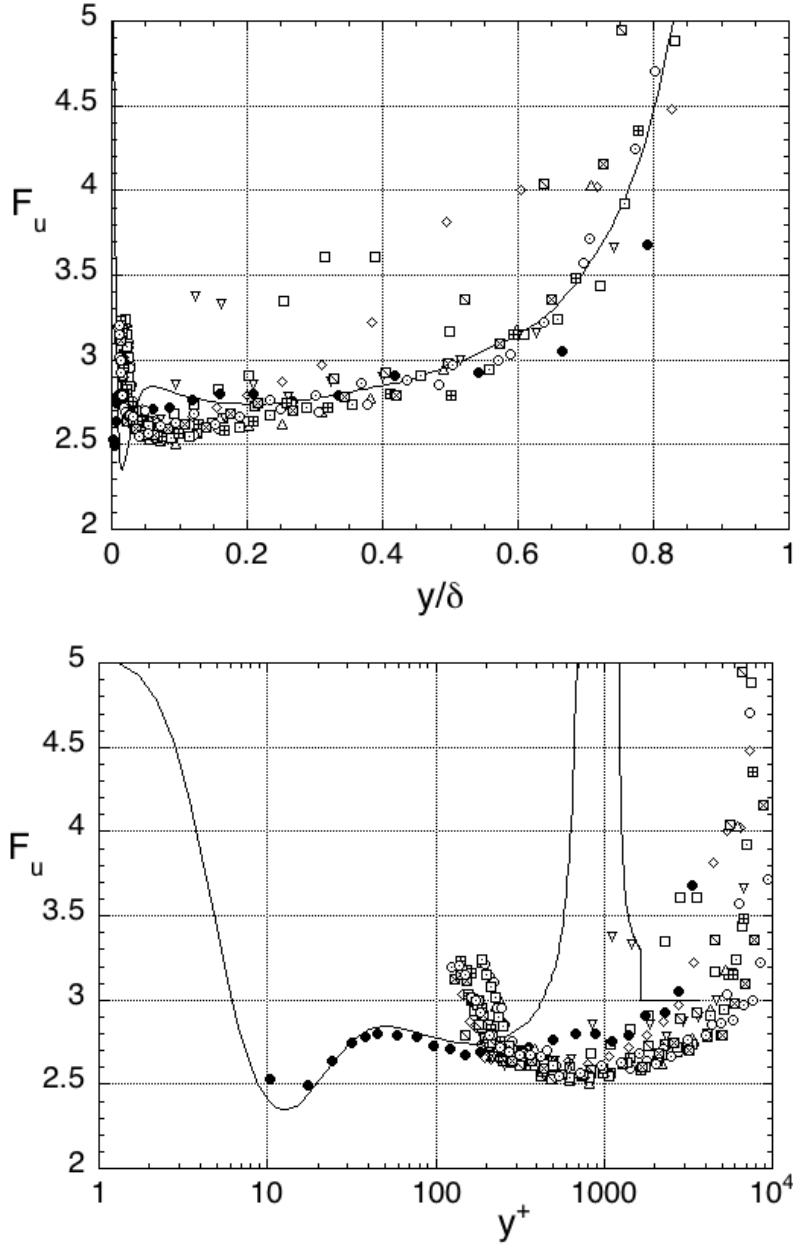


Figure 3.27: Flatness factor F_u vs. y/δ and y^+ . Symbols: — DNS smooth surface, -- DNS rough surface, \bullet $X=0$, ∇ 0.2, \square 0.7, \diamond 1.2, \boxtimes 1.7, \triangle 2.2, \circ 2.7, \square 3.2, \boxplus 3.8, \boxtimes 4.8, \odot 5.66.

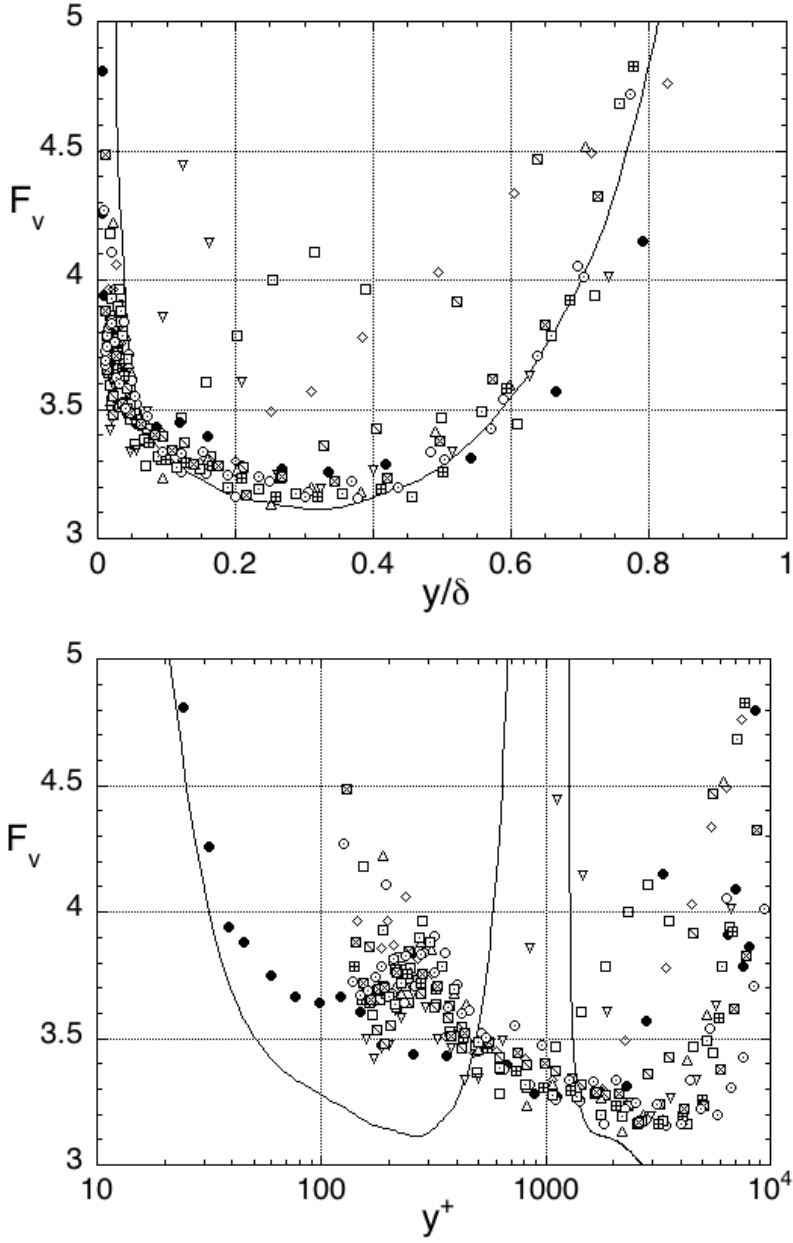


Figure 3.28: Flatness factor F_v vs. y/δ and y^+ . Symbols: — DNS smooth surface, -- DNS rough surface, \bullet $X=0$, ∇ 0.2, \square 0.7, \diamond 1.2, \boxtimes 1.7, \triangle 2.2, \circ 2.7, \square 3.2, \boxplus 3.8, \boxtimes 4.8, \odot 5.66.

3.2.7 Quadrant decomposition

In order to get more details and possible differences in flow structure due to roughness, a quadrant analysis method of Lu & Willmarth (1973), was carried out. The method consist in dividing the Reynolds shear stress in four quadrants according to sign of u and v , see Figure 3.29. The quadrants (Q_3) and (Q_4), 'inward'

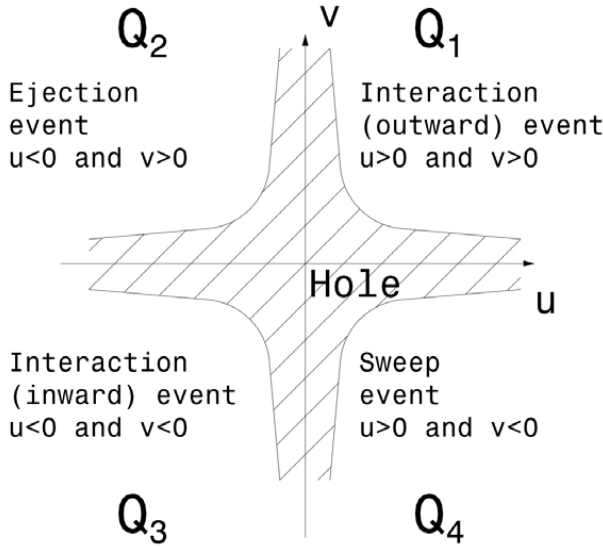


Figure 3.29: Quadrant decomposition (sketch)

interaction and 'sweep' events, contribute to downward transfer of momentum while (Q_1) and (Q_2) are outward transfer of momentum.

The contribution to $\langle uv \rangle$ from a certain quadrant may be written as:

$$(\langle uv \rangle)_Q = \lim_{T \rightarrow \infty} \frac{1}{T} \int_0^T uv \cdot I_Q(t) dt \quad (3.16)$$

where Q denotes the quadrant of interest and I_Q is a trigger function defined as:

$$I_Q(t) = \begin{cases} 1 & \text{when } |uv|_Q \geq H \sqrt{\langle uu \rangle} \sqrt{\langle vv \rangle} \\ 0 & \text{otherwise} \end{cases} \quad (3.17)$$

where H is a hyperbolic hole. The hyperbolic hole H gives us information about the contribution of large $|uv|$ to Reynolds stresses. Figure (3.30) shows the normalized contribution, from ejection and sweeps $H = 0$, to total shear stress. Comparison with Figure (3.18) shows similar shape. Contribution from ejections and sweeps, near the wall, to total shear-stress for $H = 0$ is about the same, $\langle uv_{Q_2}^+ \rangle \approx 0.74$ $\langle uv_{Q_4}^+ \rangle \approx 0.70$. The sum gives us 144%, this indicate that the interaction mechanism will represent $\sim 44\%$. For $y/\delta > 0.3$ and $X > 2.2m$ the smooth- and rough- surfaces

distribution are almost the same. This is in agreement with Flack but not with the data of Keisbulck & Labraga who found that both sweeps and ejections were much affected by the roughness.

Figure (3.31) shows contribution to shear stress due to strong ejection and sweep events $H = 4$. For $H = 4$ the ejections on smooth-surface are almost constant for entire boundary layer, $0.05 < y/\delta < 0.7$. For rough-surfaces, $X > 1.7m$, the ejection events are increasing with the y/δ and for $y/\delta > 0.4$ they are higher than on smooth surface.

The sweep events, for $H = 4$, are very small for smooth and rough-surfaces when $y/\delta > 0.6$ this point out that the sweep events are significant near the wall and are not as dominant as ejection events throughout the entire boundary layer. The profiles in Figure (3.30) show that for the $X > 1.7m$ in the outer layer, $0.2 < y/\delta < 0.6$, the sweep and ejection events are similar for smooth and rough-surfaces. Close to the wall, $y/\delta < 0.2$, there is small differences, for sweep events, between rough and smooth surface both for $H = 0$ and $H = 4$.

Figure (3.32) and Figure(3.33) shows the ratio $\alpha = \langle uv^+ \rangle_{Q2} / \langle uv^+ \rangle_{Q4}$ for $H = 0$ and $H = 4$. Close to the surface the sweep events predominate the ejection events both for smooth surface, $y^+ < 18$, and for rough-surfaces, $y^+ < 200$ ($2k$) for $X = 5.66m$. After $y^+ \approx 18$, for smooth surface, the ejection events start to prevail over sweep events in accordance with the observation from the skewness. In the case of rough-surfaces, $y^+ \approx 200$, is the point after which the ejection events starts to overcome the sweep events. This point is not correlated with change in sign for S_{ii} or maximum value for $\langle uu^+ \rangle$ as for smooth surface which confirm that we have a different mechanism compared with smooth surface.

Apart from the area delimited by the inner layer $X < 2.2m$, α is slightly higher for smooth surface than for rough-surfaces (see Figure 3.32). This difference is more evident for $H = 4$, Figure (3.33), which indicates that ejections on smooth-surface are stronger, more dominant, than for rough surfaces, $X > 1.7m$.

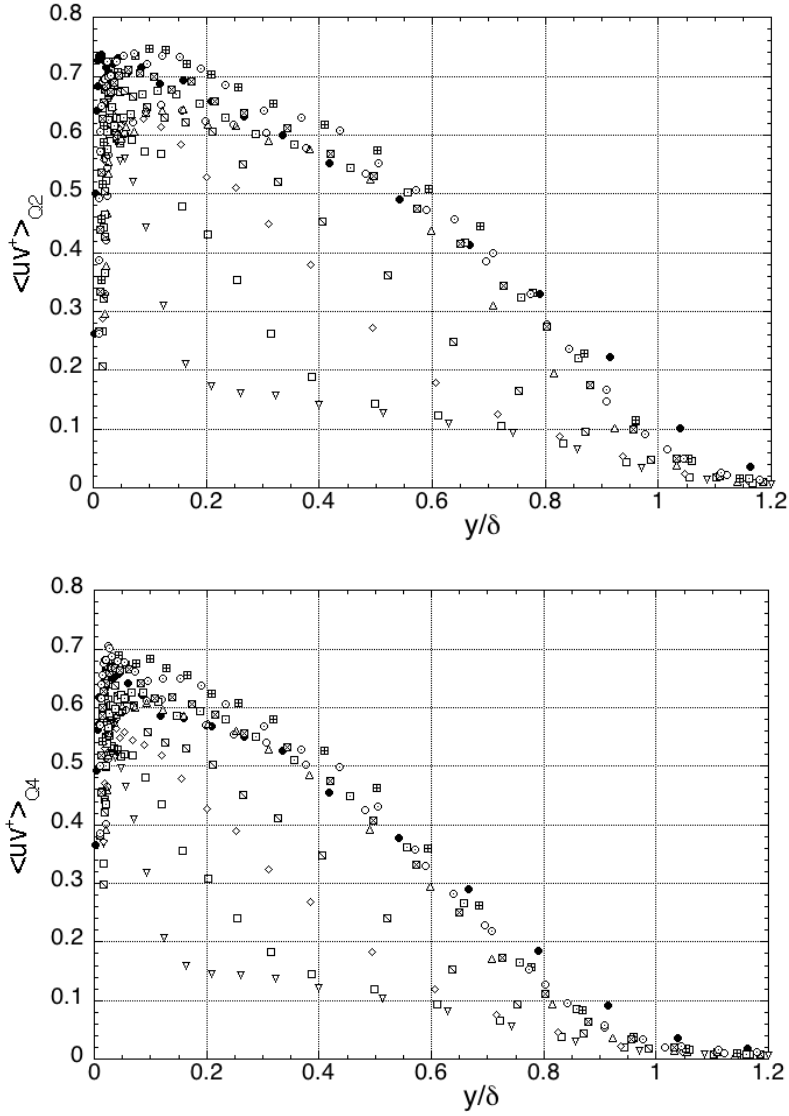


Figure 3.30: Contribution to $\langle uv^+ \rangle$ from quadrant 2 and 4 $H=0$. Symbols: \bullet $X=0$, ∇ 0.2, \square 0.7, \diamond 1.2, \boxplus 1.7, \triangle 2.2, \circ 2.7, \boxdot 3.2, \boxtimes 3.8, \boxplus 4.8, \odot 5.66.

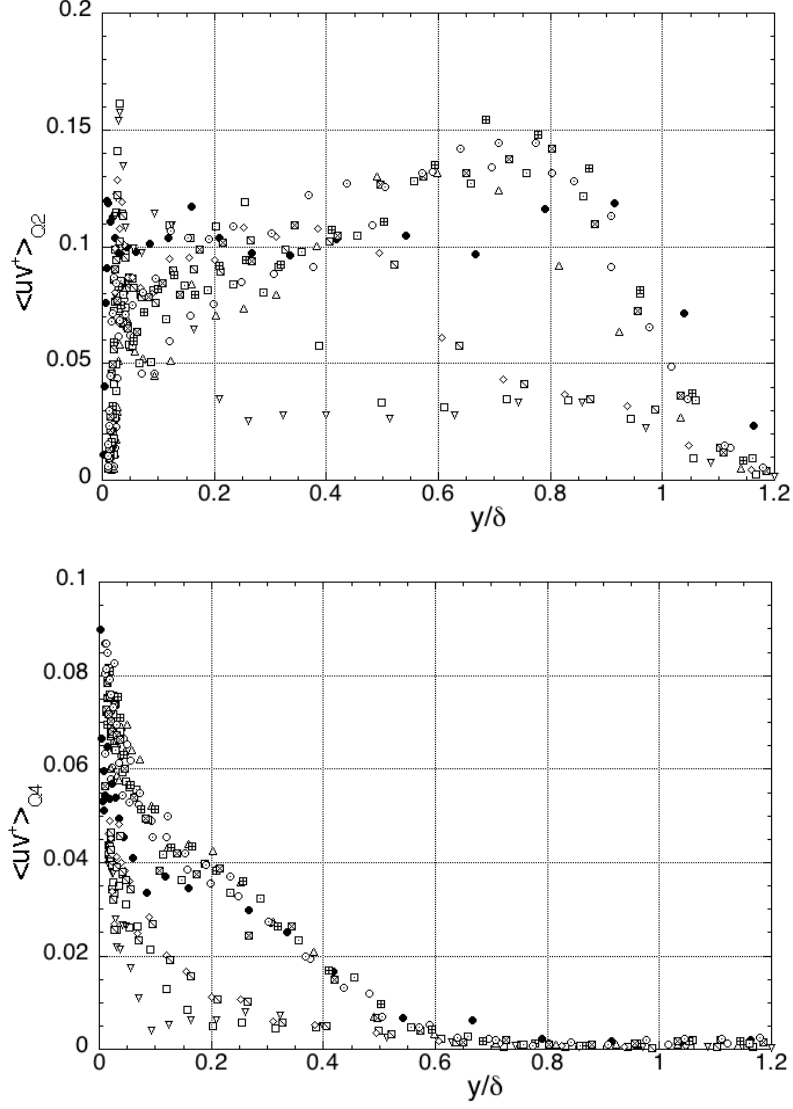


Figure 3.31: Contribution to $\langle uv^+ \rangle$ from quadrant 2 and 4 $H=4$. Symbols: \bullet $X=0$, ∇ 0.2, \square 0.7, \diamond 1.2, \boxplus 1.7, \triangle 2.2, \odot 2.7, \boxplus 3.2, \boxtimes 3.8, \boxtimes 4.8, \odot 5.66.

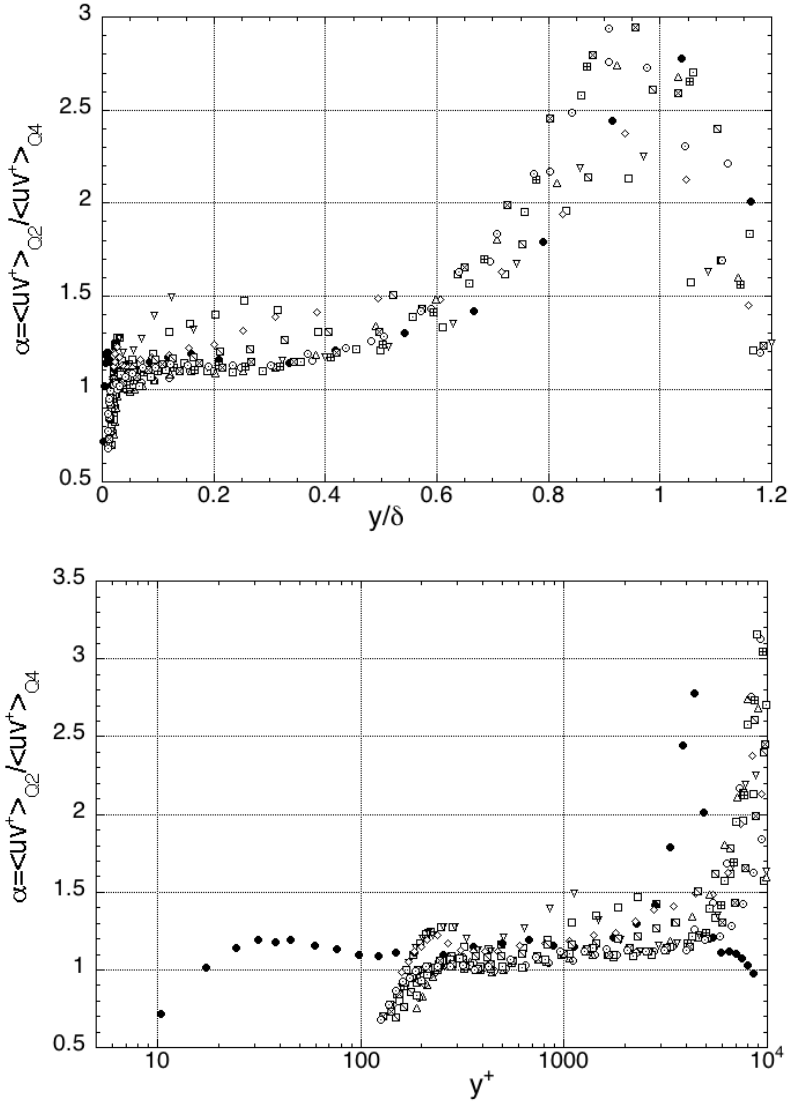


Figure 3.32: Ratio of contribution to $\langle uv^+ \rangle$ from quadrants 2 and 4. $H=0$,. Symbols: \bullet $X=0$, ∇ 0.2, \square 0.7, \diamond 1.2, \boxtimes 1.7, \triangle 2.2, \circ 2.7, \square 3.2, \boxplus 3.8, \boxtimes 4.8, \odot 5.66.

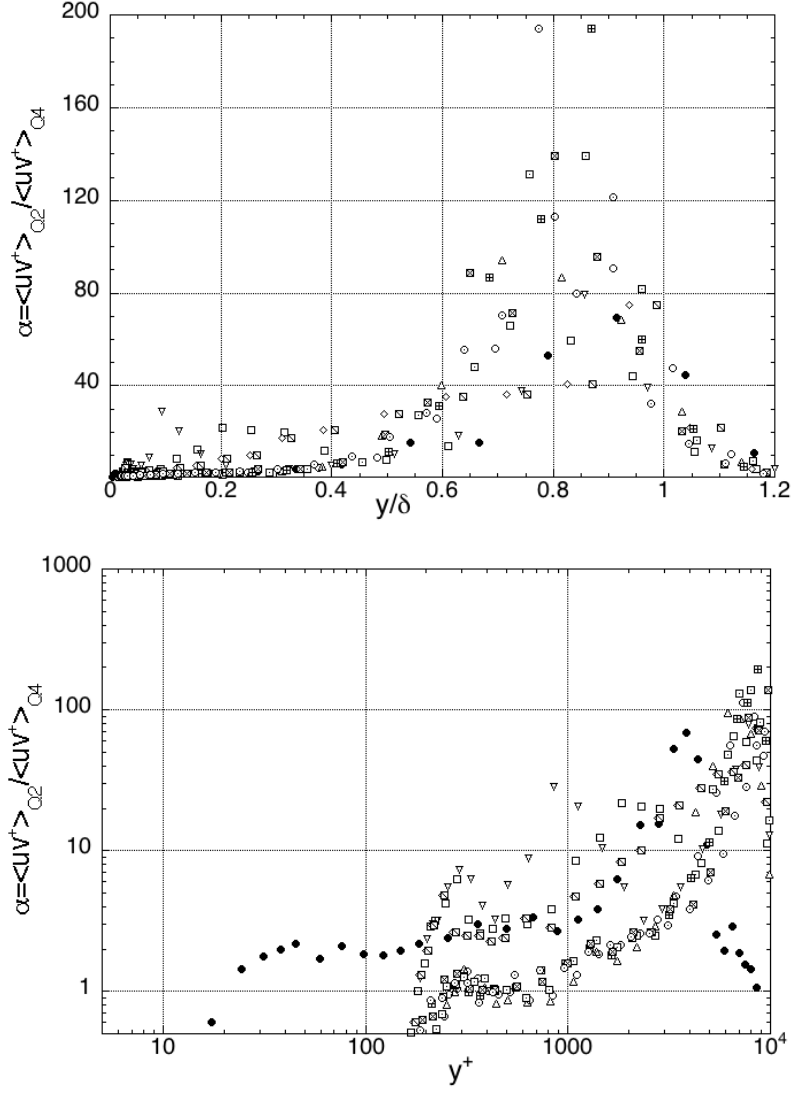


Figure 3.33: Ratio of contribution to $\langle uv^+ \rangle$ from quadrants 2 and 4. $H=4$. Symbols: \bullet $X=0$, ∇ 0.2, \square 0.7, \diamond 1.2, \boxminus 1.7, \triangle 2.2, \circ 2.7, \square 3.2, \boxplus 3.8, \boxtimes 4.8, \odot 5.66.

3.2.8 Conclussions

Studying the effect of surface change from smooth to rough over turbulent boundary layer is the same as studying the flow with two equilibrium conditions. The internal boundary layer is determined by the wall condition and outer layer is determined by the upstream wall condition. Increasing the length, X , of the rough-surface makes the effects, of rough wall, to be diffused outward. After about 18 boundary layer thicknesses over the smooth wall, $X=0$, the flow has adapted to new wall conditions both in mean velocity and Reynolds stresses.

The velocity defect profiles have adjusted to new wall conditions and display similarity for $X > 1.7m$. The effect of the wall condition on the Reynolds stresses, normalized with u_τ , is not noticed beyond the internal boundary layer. The Reynolds stresses are perturbed only in the internal boundary layer.

The perturbation effect on Reynolds stresses can clearly be seen when normalized with U_e . Outside the internal boundary layer Reynolds stresses have the characteristics of the upstream wall condition. The Reynolds stresses, $-\langle uv \rangle$ and $\langle vv \rangle$ normalized with U_e , shows a overshoot for $X < 2.2m$.

For $X \geq 2.2m$ there is good agreement between rough- and smooth-surface in velocity defect form. The Reynolds stresses and high order moments, $X \geq 2.2m$, for smooth and rough-surfaces indicate no differences in the outer layer providing support for similarity hypothesis. This is in agreement with Jimenez (2004) hypothesis. Jimenez suggested that δ/k should be greater than 40, in our experiments $\delta/k > 78$ and $k^+ > 104$, similarity is expected in outer layer.

3.3 References

- A. K. Gupta, R. E. Kaplan, Statistical Characteristics of Reynolds Stress in a Turbulent Boundary Layer, *Phys Fluids* **15**, (6) June, (1972)
- P. R. Bandyopadhyay and R. D. Watson, Structure of rough-wall turbulent boundary layers, *Phys Fluids* **31**, (7) July, (1988)
- L. Keirsbulck, L. Labraga, A. Mazouz and C. Tournier, Surface roughness effects on turbulent boundary layer structure, *J. Fluids Eng.* **124**, (2002), pp. 127–135
- K.A. Flack, M.P. Schulz, and T.A. Shapiro, Experimental support for Townsend's Reynolds number similarity, *Phys. Fluids* **17** 035102, (2005)
- R. A. Antonia, P-A. Krogstad, Turbulent structure in boundary layers over different types of surface roughness, *Fluid Dynamics Research* **28**, (2001), pp. 139-157
- J. Andreopoulos and P. Bradshaw, Measurements of turbulence structure in the boundary layer on a rough surface, *Boundary-Layer Meteorology* **20**, (1980), pp. 201-213
- S. S. Lu and W. W. Willmarth, Measurements of the structure of the Reynolds stress in a turbulent boundary layer, *J. Fluid Mech* **60**, **part 3**, (1973), pp. 481-511
- I. Marusic, N. Hutchins, and R. Mathis, High Reynolds number Effects in Wall Turbulence, *Sixth International Symposium on Turbulence and Shear Flow Phenomena, Seoul, Korea, 22-24 June 2009 Vol III*
- P-Å Krogstad, R. A. Antonia and L. W. Browne, Comparison between rough- and smooth-wall turbulent boundary layer, *J. Fluid Mech* **245**, (1992), pp. 599-617
- P. Schlatter, R. Örlü, Q. Li, G. Brethouwer, J. H. M. Fransson, A. V. Johansson, P. H. Alfredsson and D. S. Henningson, DNS of a turbulent zero-pressure gradient boundary layer, *Phys Fluids* **21**, 051702 (2009)
- R. A. Antonia and R. E. Luxton, The response of a turbulent boundary layer to a step change in surface roughness. Part 1. Smooth to rough, *J. Fluid Mech*, **48**, **part 4**, (1971), pp. 721-761
- J. Jimenez, Turbulent flows over rough walls, *Annu. Rev. Fluid Mech* **36**, (2004), pp. 173-196
- S.-H. Lee and H.J. Sung, Direct numerical simulation of the turbulent boundary layer with rod-roughened wall, *J. Fluids Eng.* **584**, (2007) pp. 125–146
- V. Efros & P-Å. Krogstad, A Skin Friction balance applied to rough wall experiments, *Sixth International Symposium on Turbulence and Shear Flow Phenomena, Seoul, Korea, 22-24 June 2009 Vol II*
- R. H. Shaw and J. Tavangir, D. P. Ward, Structure of the Reynolds Stress in a Canopy Layer, *Journal of Climate and Applied Meteorology* **22**, (1983), pp. 1922-1931
- P-Å. Krogstad, T. Nickels, Turbulent boundary layer with a step change in surface roughness", *Conference on Modelling Fluid Flow (CMFF'06)* (2006)
- H. Cheng and I. P. Castro, "Near-wall flow development after a step change in surface roughness, *Boundary-Layer Meteorology*, **105**, (2002), pp. 411-432

CHAPTER 3. TURBULENT BOUNDARY LAYER OVER A STEP CHANGE: SMOOTH TO ROUGH. LDV MEASUREMENTS

- W. P. Elliot, The growth of the Atmospheric Internal Boundary Layer, *Transactions, American Geophysical Union* **39**, (6), (1958)
- P-Å. Krogstad, H. I. Andersson, O. M. Bakken, and A. Ashrafian, An experimental and numerical study of channel flow with rough walls, *J. Fluid Mech* **530**, (2005), pp. 327-352
- I. P. Castro, Rough-wall boundary layers: mean flow universality, *J. Fluid Mech* **585**, (2007), pp. 469-485
- M. V. Zaragola, A. J. Smits, Mean-flow scaling of turbulent pipe flow, *J. Fluid Mech* **373**, (1998), pp. 33-79
- W.K. George and L. Castillo, Zero-pressure gradient turbulent boundary layer, *Appl. Mech. Rev* **50**, (1997), pp. 689-729
- O. G. Akinlade, D. J. Bergstrom, M. F. Tachie and L. Castillo, Outer flow scaling of smooth and rough wall turbulent boundary layers, *Experiments in Fluids* **37**, (2004), pp. 604-612
- M. Acharya, J. Bornstein and M. P. Escudier, 1986, Turbulent boundary layers on rough surfaces, *Experiments in Fluids* **4**, (1986), pp. 33-47
- D. B. DeGraaff and J. K. Eaton, Reynolds-number scaling of the flat-plate turbulent boundary layer, *J. Fluid Mech* **422**, (200), pp. 319-346
- J. Andreopoulos and P. Bradshaw, The response of a turbulent boundary layer to a short length of surface roughness, *J. Fluid Mech* **118**, (1982), pp. 143-164
- W. Pendergrass and S. P. S. Arya, Dispersion in neutral boundary layer over a step change in surface roughness I. Mean flow and turbulence structure, *Atmospheric Environment* **18**, (7), (1984), pp. 1267-1279
- M. Gad-el-Hak and P. R. Bandyopadhyay, Reynolds number effects in wall-bounded turbulent flows, *Applied Mechanics Reviews* **47**, (8), (1994), pp. 307-367
- M. Metzger, B. J. McKeon and H. Holmes, The near-neutral atmospheric surface layer: turbulence and non-stationarity *Phil. trans. R. Soc. A* **365**, (2007), pp. 859-876
- K. R. Sreenivasan, The turbulent boundary layer, *Frontiers in Experimental Fluid Mechanics*, ed. M. Gad-el-Hak, (1989), pp. 159-209
- J. C. Rotta, Turbulent boundary Layers in Incompressible Flow, In *Progress in Aeronautical Science* **2**, (1962), pp. 1-219
- R. Balachandar and F. Bhuiyan, High-Order Moments of Velocity Fluctuations in an Open-Channel flow with Large Bottom Roughness, *Journal of Hydraulic Engineering*, **133**, (1), (2007), pp. 77-87
- F. Fernholz and P. J. Finley, The incompressible zero-pressure-gradient turbulent boundary layer : an assessment of the data, *Progress in aerospace science* vol 32, (32), (1996), pp. 245-311
- P. R. Bandyopadhyay, Reynolds number dependence of the Freestream Turbulence Effects on turbulent Boundary Layers, *AIAA Journal* **30**, (7), (1992), pp. 1910-1911
- P. Schlatter and R. Örlü 2010, Assessment of direct numerical simulation data of

turbulent boundary layers, *J. Fluid Mech* **659**, (2010), pp. 116-126
Boundary Layer DNS/LES Data
[http : //www.mech.kth.se/ pschlatt /DATA/README.html](http://www.mech.kth.se/pschlatt/DATA/README.html)

Chapter 4

Turbulent boundary layer over a step change: smooth to rough. PIV measurements

Further progress and understanding of the effect on the flow from a perturbation at the wall can be achieved by studying the flow structure using two point correlations. In addition the impact of perturbation at the wall on small and large scales is obtained through POD analysis.

4.1 Experimental set-up

The experimental set-up is the same as for LDA measurements. The experimental test conditions are given in Tabel (4.1). Two-dimensional PIV measurements were performed in $x - y$ plane at the same position with the LDA measurements. The flow was seeded with smoke particles, $\sim 1\mu m$ in diameter, generated with SAFEX F2010 Fog generator. The flow is illuminated using a Nd: YAG laser from New Wave Research (532nm 15Hz 120mJ). The laser sheet was directed through a slot in the roof of the tunnel, as shown schematically in Figure (4.1). An 80C60 Flow Sense 2M camera, with 1600×1186 pixel resolution, was used to capture the images. Nikkor 60mm $f2.8$ lenses were used with camera. The field of view was $100 \times 80 \text{ mm}^2$ equivalent to $0.78\delta \times 0.64\delta$ for $X = 0$ and $0.46\delta \times 0.37\delta$ for $X = 5.66m$. In order to measure the entire boundary layer the camera was translated in vertical direction four times for $X = 5.66m$ and three times for the other cases. For each position 2500 image pairs were acquired.

The interrogation window was kept constant for all measurements ($32 \times 32 \text{ pixels} \sim 2.13 \times 2.13 \text{ mm}^2$). In wall units the window size for $X = 0$ and $X = 5.66m$ is 85 and 141 units respectively, corresponding to Re_τ of 5014 and 14438. The vector field calculation was done with a 50% overlap using FlowManager v 4.71. The particle displacement was determined using adaptive correlation technique with high accuracy sub-pixel scheme.

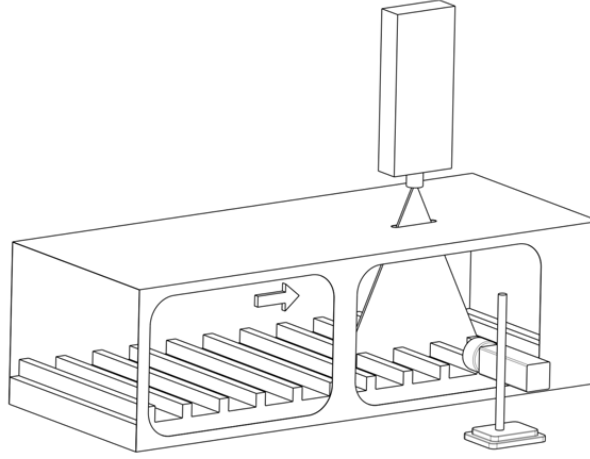


Figure 4.1: PIV setup.

Table 4.1: Parameters for experiment. The symbols used for the plots.

Case	Symbol	X[m]	Wall	u_e	Re_θ	δ/k
1	•	0.00	smooth	17.5	16251	-
2	▽	0.19	rough	17.6	17410	77.1
3	□	0.70	rough	17.7	18666	75.3
4	◇	1.20	rough	17.7	19825	78.0
5	▣	1.70	rough	17.7	21526	76.9
6	△	2.20	rough	18.1	23245	79.6
7	○	2.70	rough	17.6	23546	82.6
8	▣	3.20	rough	17.8	25437	86.3
9	⊙	5.66	rough	17.0	34774	128.4

4.2 Results

4.2.1 Validation of mean profiles

The skin friction velocity for the smooth case was determined using the Clauser chart method. For all the rough cases the skin friction was estimated using the C_f obtained from the balance in the LDA measurements. The comparison between LDA and PIV measurement of mean profiles for $X = 0$ and $X = 5.66 m$ is shown in Figure (4.2). The agreement between the mean profiles obtained with PIV and LDA indicates that the friction velocity was determined correctly.

The velocity defect-profiles plotted as a function of y/δ and y/Δ , $\Delta = \delta^* \cdot u_e/u_\tau$,

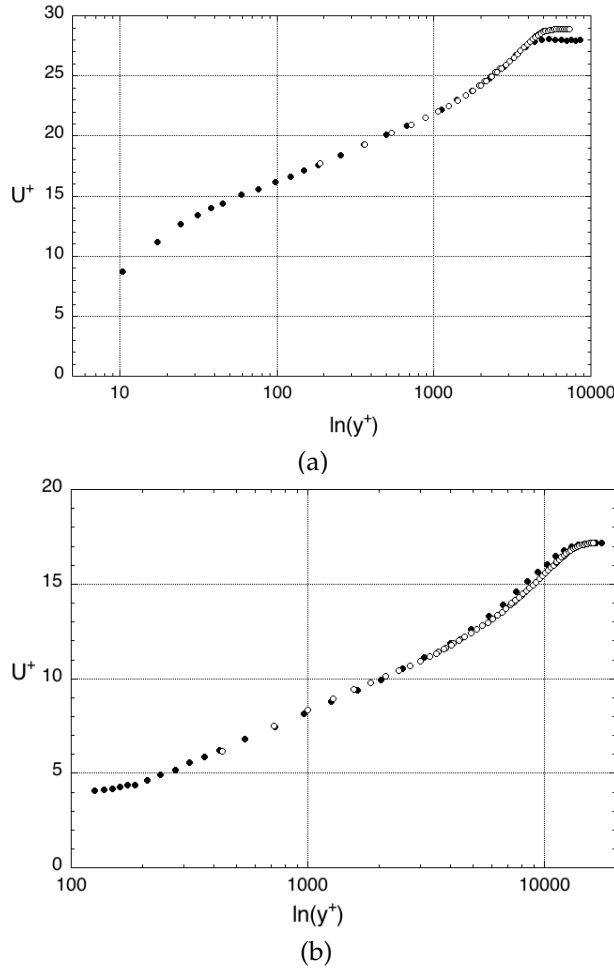
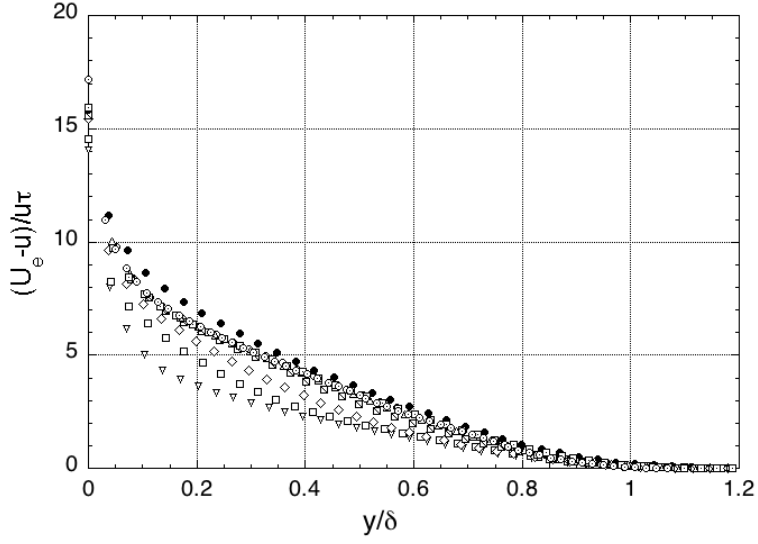


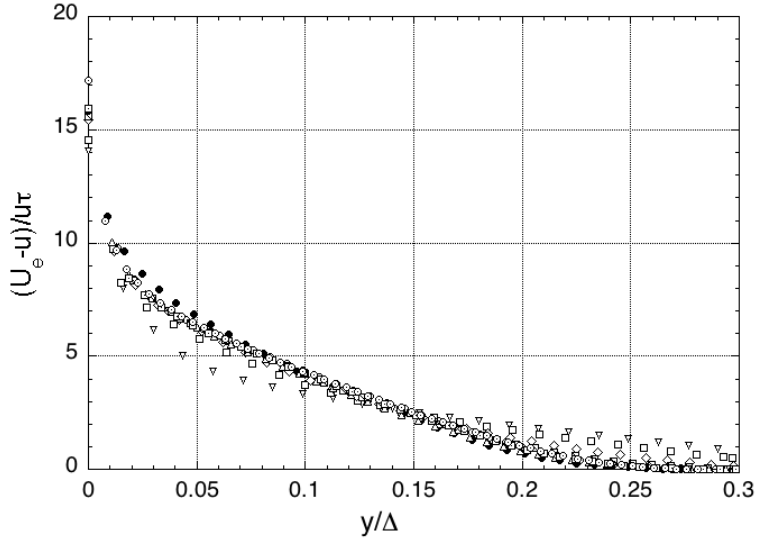
Figure 4.2: Mean velocity profiles inner scalings. a) $X = 0$ smooth, b) $X = 5.66$ full rough. Symbols: \bullet LDA measurements, \circ PIV measurements.

CHAPTER 4. TURBULENT BOUNDARY LAYER OVER A STEP CHANGE: SMOOTH TO ROUGH. PIV MEASUREMENTS

are shown in Figure (4.3). It shows that the differences in velocity profile are decreasing when increasing the length, X , of rough surface. Differences between $X = 5.66\text{ m}$ and $X = 0$ at $y/\delta \leq 0.4$ indicate that the effect on the flow of this two surfaces are different. The comparison between the displacement thickness δ^* and momentum thickness θ obtained with PIV and LDA are presented in Figure (4.4). The agreement for momentum thickness is better than displacement thickness.

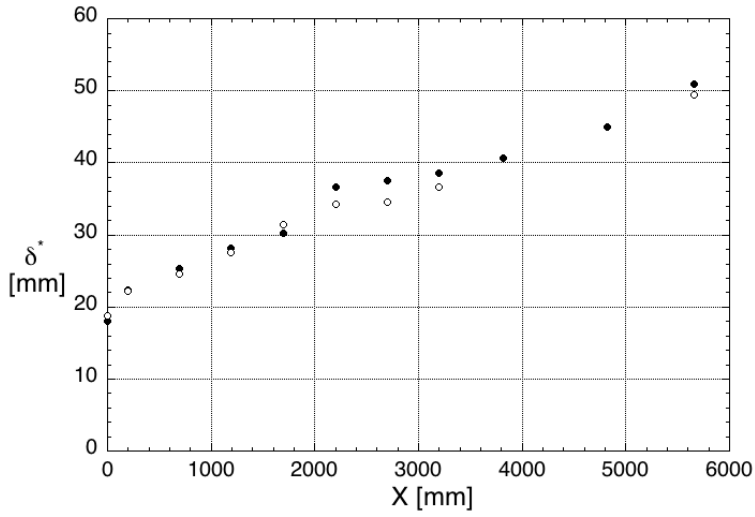


(a)

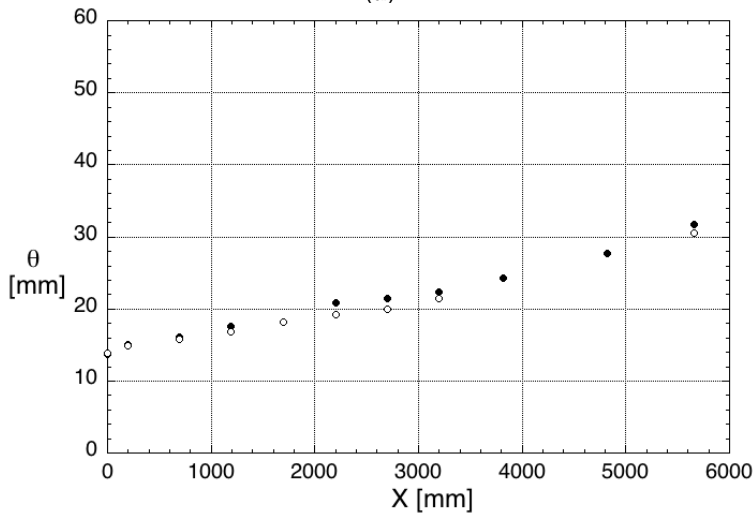


(b)

Figure 4.3: Velocity-defect profiles, vs . y/δ and y/Δ . Symbols: \bullet $X=0$, ∇ 0.2, \square 0.7, \diamond 1.2, \boxtimes 1.7, \triangle 2.2, \circ 2.7, \boxdot 3.2, \odot 5.66.



(a)



(b)

Figure 4.4: Distribution of δ^* and θ . • LDA measurements, ○ PIV measurements

4.2.2 Effects of spatial resolution

The Reynolds stresses comparison between LDA and PIV measurements are shown in Figure (4.5) to Figure (4.8). It is apparent that the PIV has failed to solve the near wall region for u and v fluctuations mainly due to the spatial resolution problem.

The effect of spatial resolution is obviously more visible for the normal stresses $\langle vv \rangle$. This is expected because the energy for the wall normal component is mainly in small scales and when increasing the Reynolds number the small scales become smaller.

The ability of PIV system to resolve small scales is limited by the spatial resolution or the measurement volume. Scales smaller than the measurement volume cannot be resolved. This can lead to significant errors in the measurements of the velocity field.

The measurement volume is defined by the interrogation area and the time delay, dT , between image pairs. The interrogation area was kept constant for all cases, 32×32 pixels. The time delay was adjusted such that the displacement between images was kept in the limits of 5 to 11 pixels.

Increasing the spatial resolution from 32×32 pixels to 16×16 pixels has shown only small differences. This is considered to be the extra noise introduced by smaller interrogation area.

From Figure (4.5) it is evident that the agreement between LDA and PIV measurements is good for $X = 0, 0.2, 0.7 m$ and $X = 5, 66 m$ but not for the ones between. This indicates that the differences are not only due to the resolution problem.

Since the experimental set up is almost the same for all cases the only issues that can make a difference are background noise, velocity gradient and the seeding density.

A velocity gradient within the interrogation area increases the chance that either the initial or the final particle position will be outside the interrogation area which will result in biased data. The displacement will be biased to a lower value because particle with small displacement will be more frequent than those with higher displacement Raffel *et al.* (1998). Increasing the seeding density can solve this problem. A high seeding density correlated with small interrogation area will decrease the uncertainty of the measurement and increase the valid detection rate (see Raffel *et al.* (1998)).

Because of these problems the analysis of the PIV data are concentrated on the outer layer at the reference distance from the wall $y/\delta = 0.4$.

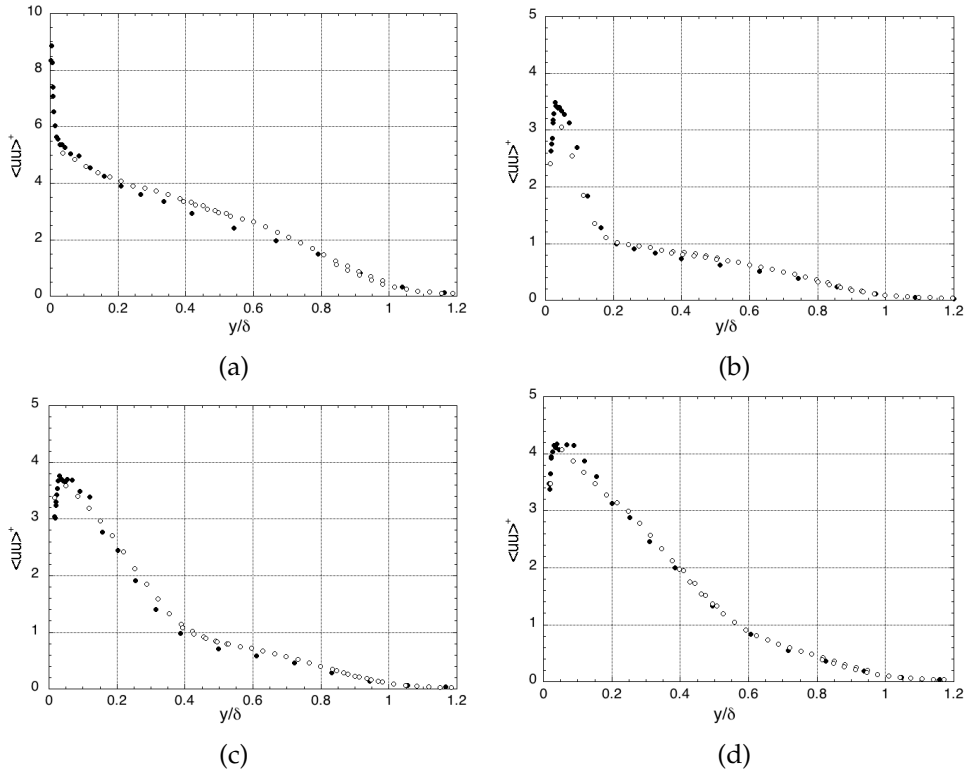


Figure 4.5: Streamwise Reynolds stresses $\langle uu^+ \rangle$, a) $X = 0$, b) $X = 0.2$, c) $X = 0.7$, d) $X = 1.2$. • LDA measurements, ○ PIV measurements

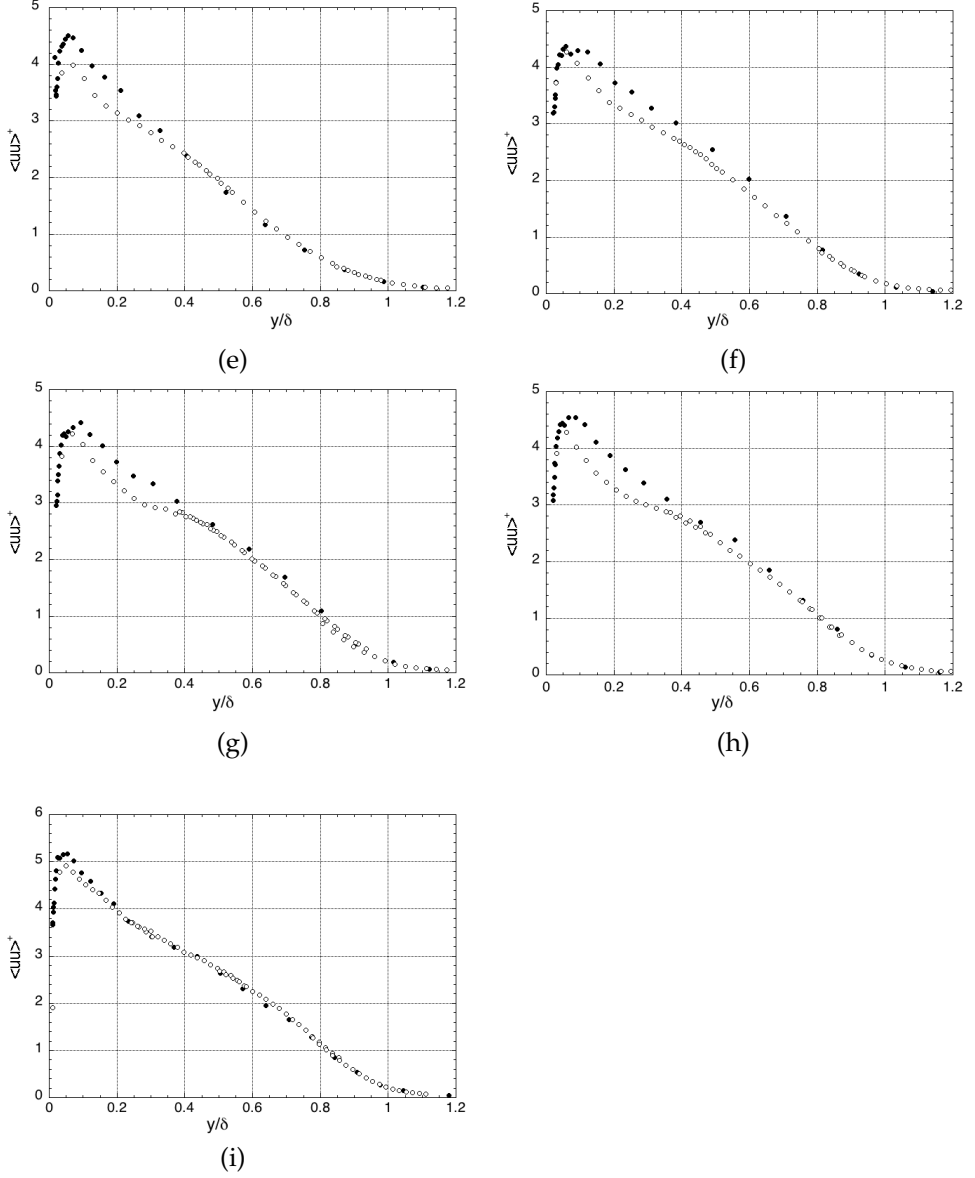


Figure 4.6: Streamwise Reynolds stresses $\langle uu \rangle^+$, e) $X = 1.7$, f) $X = 2.2$, g) $X = 2.7$, h) $X = 3.2$, i) $X = 5.66$. • LDA measurements, o PIV measurements

CHAPTER 4. TURBULENT BOUNDARY LAYER OVER A STEP CHANGE: SMOOTH TO ROUGH. PIV MEASUREMENTS

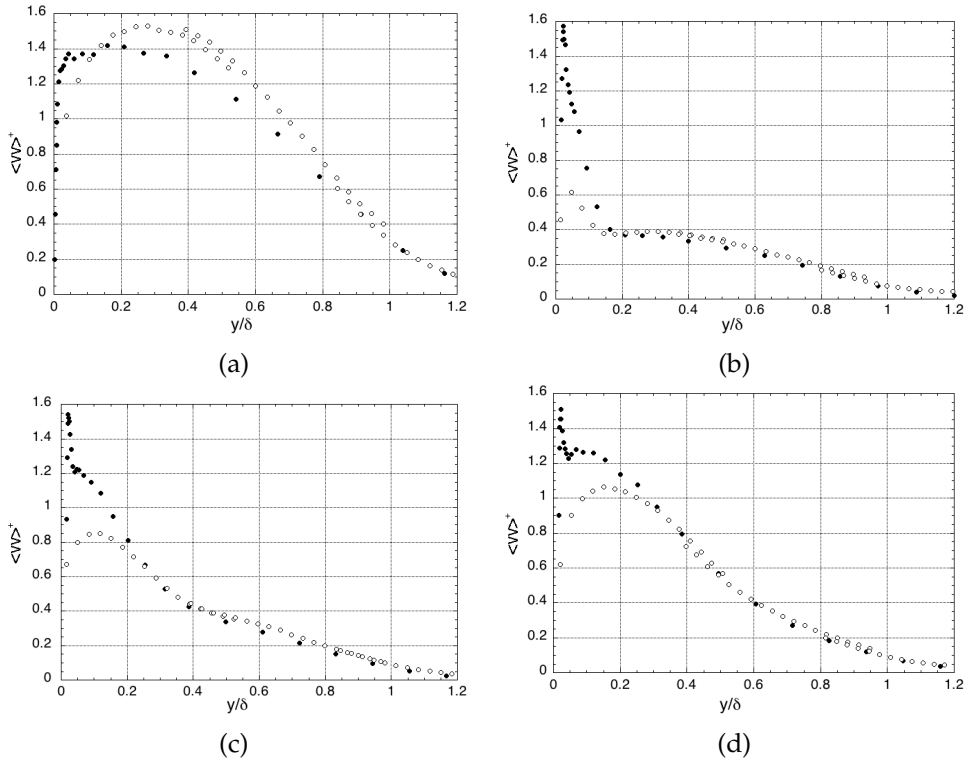


Figure 4.7: Normal Reynolds stresses $\langle vv^+ \rangle$, a) $X = 0$, b) $X = 0.2$, c) $X = 0.7$, d) $X = 1.2$. • LDA measurements, ○ PIV measurements

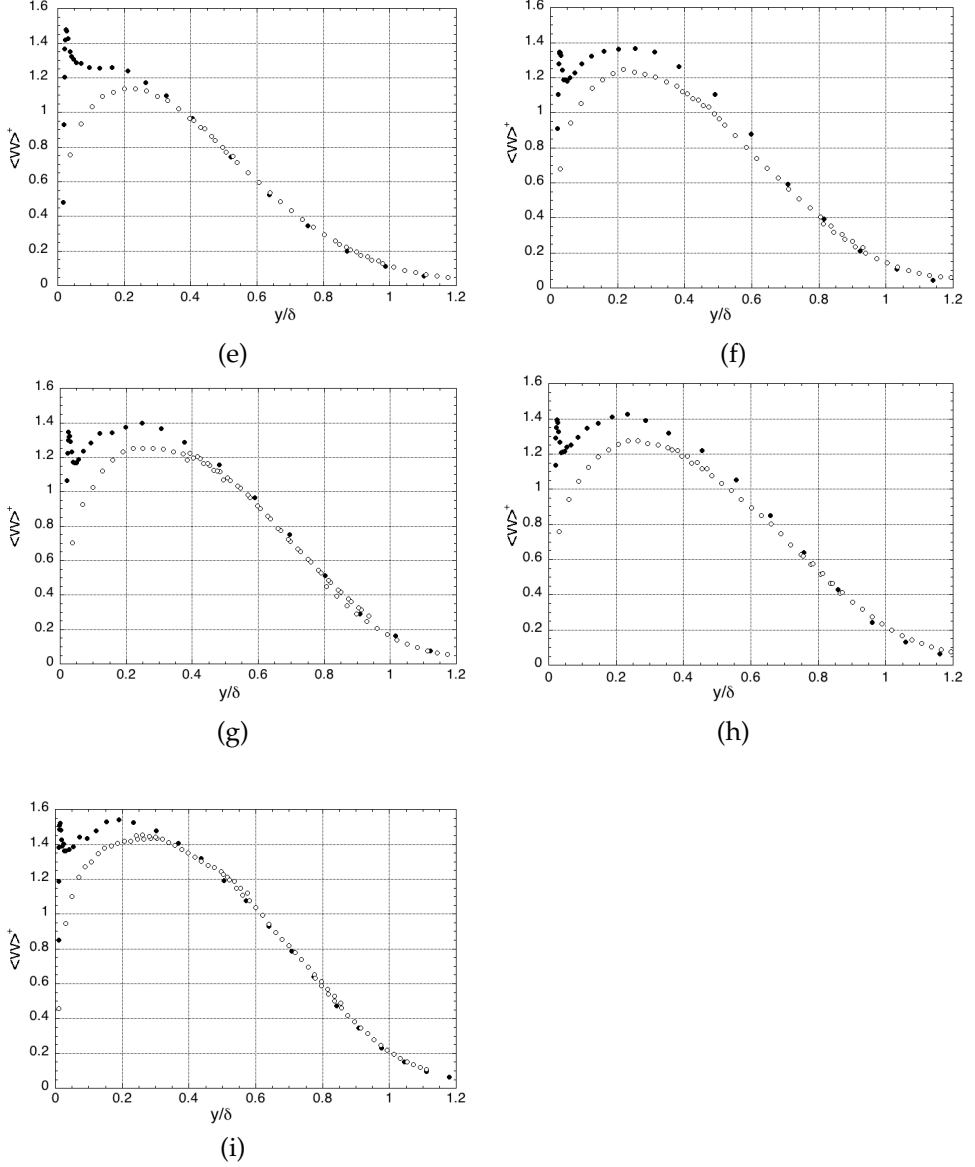


Figure 4.8: Normal Reynolds stresses $\langle vv^+ \rangle$, e) $X = 1.7$, f) $X = 2.2$, g) $X = 2.7$, h) $X = 3.2$, i) $X = 5.66$. • LDA measurements, o PIV measurements

4.2.3 Two-point correlations

The two point-correlation are defined by,

$$R_{pq}(x, y_{ref}) = \frac{\langle q(x, y_{ref})p(x + \Delta x, y + \Delta y) \rangle}{\sigma_q(x, y_{ref})\sigma_p(x, y_{ref})} \quad (4.1)$$

where p and q are the velocity fluctuations separated in the streamwise direction by Δx and in wall normal direction by Δy , σ_p and σ_q are standard deviations of p and q quantities.

Figure (4.9) and Figure (4.10) presents the two-point correlation, R_{uu} , contours at $y/\delta = 0.4$ for all cases. Visual investigation of R_{uu} contours do not reveal too much information. All the contours are elongated in the streamwise direction and slightly tilted away from the wall.

Figure (4.12) presents the slices through the correlations presented in Figure (4.9) and Figure (4.10). The 2 – D slices of R_{uu} , $X > 0$, show good agreement with the smooth surface in streamwise and wall-normal direction. This indicate that the change in roughness has no effect on R_{uu} .

The R_{uu} in Figure (4.12) reaches a value ~ 0.2 at $\Delta X = 0.8\delta$, $X = 0$ and a value of ~ 0.4 at $\Delta X = 0.8\delta$, $X = 5.66m$. This indicates that the size of experimental domain is not enough to capture the elongated tail of autocorrelation.

The R_{uu} contours can be examined in more details by computing the length scales Lx_{uu} and Ly_{uu} . The streamwise and wall-normal extent of R_{uu} , based on contour $R_{uu} = 0.7$, is illustrated in Figure (4.11). The distance Lx_{uu} is defined as in Christensen & Wu (2005), Volino *et al.* (2007) as twice the distance from the self-correlation peak to the most downstream location on a particular contour. There is no clear effect on Lx_{uu} when $X > 0.2m$. If the contour $R_{uu} = 0.6$ is used, the Lx_{uu}/δ for smooth surface will increase to 0.4 for $y/\delta = 0.1$, 0.49 for $y/\delta = 0.4$ and 0.45 for $y/\delta = 0.6$. These values are in good agreement with the value of 0.43 obtained by Volino *et al.* (2007), between $y/\delta = 0.1$ and $y/\delta = 0.6$. The wall normal extent of R_{uu} is determined as in Volino *et al.* (2007), based on the wall normal distance between the points closest and farthest from the wall on a particular contour. Similar to the Lx_{uu} there is no clear effect on the Ly_{uu} for $X > 0.2$.

For isotropic turbulence Frenkiel (1948) showed that the longitudinal scale of turbulence is equal to twice the transverse scale of turbulence.

The ratio of Lx_{uu}/Ly_{uu} for $y/\delta = 0.4$ vary between 2.2 for $X = 0$ and 2.05 for $X = 5.66m$. For both rough and smooth-wall Volino *et al.* (2007) reported a value of 2.5. Nakagawa & Hanratty (2001) reported a value of 2.8 for smooth wall and 3.4 for a flow over a wave wall. For the same type of roughness but lower Reynolds number, $Re_\theta = 4260$, Volino *et al.* (2009) found a value of ~ 2.14 which is in good agreement with our result. Hence, the R_{uu} indicate a tendency towards isotropy caused by 2-D roughness in agreement with results of Krogstad & Antonia (1994).

The inclination angle for R_{uu} which should be related to the inclination of vortex

structure was determined by fitting an ellipse through the points of R_{uu} contours see Figure (4.15). In the present study the ellipse was fitted only to contour levels 0.7. The inclination angle of R_{uu} , β is presented in Figure (4.15). A clear trend is not evident and the angle appears to be insensitive to the length, X , of the rough surface and is approximately 8° . Based on contours level, $R_{uu} = 0.5$, Volino *et al.* (2007) found 13° for smooth surface and 15.8° for rough surface while Wu & Christensen (2010) found an angle of 9° for $y/\delta = 0.1$, which increases with the wall-normal position, 13° for $y/\delta = 0.4$. It is difficult to compare the results because the angle depends on the length scale associated with it. (see Krogstad & Kaspersen 2002)

Figure (4.11) and Figure (4.12) presents the two-point correlation, R_{vv} , contours at $y/\delta = 0.4$. The R_{vv} is less elongated in streamwise directions compared with R_{uu} . It appears that the increase of rough surface X does not affect the R_{vv} . Figure (4.17) shows the one-dimensional profiles of R_{vv} in the streamwise and wall normal directions. The profiles of R_{vv} indicate that the change in surface condition, moving from smooth surface $X = 0$ towards fully rough surface $X = 5.66 m$, has no effect on the small scales in streamwise and wall normal direction.

The length scales Lx_{vv} and Ly_{vv} , defined as Lx_{uu} and Ly_{uu} , for $R_{vv} = 0.7$ are presented in Figure (4.16). The ratio Lx_{vv}/Ly_{vv} , for $y/\delta = 0.4$, vary between 0.67 for $X = 0$ and 0.76 for $X = 5.66 m$. This value is less than the value of 0.8 obtained by Volino *et al.* (2007) and 0.85 obtained by Nakagawa & Hanratty (2001) for $R_{vv} = 0.5$. The discrepancy in value may be attributed to the uncertainty in measurements and due to the different contour level used.

Figure (4.18) presents the comparison between the R_{uu} and R_{vv} obtained with PIV and LDA at $y/\delta = 0.4$ for $X = 0$, $X = 3.2 m$ and $X = 5.66 m$. The R_{uu} and R_{vv} from LDA measurement are calculated using the Taylor's hypothesis with mean velocity as convection velocity. The agreement between PIV and LDA results is quite good with a difference less than 10%. This indicates that the Taylor's hypothesis is valid for rough surface.

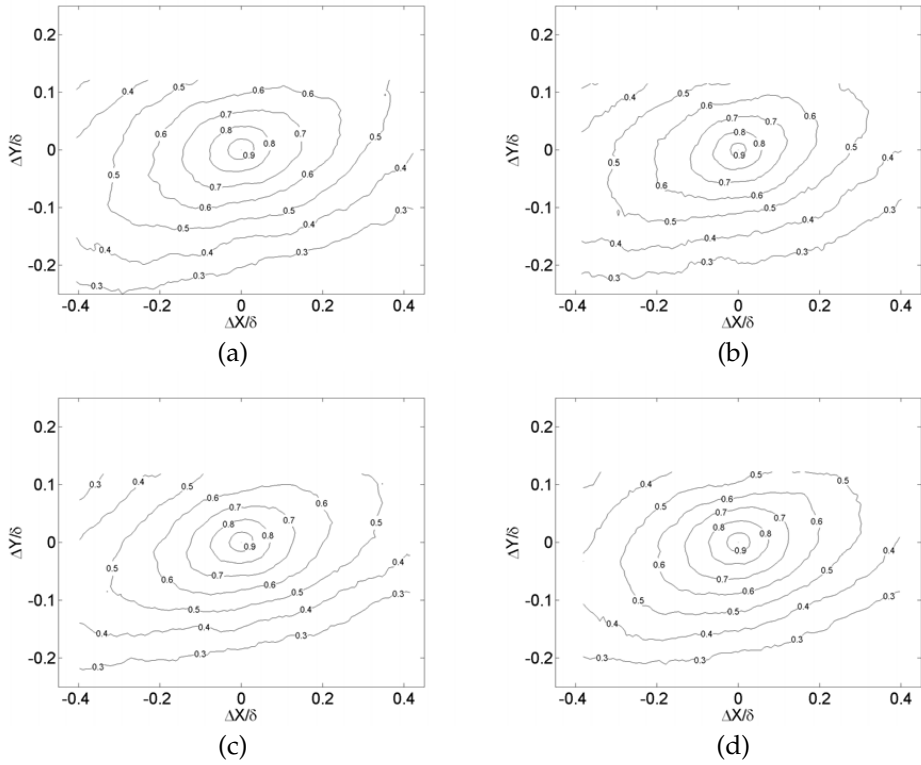


Figure 4.9: Velocity correlation coefficients R_{uu} for $y/\delta = 0.4$, a) $X = 0$, b) $X = 0.2$, c) $X = 0.7$, d) $X = 1.2$

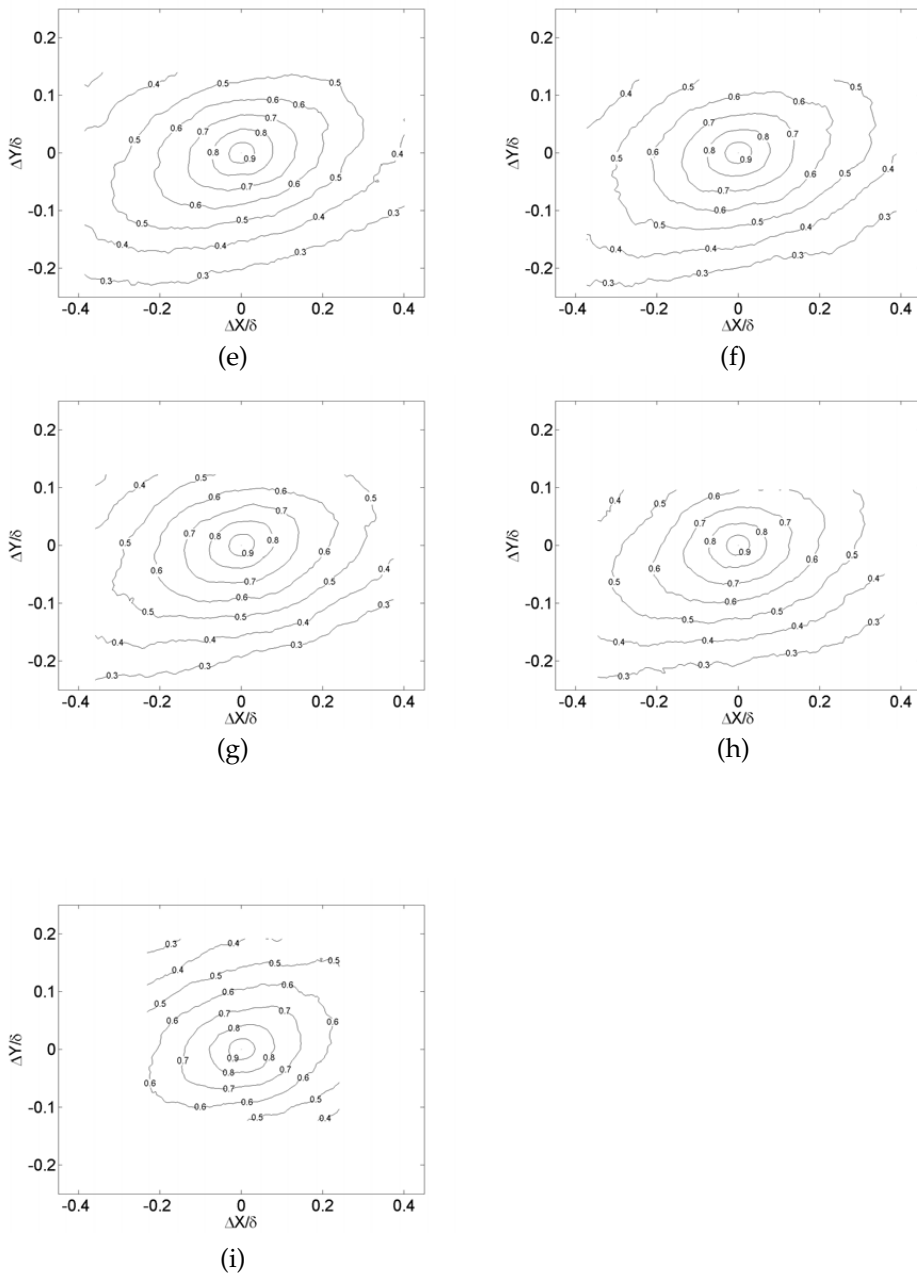


Figure 4.10: Velocity correlation coefficients R_{uu} for $y/\delta = 0.4$, e) $X = 1.7$, f) $X = 2.2$, g) $X = 2.7$, h) $X = 3.2$, i) $X = 5.66$

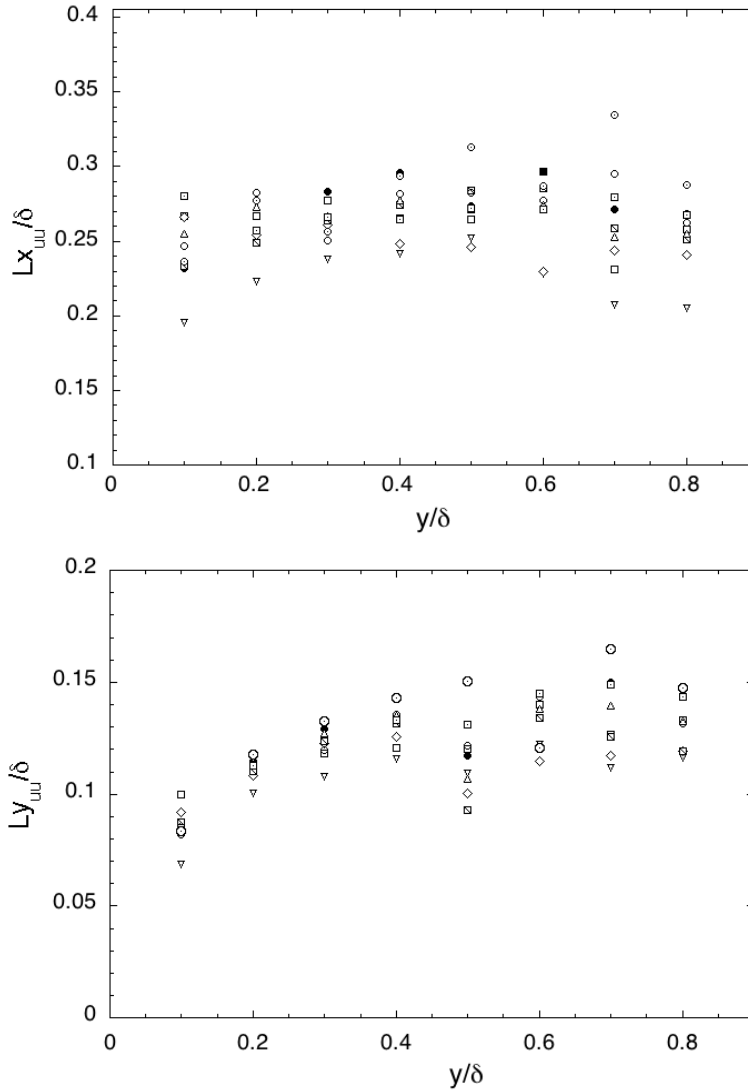


Figure 4.11: Streamwise and wall normal extent of $R_{uu} = 0.7$. Symbols: \bullet $X=0$, ∇ 0.2, \square 0.7, \diamond 1.2, \boxtimes 1.7, \triangle 2.2, \odot 2.7, \boxplus 3.2, \ominus 5.66.

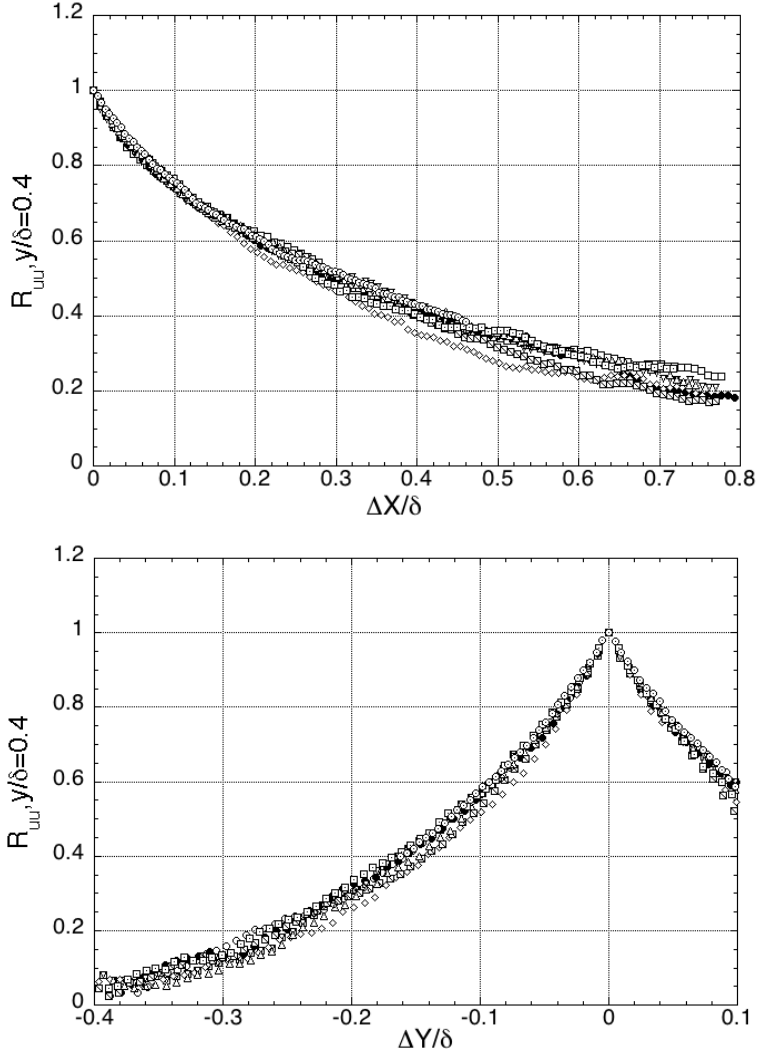


Figure 4.12: One dimensional profiles of R_{uu} . Symbols: \bullet $X=0$, ∇ 0.2, \square 0.7, \diamond 1.2, \boxtimes 1.7, \triangle 2.2, \circ 2.7, \boxdot 3.2, \odot 5.66.

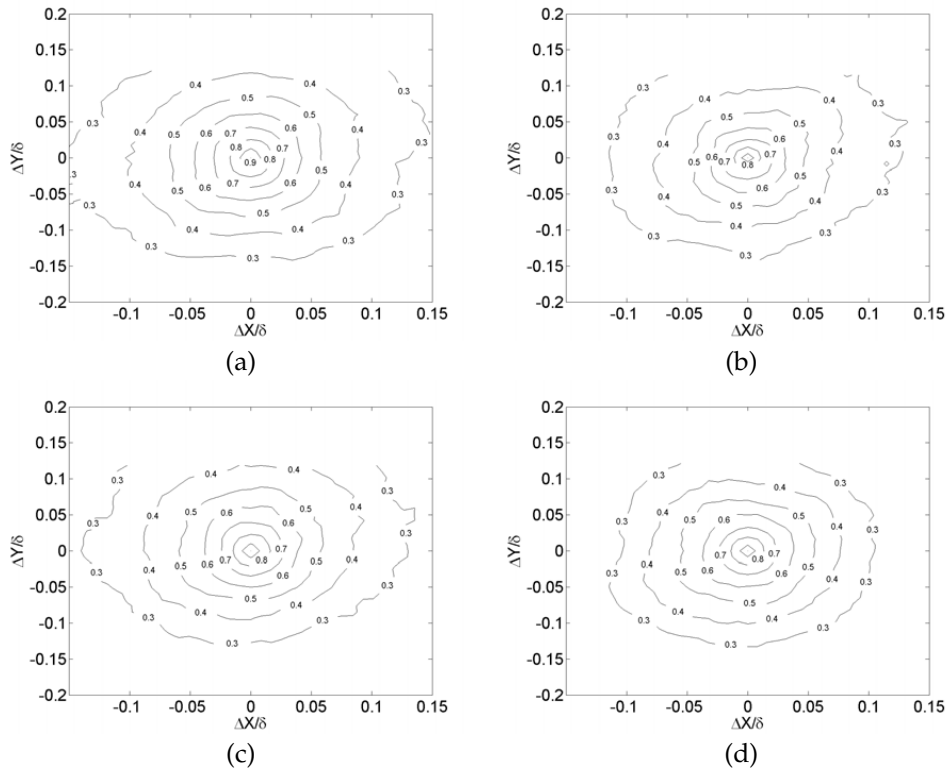


Figure 4.13: Velocity correlation coefficients R_{vv} for $y/\delta = 0.4$, a) $X = 0$, b) $X = 0.2$, c) $X = 0.7$, d) $X = 1.2$

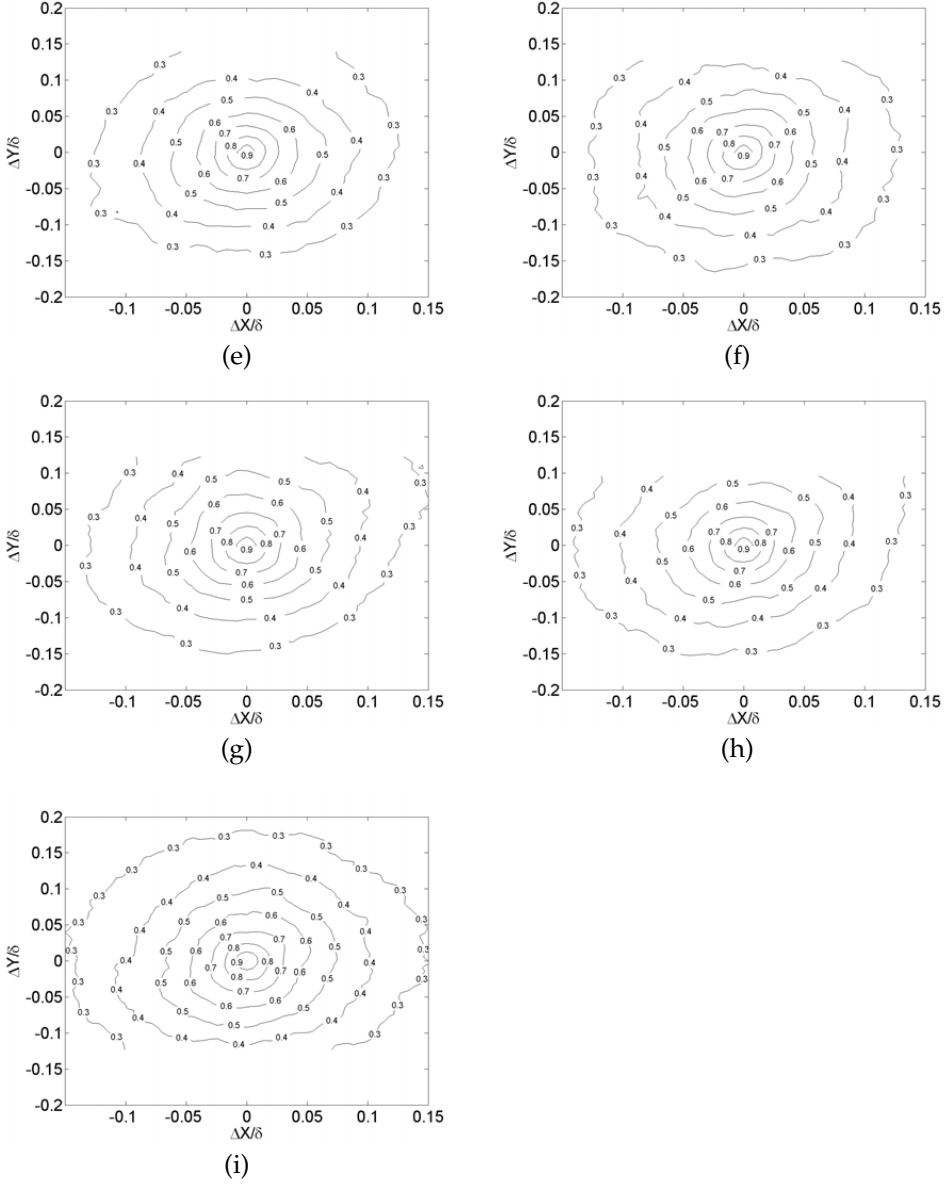


Figure 4.14: Velocity correlation coefficients R_{vv} for $y/\delta = 0.4$, $e)X = 1.7$, $f)X = 2.2$, $g)X = 2.7$, $h)X = 3.2$, $i)X = 5.66$

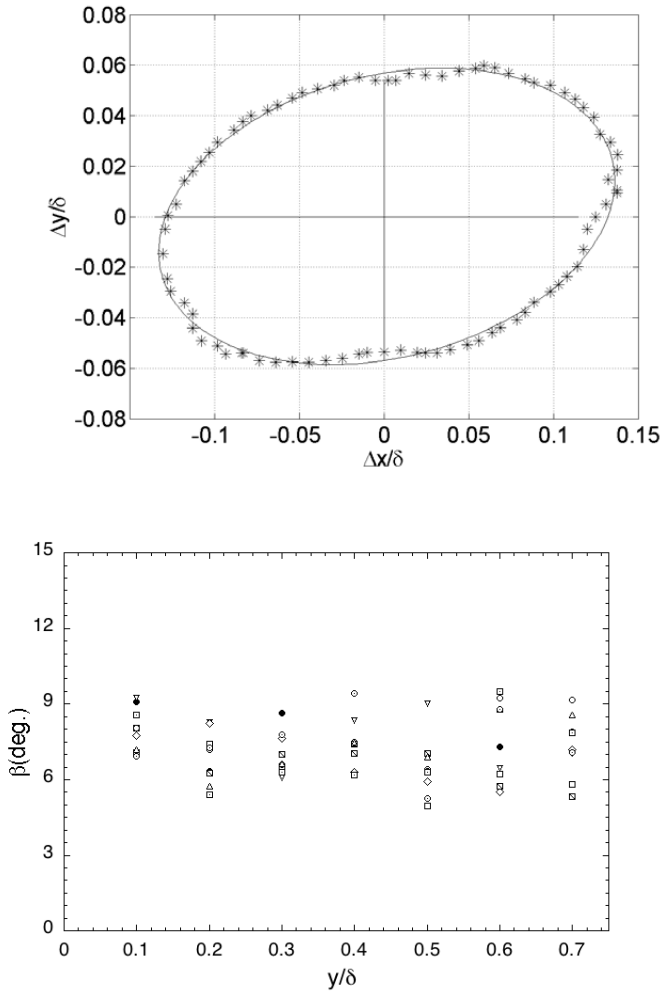


Figure 4.15: Inclination angle of R_{uu} . Symbols: \bullet $X=0$, ∇ 0.2, \square 0.7, \diamond 1.2, \boxtimes 1.7, \triangle 2.2, \circ 2.7, \boxdot 3.2, \odot 5.66.

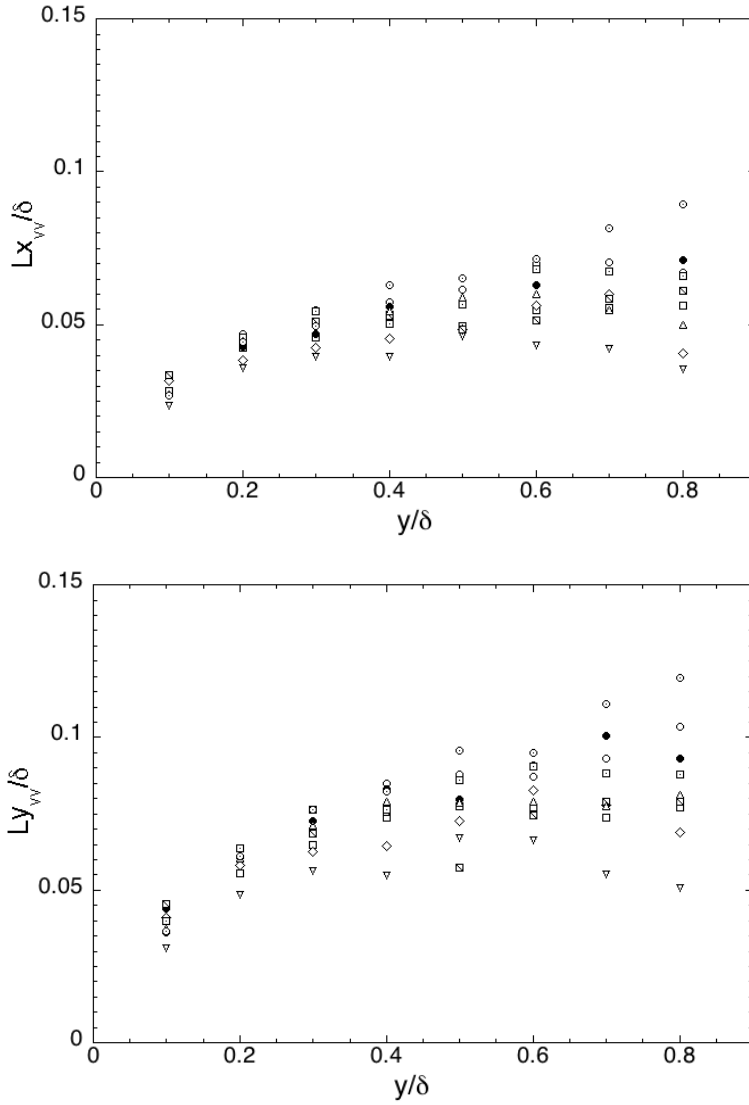


Figure 4.16: Streamwise extent of $R_{vv} = 0.7$. Symbols: \bullet $X=0$, ∇ 0.2, \square 0.7, \diamond 1.2, \boxtimes 1.7, \triangle 2.2, \odot 2.7, \boxdot 3.2, \ominus 5.66.

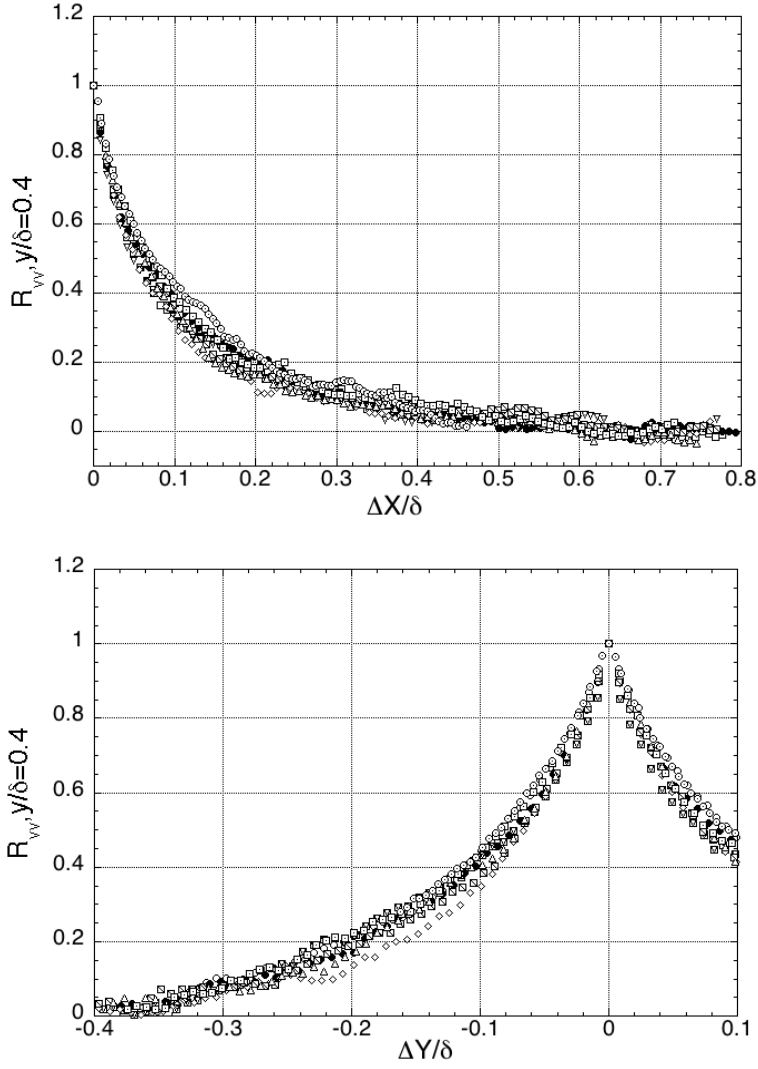


Figure 4.17: One dimensional profiles of R_{vv} . Symbols: \bullet $X=0$, ∇ 0.2, \square 0.7, \diamond 1.2, \square 1.7, \triangle 2.2, \circ 2.7, \boxtimes 3.2, \odot 5.66.

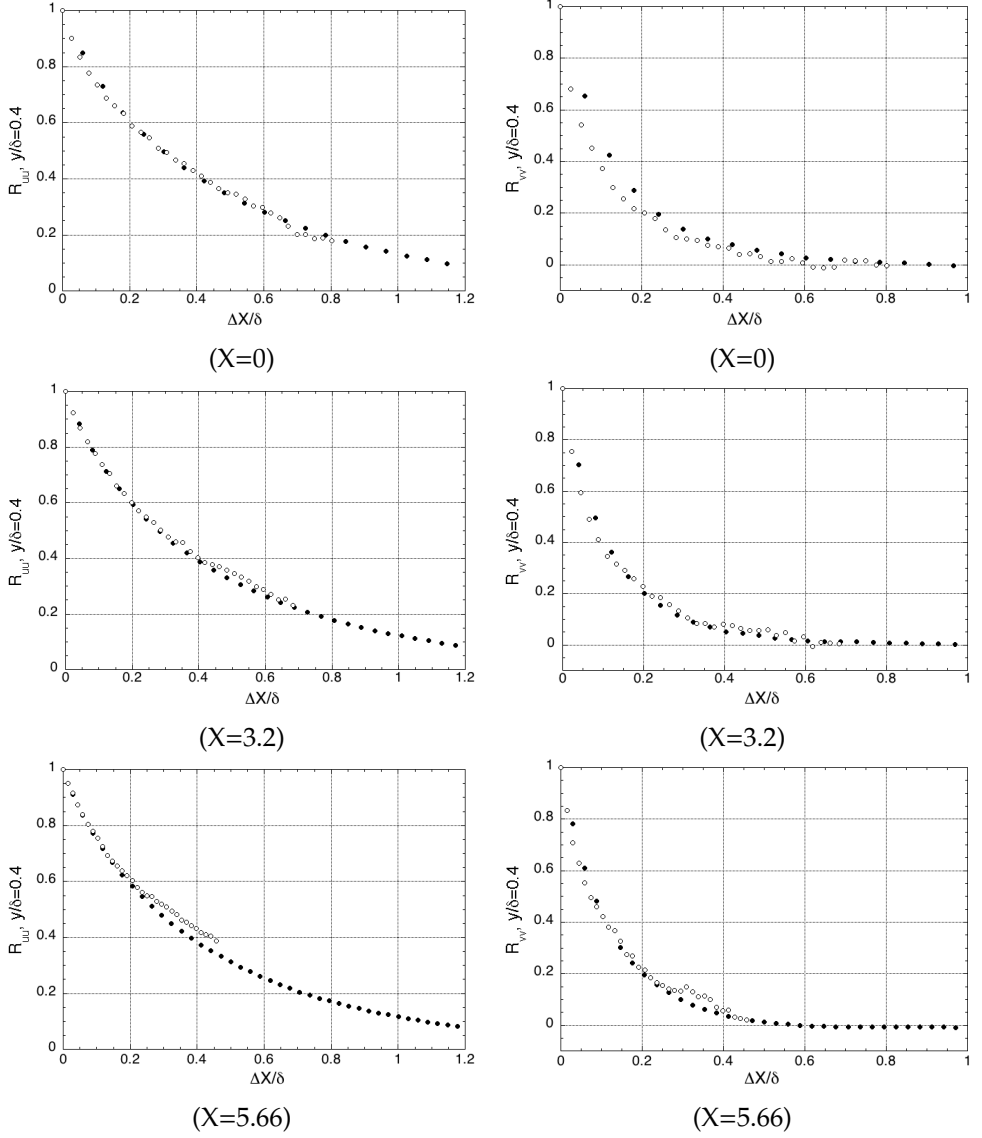


Figure 4.18: The R_{uu} and R_{vv} obtained from PIV and LDA, for $y/\delta = 0.4$. • LDA measurements, ◦ PIV measurements.

4.2.4 Swirling Strength

Chong & Perry (1990) showed that the characteristic equation (4.2) represents the best way to identify the various streamline patterns that can occur in a three-dimensional flows.

$$\lambda^3 + P\lambda^2 + Q\lambda + R = 0 \quad (4.2)$$

where:

$$\begin{aligned} P &= -S_{ii} \equiv 0 \Rightarrow \text{incompressible flow} \\ Q &= \frac{1}{2} (P^2 - S_{ij}S_{ij} - R_{ij}R_{ij}) \\ R &= \frac{1}{3} (-P^3 + 3PQ - S_{ij}S_{jk}S_{ki} - 3R_{ij}R_{jk}S_{ki}) \\ S_{ij} &= \frac{1}{2} \left(\frac{\partial u_i}{\partial x_j} + \frac{\partial u_j}{\partial x_i} \right) \\ R_{ij} &= \frac{1}{2} \left(\frac{\partial u_i}{\partial x_j} - \frac{\partial u_j}{\partial x_i} \right) \end{aligned}$$

The characteristic equation has many solutions but we are interested only when we have one real root (λ_r) and a conjugate pair of complex roots ($\lambda_c + \lambda_{ci}$). When (λ_r) > 0, Chong & Perry (1990) demonstrated that the motion of a particle is a spiral motion.

The solution above is based on a three-dimensional flow field, the PIV velocity fields obtained are only 2D. The solution came from Adrian *et al.* (2000); they computed a two-dimensional form based on the PIV data.

$$\begin{vmatrix} \frac{\partial u}{\partial x} - \lambda & \frac{\partial u}{\partial y} \\ \frac{\partial v}{\partial x} & \frac{\partial v}{\partial y} - \lambda \end{vmatrix} = 0 \quad (4.3)$$

From which we obtain the solution:

$$\lambda = \frac{1}{2} \left(\frac{\partial u}{\partial x} + \frac{\partial v}{\partial y} \right) + \frac{1}{2} \sqrt{\left(\frac{\partial u}{\partial x} + \frac{\partial v}{\partial y} \right)^2 - 4 \left(\frac{\partial u}{\partial x} \frac{\partial v}{\partial y} - \frac{\partial u}{\partial y} \frac{\partial v}{\partial x} \right)} \quad (4.4)$$

$$\lambda = \frac{1}{2} \left(\frac{\partial u}{\partial x} + \frac{\partial v}{\partial y} \right) + \frac{1}{2} \sqrt{\left(\frac{\partial u}{\partial x} - \frac{\partial v}{\partial y} \right)^2 + 4 \left(\frac{\partial u}{\partial y} \frac{\partial v}{\partial x} \right)} \quad (4.5)$$

Swirling strength λ_{ci} is defined as the imaginary part of λ ,

$$\lambda_{ci} = \frac{1}{2} \sqrt{\left| \left(\frac{\partial u}{\partial x} - \frac{\partial v}{\partial y} \right)^2 + 4 \left(\frac{\partial u}{\partial y} \frac{\partial v}{\partial x} \right) \right|} \quad (4.6)$$

The advantage with the swirling strength is that it does not detect regions of shear stress that have no rotation. The swirling strength does not give the sense

of rotation, λ_{ci} is positive by definition, a sign can be assigned based on the sign of the local vorticity,

$$\lambda_s = \lambda_{ci} \left(\frac{\omega_z}{|\omega_z|} \right) \quad (4.7)$$

Contours of swirling strength, λ_{ci} , can be interpreted as representing the vortex cores (Adrian *et al.* 2000). The outermost contour of $R_{\lambda\lambda}$ can be defined as a representative length scale of largest vortex cores (Ganapathisubramani *et al.* 2006). Figure (4.19) and Figure (4.20) present contours of $R_{\lambda\lambda}$ in $x-y$ plane. Figures (4.19) and (4.20) show the resolution problem, due to the high Reynolds number and the large field of view, the vortex cores are not fully resolved. The shape or size of the the $R_{\lambda\lambda}$ contours, except $X = 5.66 m$, are seen to be unaffected by increasing the length, X , of rough surface. The visual analysis reveal that the contours of $R_{\lambda\lambda}$ for $X = 5.66 m$ has shrunk compared with smooth surface. If this is due to roughness or high Reynolds number is not yet clear. The Reynolds number for $X = 5.66 m$ is twice than for $X = 0$. According to Head & Bandyopadhyay (1981) hypothesis, the vortices become skinnier (stretched) when increasing the Reynolds number. For $(Re_\theta)_{rough} = 4260$ and $(Re_\theta)_{smooth} = 6069$, Volino *et al.* (2009), found that the spatial extensions was larger in two-dimensional roughness than on smooth surface. The streamwise and wall normal slices of $R_{\lambda\lambda}$ for $y/\delta = 0.4$, outer- and inner-scaled, are depicted in Figure (4.21). Scaling in outer variable underline the reduction of $R_{\lambda\lambda}$ for $X = 5.66 m$.

Inner-scaled $R_{\lambda\lambda}$ shows a good agreement for $X > 0$ in both directions indicating that the size of vortices scales with viscous variables, ν/u_τ . Calier & Stanislas (2005), for smooth-surface, come to conclusion that all the physical characteristics of the vortices, in log-law region, scale in wall units. The differences noticed in Figure (4.21), inner-scaled $R_{\lambda\lambda}$, between $X = 0$ and $X > 0$ may be explained as follows:

- the scatter in measurements due to the resolution problem and background noise
- the size of vortices, for smooth-surface, do not scale on inner variables outside the logarithmic region
- the vortices, $X > 0$, are produced in the wall region and transported in the outer region

The extent of $R_{\lambda\lambda}$, $Lx_{\lambda\lambda}$ and $Ly_{\lambda\lambda}$, are presented in Fig. (4.22). The extent of $R_{\lambda\lambda}$ in streamwise direction and wall-normal direction has the largest value for $X = 0$ and the smallest value for $X = 5.66 m$. The difference is decreasing when increasing the y/δ . The effect of increasing the length, X , of rough surface is a decrease in the extent of $R_{\lambda\lambda}$ compared with smooth surface, $X = 0$. The results are in agreement with Volino *et al.* (2007) but not with Volino *et al.* (2009).

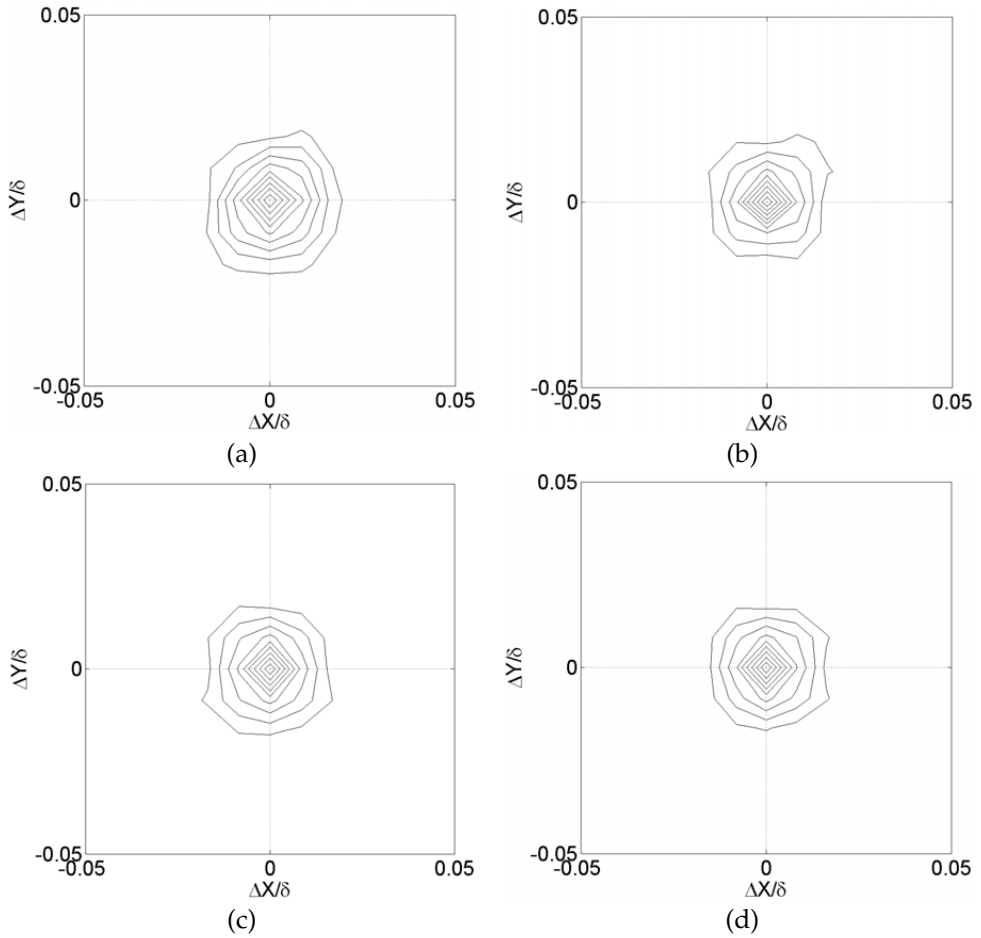


Figure 4.19: Contours of $R_{\lambda\lambda}$ for $y/\delta = 0.4$, outermost contour $R_{\lambda\lambda} = 0.1$, contour spacing 0.1, a) $X = 0$, b) $X = 0.2$, c) $X = 0.7$, d) $X = 1.2$

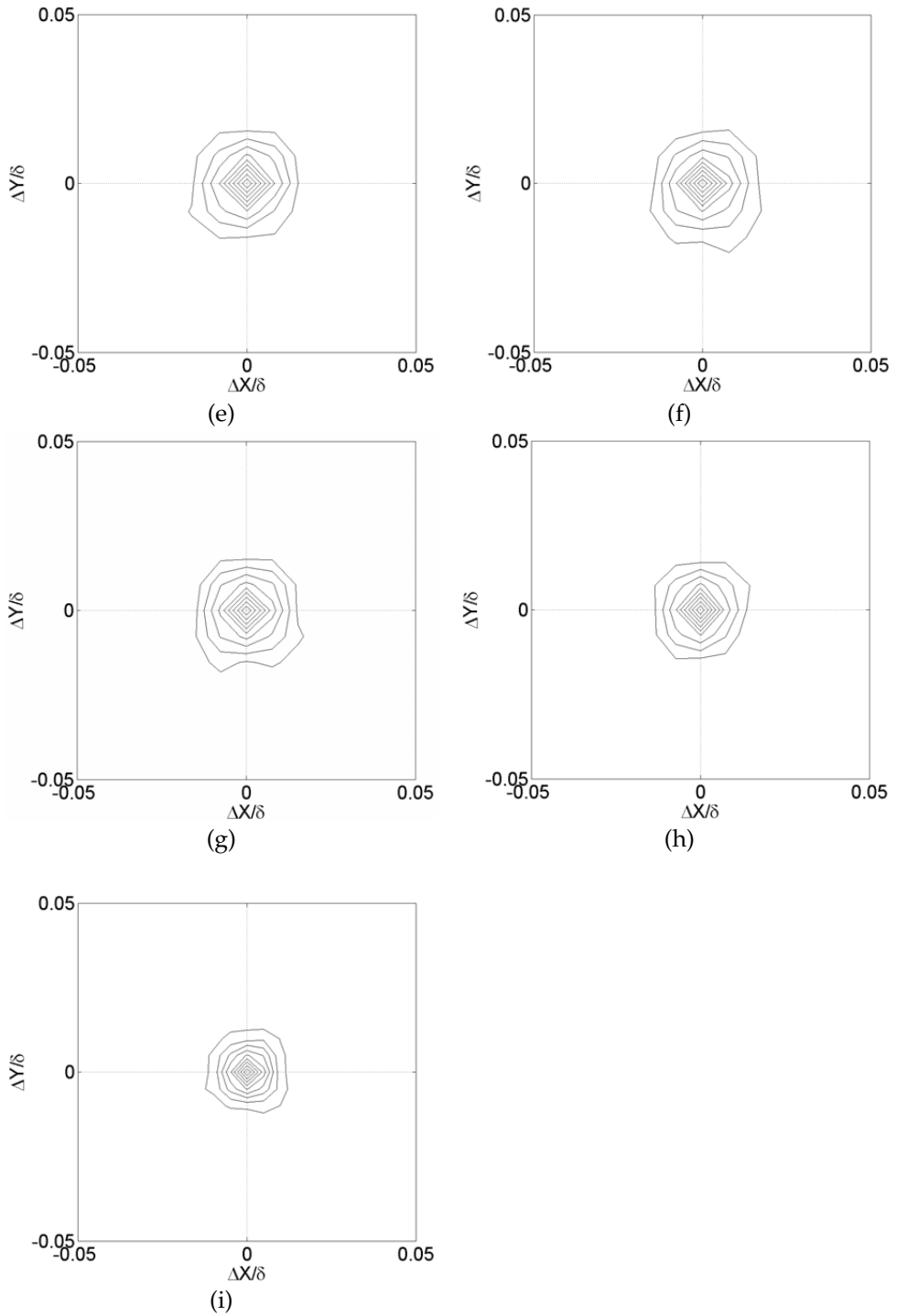


Figure 4.20: Contours of $R_{\lambda\lambda}$ for $y/\delta = 0.4$, outermost contour $R_{\lambda\lambda} = 0.1$, contour spacing 0.1, e) $X = 1.7$, f) $X = 2.2$, g) $X = 2.7$, h) $X = 3.2$, i) $X = 5.66$

CHAPTER 4. TURBULENT BOUNDARY LAYER OVER A STEP CHANGE:
SMOOTH TO ROUGH. PIV MEASUREMENTS

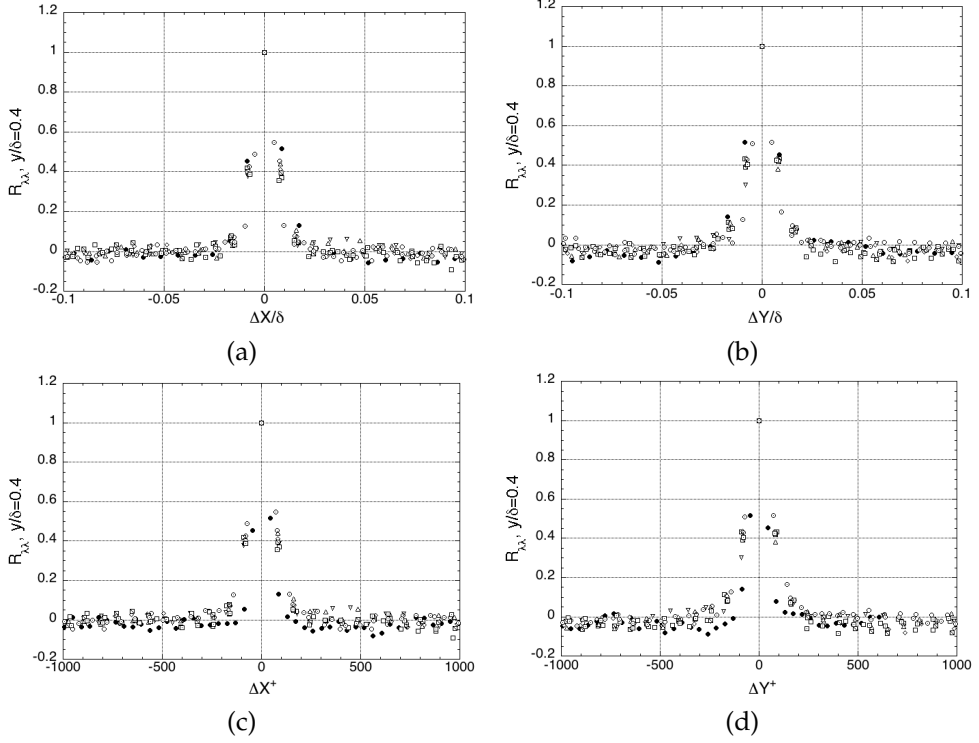
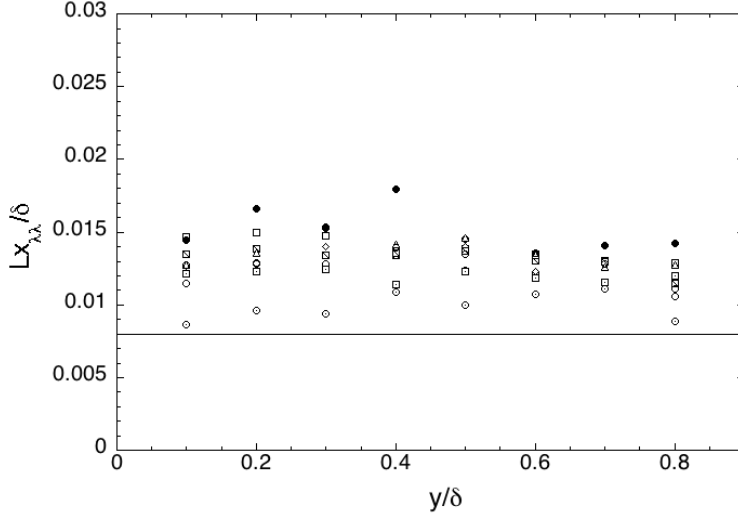
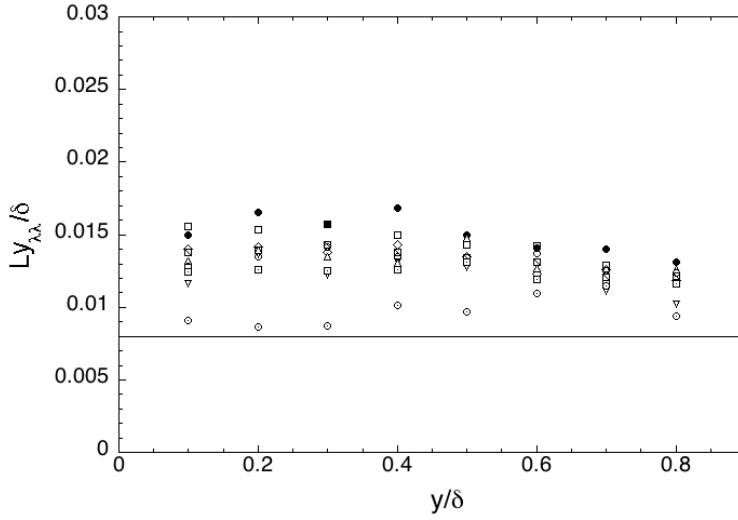


Figure 4.21: Swirling strength correlation coefficients $R_{\lambda\lambda}$ for $y/\delta = 0.4$ in the $x - y$ plane, (a – b) outer-, (c – d) inner-scaled. Symbols: \bullet $X=0$, ∇ 0.2, \square 0.7, \diamond 1.2, \boxplus 1.7, \triangle 2.2, \circ 2.7, \boxminus 3.2, \odot 5.66.



(a)



(b)

Figure 4.22: Streamwise and wall-normal extent of $R_{\lambda\lambda}$ for $y/\delta = 0.4$. Symbols: \bullet $X=0$, ∇ 0.2, \square 0.7, \diamond 1.2, \boxtimes 1.7, \triangle 2.2, \circ 2.7, \boxdot 3.2, \odot 5.66. The solid line is $k/\delta = 0.008$ for $X = 5.66$.

4.2.5 Proper orthogonal decomposition analysis

The main conclusion from two point correlations is that the roughness has little effect on the small scales. To study further the effect of roughness on the small and large scales of the flow we will use POD analysis. Proper orthogonal decomposition (POD) is an effective tool to identify the dominant features in a flow. The method of snapshots is used, as it is more suitable for the PIV measurements. The snapshot POD has the advantage of being computationally efficient as it reduces the order of the eigenvalue problem to that of the number of snapshots and not the physical mesh (Sen *et al.* (2007)). Following the J. M. Pedersen (2003) and J. Kostas *et al.* (2005), POD is a technique based on the two-point velocity correlation, the goal is to find an orthogonal decomposition for a random vector based on a POD modes ϕ_i satisfying the orthonormality condition. Mathematically this can be expressed as:

$$u(x, y, t) = \sum_{j=1}^M a^{(j)} \phi^{(j)}(x, y) \quad (4.8)$$

Consider the u and v the fluctuating velocity. Based on u and v a matrix U (see J M Pedersen (2003)) can be constructed:

$$U = \begin{bmatrix} u_1^{(1)} & u_1^{(2)} & \cdots & u_1^{(M)} \\ u_2^{(1)} & u_2^{(2)} & \cdots & u_2^{(M)} \\ \vdots & \vdots & \ddots & \vdots \\ u_{lm}^{(1)} & u_{lm}^{(2)} & \cdots & u_{lm}^{(M)} \\ v_1^{(1)} & v_1^{(2)} & \cdots & v_1^{(M)} \\ v_2^{(1)} & v_2^{(2)} & \cdots & v_2^{(M)} \\ \vdots & \vdots & \ddots & \vdots \\ v_{lm}^{(1)} & v_{lm}^{(2)} & \cdots & v_{lm}^{(M)} \end{bmatrix} \quad (4.9)$$

where M is the number of snapshots, l, m number of velocity components in a snapshot. A correlation matrix, from the matrix U , can be calculated as

$$\mathbf{C} = \frac{1}{M} \mathbf{U}^T \cdot \mathbf{U} \quad (4.10)$$

and the eigenvalue problem can be written

$$\mathbf{C} \cdot \mathbf{A} = \lambda \cdot \mathbf{A} \quad (4.11)$$

Solving the equation and ordering solutions descending:

$$\lambda^{(1)} > \lambda^{(2)} > \cdots > \lambda^{(M)} = 0 \quad (4.12)$$

The eigenvalues λ_i are real and positive and represents contribution to the turbulent kinetic energy of mode ϕ_i .

$$E = \sum_{i=1}^M \lambda_i \quad (4.13)$$

where E is twice the turbulent kinetic energy of the flow.

The discrete POD modes of the snapshot POD are calculated as:

$$\phi^{(i)}(x, y) = \frac{\sum_{n=1}^M A_n^{(i)} U(x, y)^n}{\left\| \sum_{n=1}^M A_n^{(i)} U(x, y)^n \right\|}, \quad i = 1, \dots, M \quad (4.14)$$

The expansion coefficients were calculated by projecting the PIV field onto the calculated modes,

$$a^{(n)} = \phi^{(n)T} \cdot U(x, y) \quad (4.15)$$

A reconstruction of velocity field using the N_{POD} leading POD modes can be done as (see Wu & Christensen (2010)):

$$u_L^{(n)}(x, y) = \sum_{i=1}^{N_{POD}} a_i^{(n)} \phi_i^{(n)}(x, y) \quad (4.16)$$

and residual field,

$$u_R^{(n)}(x, y) = \sum_{i=N_{POD}+1}^M a_i^{(n)} \phi_i^{(n)}(x, y) = u^{(n)}(x, y) - u_L^{(n)}(x, y) \quad (4.17)$$

Results POD

The analysis is carried out for the near wall region, $y/\delta < 0.5$ for $X \leq 3.2m$ and $y/\delta < 0.3$ for $X = 5.66m$, using 2500 instantaneous flow fields. Figure (4.23(a)) presents the fractional energy distribution, calculated with equation (4.18).

$$E_i = \frac{\lambda_i}{\sum_{j=1}^M \lambda_j} \cdot 100\% \quad (4.18)$$

The lower modes which are the most energetic modes are associated with the large scale in the flow, and the higher modes are less energetic modes, and correspond to small scales. The fractional energy distributions over the first 10 modes for all cases is presented in Tabel (4.18). The first mode gives the largest contribution to the energy. There is no clear effect of increasing the length, X , of rough surface on the fractional energy content for the first mode when $X \leq 2.7$ except for $X = 0.2$ where a decrease of $\sim 15\%$ on the fractional energy is noticed. For $X \geq 3.2$ there is an increase of $\sim 11\%$ for $X = 3.2m$ and $\sim 40\%$ for $X = 5.66m$.

Figure (4.23(b)) depicts the distribution of the cumulative energy defined as:

$$(\text{cumulative energy})_m = \sum_{j=1}^m E_j \quad (4.19)$$

calculated from the fractional energy Figure (4.23(a)). The first six modes for $0 < X < 2.7$ and four modes for $X > 2.7$ capture around 50% of the resolved

Table 4.18: Fractional energy contribution to the first 10 POD modes

Mode	X								
	0.00	0.2	0.7	1.2	1.7	2.2	2.7	3.2	5.66
1	0.260	0.227	0.277	0.270	0.260	0.276	0.259	0.289	0.366
2	0.108	0.108	0.099	0.100	0.104	0.109	0.103	0.106	0.098
3	0.049	0.049	0.048	0.053	0.053	0.053	0.050	0.054	0.049
4	0.042	0.039	0.041	0.044	0.045	0.042	0.039	0.040	0.038
5	0.023	0.029	0.028	0.028	0.030	0.026	0.025	0.027	0.024
6	0.021	0.022	0.022	0.022	0.022	0.023	0.021	0.022	0.023
7	0.019	0.019	0.020	0.021	0.021	0.021	0.018	0.019	0.017
8	0.014	0.015	0.016	0.015	0.015	0.014	0.014	0.015	0.016
9	0.013	0.014	0.013	0.014	0.014	0.013	0.013	0.013	0.013
10	0.012	0.012	0.012	0.012	0.013	0.013	0.013	0.013	0.012

energy. The first ~ 700 modes are needed to capture 95% of the resolved energy for $X = 0$ and $X = 3.2m$. Using POD for turbulent boundary layer, over smooth surface at $Re_\theta = 12000$, Wu & Christensen (2010) found that the first six modes and more than 400 modes were necessary to capture 50% and 95% of the resolved energy. This points out the resolution problem and the inability of the system to capture the small scales.

A useful aspect of the POD is possibility to separate the flow in large and small scales. This enables us to study the effect of roughness on large and small scales separately. Large-scale flow fields are reconstructed using the equation (4.16) and the small scales, or residual, flow fields are generated using the equation (4.17). The large-scale flow fields are based on the number of modes, N , necessary to reconstruct 50% of energy, thus six modes were necessary to reconstruct the flow fields for the smooth case ($X = 0$) and four modes for $X = 3.2m$. The small-scale flow fields are reconstructed starting with the mode $N + 1$ until the mode necessary to reconstruct the remaining 49% of energy. Thus the total reconstructed fluctuating flow contains 99% of the resolved energy. Figure (4.24) and Figure (4.25) presents, random selected, large- and small-scale representations of fluctuating velocity field for $X = 0$ and $X = 3.2m$. Visual examinations does not give any quantitative information regarding to what happens to the flow structure when we increase the length X of the rough surface. A solution is to calculate contribution of large and small-scales to the Reynolds stresses separately.

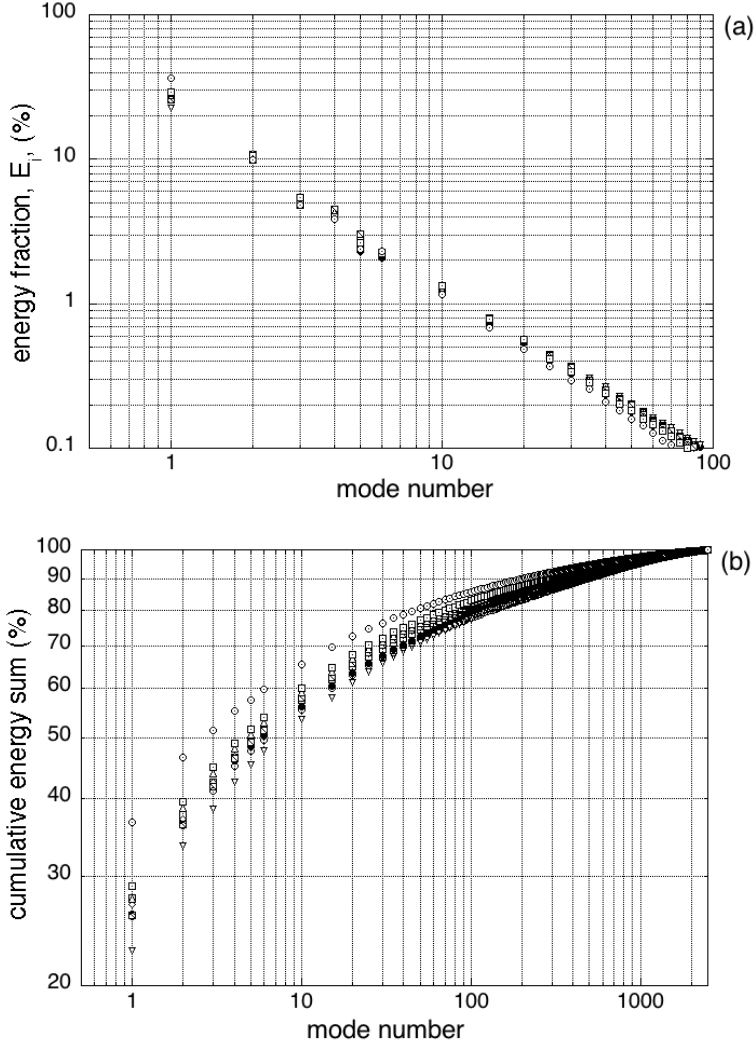


Figure 4.23: POD energy. (a) Fractional contribution of each mode (b) Cumulative energy distribution. Symbols: \bullet $X=0$, ∇ 0.2, \square 0.7, \diamond 1.2, \boxtimes 1.7, \triangle 2.2, \circ 2.7, \boxdot 3.2, \odot 5.66. Not every mode is shown for clarity (1 – 6, 11, 16, 21, \dots)

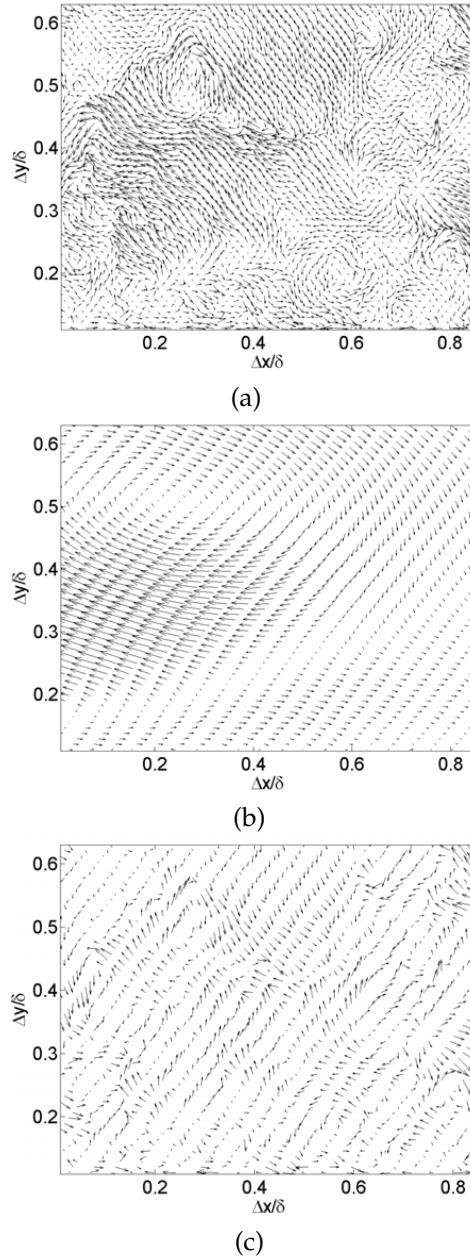


Figure 4.24: (a) fluctuating velocity field for $X=0$ (b) large-scale representation of (a) (projected on the first six modes). (c) small scale representation of (a) (projected on 7-1724 modes). Not every vector is shown.

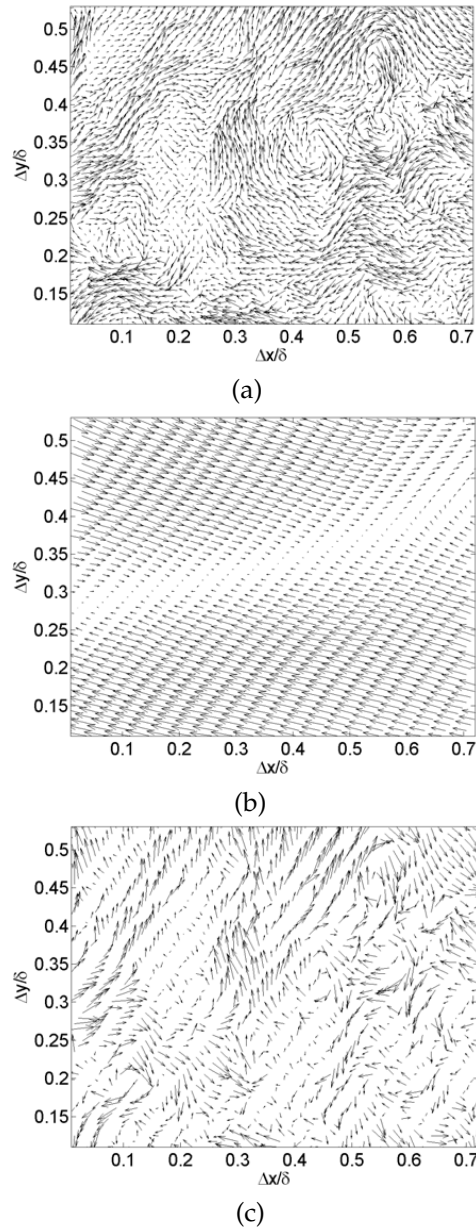


Figure 4.25: (a) fluctuating velocity field for $X=3.2$ (b) large-scale representation of (a) (projected on the first four modes). (c) small scale representation of (a) (projected on 5-1751 modes). Not every vector is shown.

Figure (4.26) presents the profiles of $\langle uu \rangle^+$ and $\langle vv \rangle^+$, obtained from PIV measurements; calculated from POD, using equation (4.16), by recovering 50% of energy and the profiles associated with small scales using equation (4.17). The energy recovered in large and small scales contains 99% of the total energy.

The contribution to the $\langle uu \rangle^+$ is dominated by large scales for $y/\delta > 0.1$ while the small scales dominate the near wall region, $y/\delta < 0.1$. For smooth surface at $y/\delta = 0.2$ the contribution of large scales represents $\sim 70\%$ while at $y/\delta = 0.02$ it represents only $\sim 35\%$. The main contribution to the $\langle vv \rangle^+$ is due to the small scales and only $\sim 20\%$ is due to the large scales. This is in agreement with Wu & Christensen (2010). The large and small scales show no effect on the outer layer.

A qualitative evaluation of the character of flow structure is obtained through the two-point correlations. Figure (4.27) to Figure (4.29) present the contours of two-point correlations, streamwise and wall-normal component, for $X = 0, 0.2, 3.2$. The $(R_{uu})_L$, computed from large scales, is similar in shape to the R_{uu} , computed from PIV, but is more elongated in streamwise direction. The $(R_{uu})_R$, residual or computed from the small scales, is more compact than (R_{uu}) and has a streamwise extension similar to R_{vv} . The inclination angle for $(R_{uu})_R$ is zero.

The $(R_{vv})_R$ has a shape similar to the R_{vv} but less elongated in streamwise direction, $\sim 25\%$ less for $X = 0$.

Figure (4.30) presents the one-dimensional profiles for R_{uu} and R_{vv} , in streamwise direction computed from PIV ($a - b$), large scales POD ($c - d$) and small scales POD ($e - f$). The $(R_{uu})_L$ shows small differences when increasing the length X of rough surface. The $(R_{vv})_L$ is reduced when increasing the length X of rough surface. The small-scale correlation $(R_{vv})_R$ is similar to (R_{vv}) indicating that the main contribution to v component is due to the small scales. Further the streamwise $(R_{vv})_L$ falls below zero and rises again to reach a second top.

Wall-normal correlation coefficients are presented in Figure (4.31). The R_{uu} and R_{vv} for large and small scales, in wall normal direction, show no differences with increasing the length, X , of rough surface.

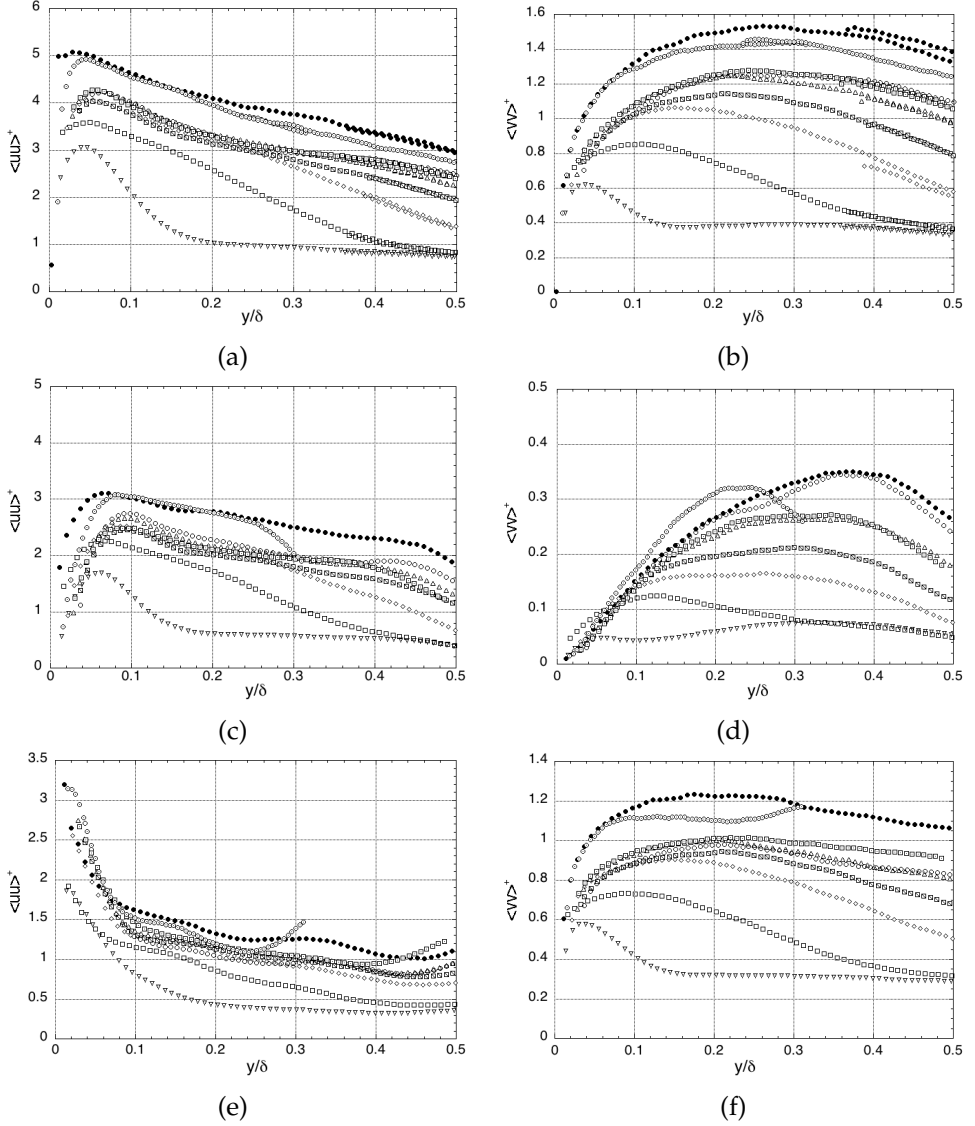


Figure 4.26: Comparison of Reynolds stresses obtained from PIV and POD modes, a) $\langle uu^+ \rangle$, b) $\langle vv^+ \rangle$ from PIV; c) $\langle uu^+ \rangle$, d) $\langle vv^+ \rangle$ recalculated from POD by recovering 50% of energy; e) $\langle uu^+ \rangle$, f) $\langle vv^+ \rangle$ residual velocity field (small scales). Symbols: \bullet $X=0$, ∇ 0.2, \square 0.7, \diamond 1.2, \boxtimes 1.7, \triangle 2.2, \odot 2.7, \boxdot 3.2, \ominus 5.66.

CHAPTER 4. TURBULENT BOUNDARY LAYER OVER A STEP CHANGE:
SMOOTH TO ROUGH. PIV MEASUREMENTS

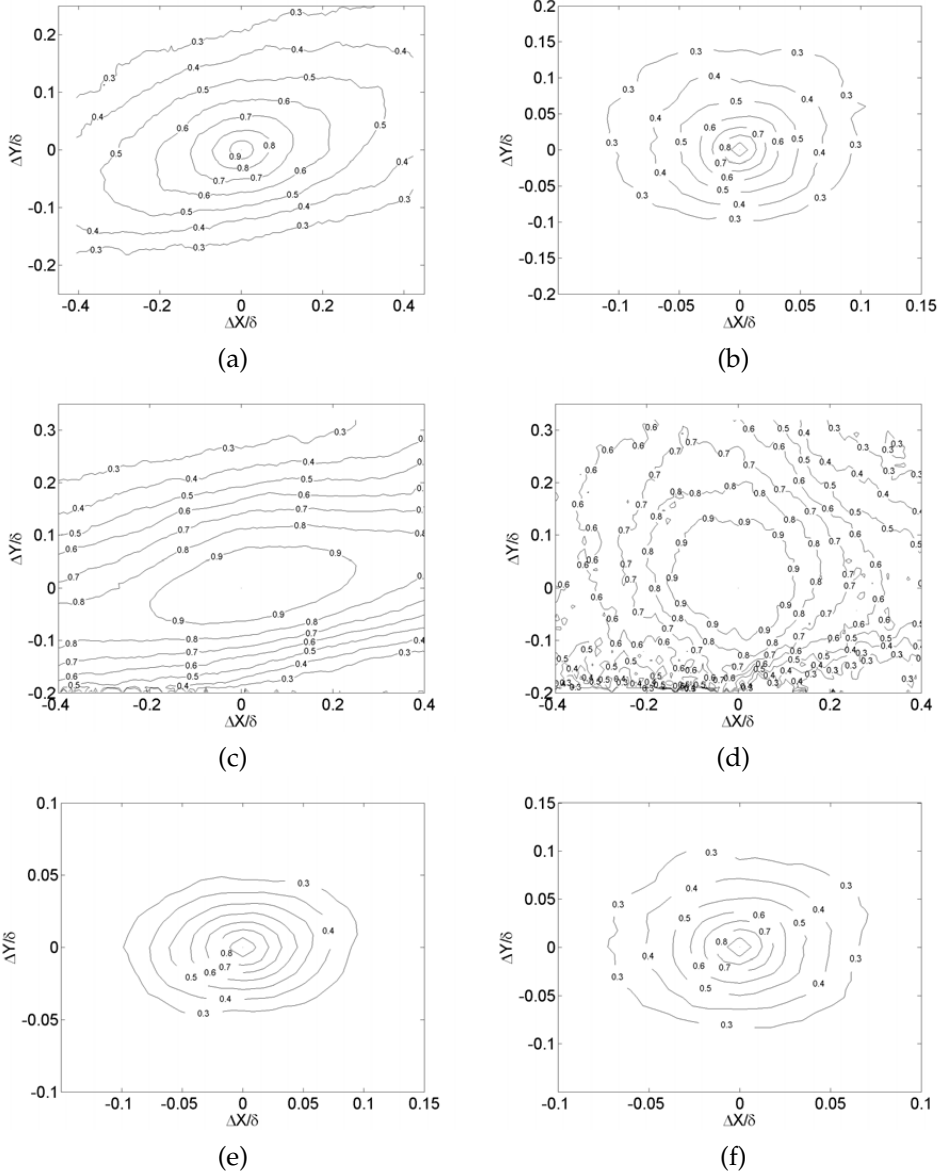


Figure 4.27: Contours of (a) R_{uu} (b) R_{vv} (c) $(R_{uu})_L$ (d) $(R_{vv})_L$ (e) $(R_{uu})_R$ (f) $(R_{vv})_R$ for $X = 0$ at $y/\delta = 0.2$.

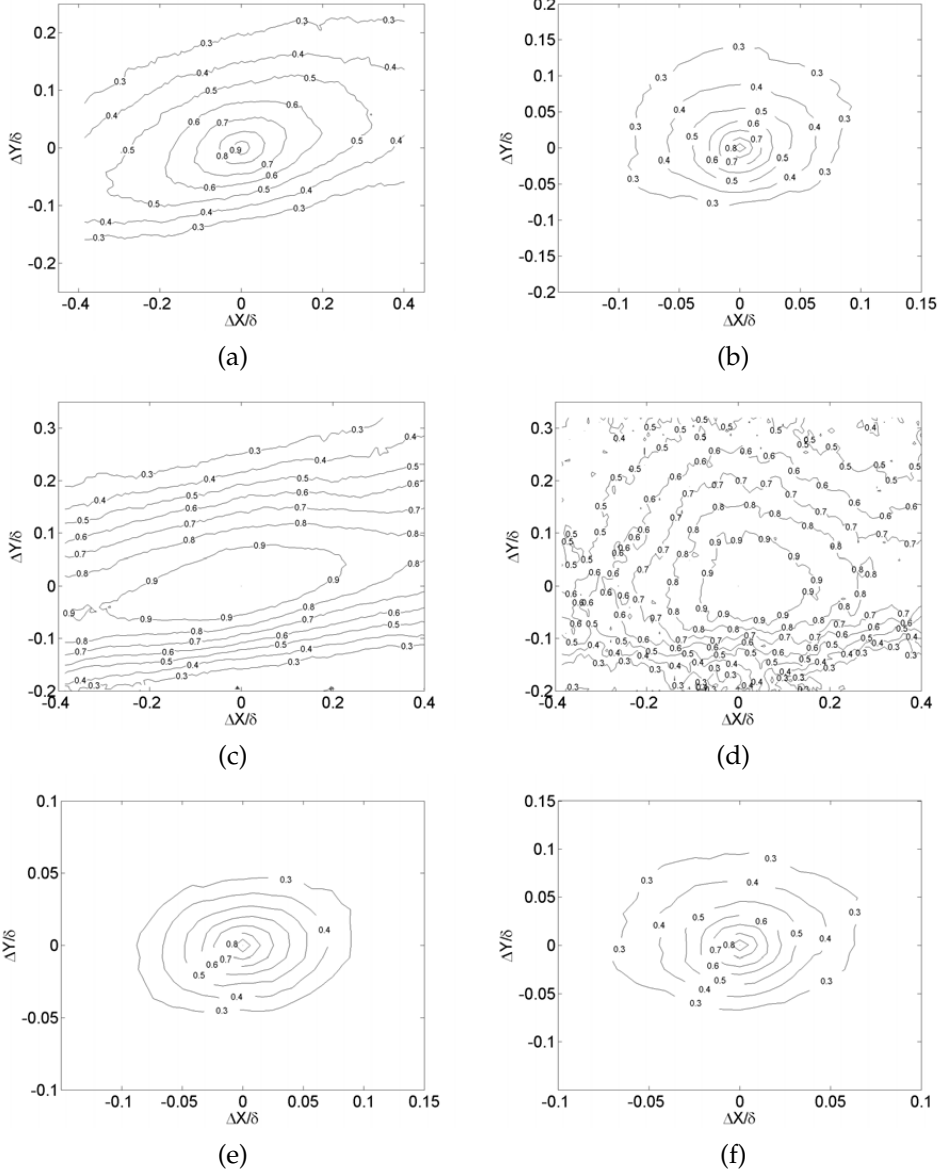
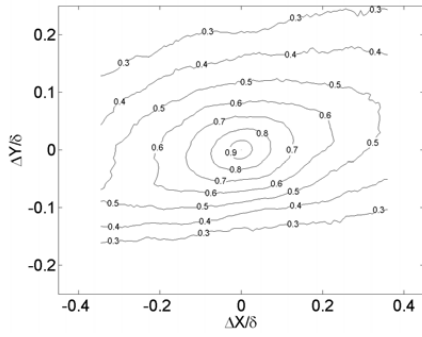
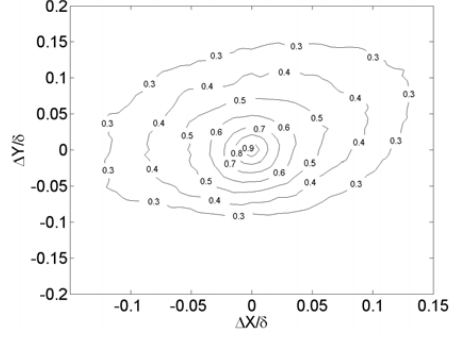


Figure 4.28: Contours of (a) R_{uu} (b) R_{vv} (c) $(R_{uu})_L$ (d) $(R_{vv})_L$ (e) $(R_{uu})_R$ (f) $(R_{vv})_R$ for $X = 0.2$ at $y/\delta = 0.2$.

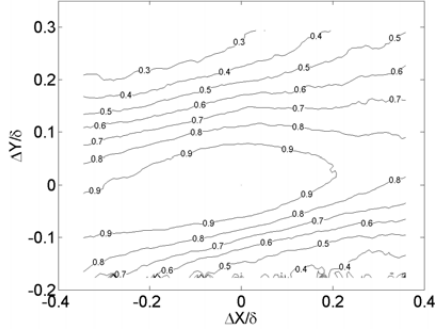
CHAPTER 4. TURBULENT BOUNDARY LAYER OVER A STEP CHANGE:
SMOOTH TO ROUGH. PIV MEASUREMENTS



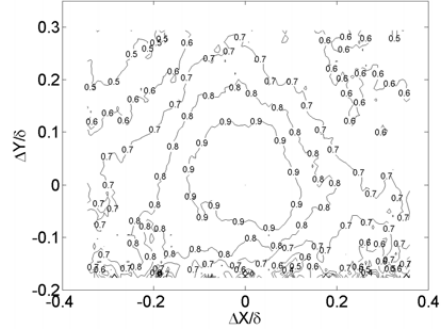
(a)



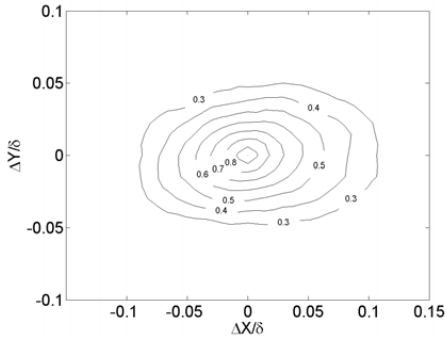
(b)



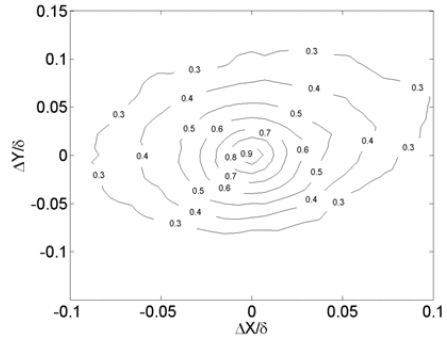
(c)



(d)



(e)



(f)

Figure 4.29: Contours of (a) R_{uu} (b) R_{vv} (c) $(R_{uu})_L$ (d) $(R_{vv})_L$ (e) $(R_{uu})_R$ (f) $(R_{vv})_R$ for $X = 3.2$ at $y/\delta = 0.2$.

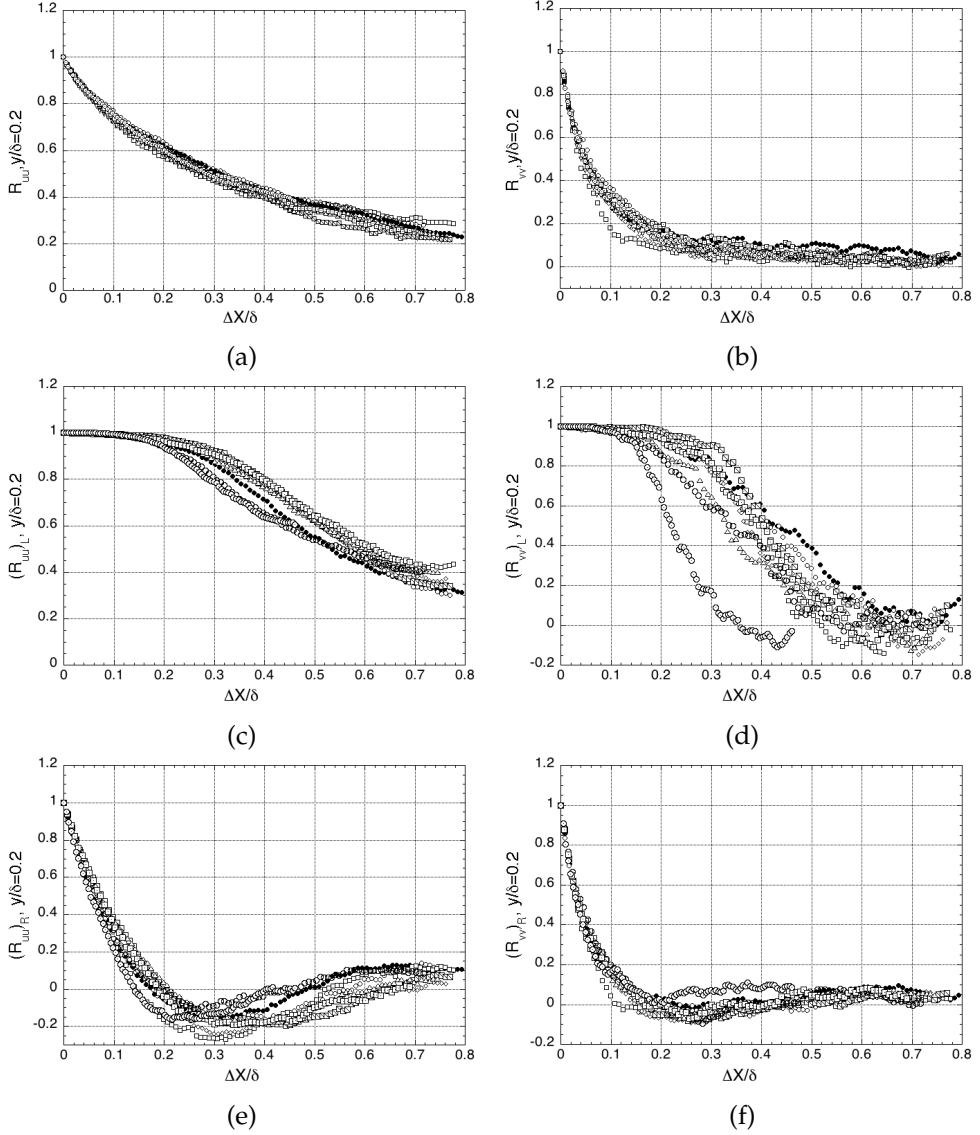


Figure 4.30: Streamwise velocity correlation, R_{uu} and R_{vv} , at $y/\delta = 0.2$. Symbols:
 • $X=0$, ∇ 0.2, \square 0.7, \diamond 1.2, \boxtimes 1.7, \triangle 2.2, \circ 2.7, \boxdot 3.2, \odot 5.66.

CHAPTER 4. TURBULENT BOUNDARY LAYER OVER A STEP CHANGE:
SMOOTH TO ROUGH. PIV MEASUREMENTS

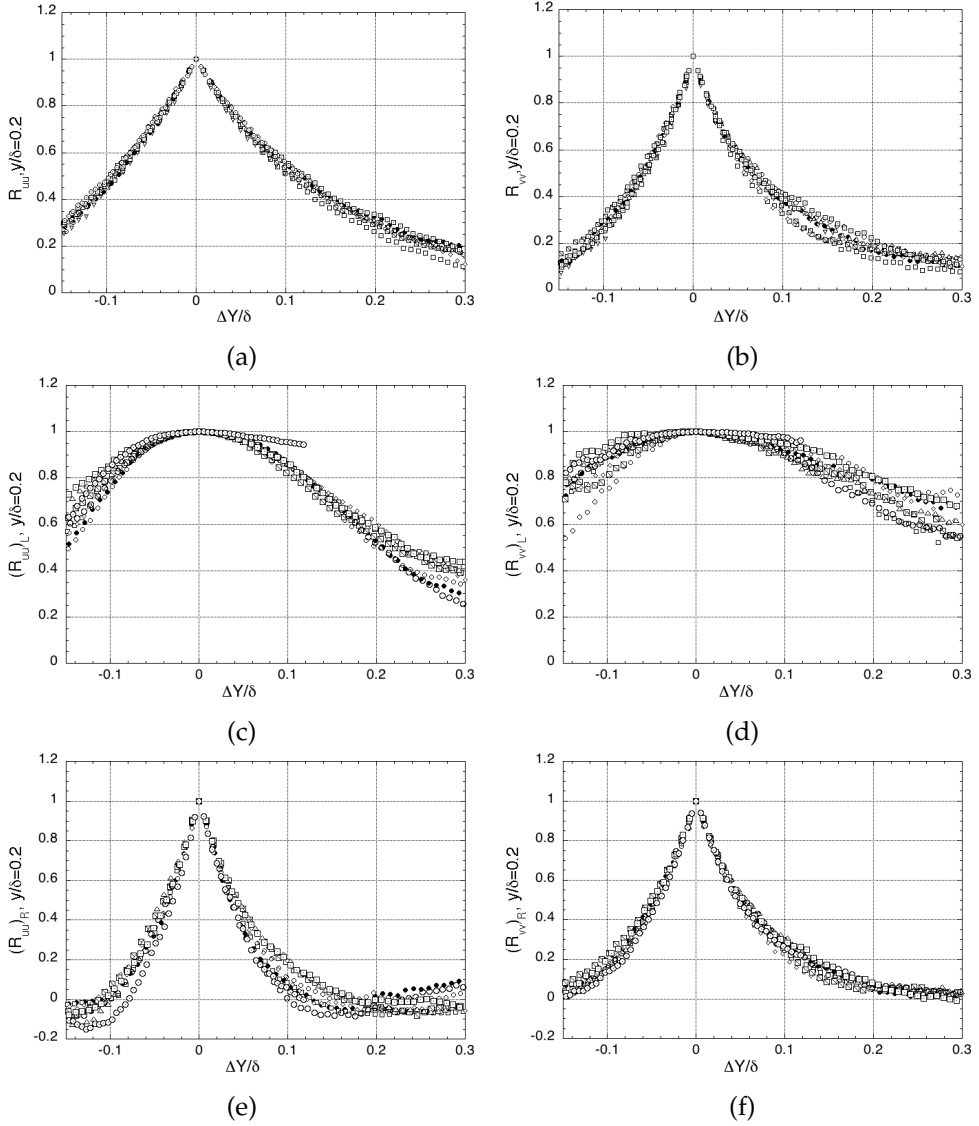


Figure 4.31: Wall-normal correlation, R_{uu} and R_{vv} , at $y/\delta = 0.2$. Symbols: \bullet $X=0$, ∇ 0.2, \square 0.7, \diamond 1.2, \boxplus 1.7, \triangle 2.2, \circ 2.7, \boxtimes 3.2, \odot 5.66.

4.2.6 Conclussions

An experimental study of the response of a turbulent boundary layer to a smooth-to-rough change in surface condition was carried out using a PIV. The results are focused on the spatial structure of the flow in the $x - y$ plane.

Increasing the length X of rough surface does not seem to affect the two point correlations, R_{uu} and R_{vv} . The inclination angle of the flow structure is similar to all surfaces which indicates that increasing X will not affect the alignment of the flow structure. Further, the swirling strength correlation, $R_{\lambda\lambda}$, is slightly affected by the X . The increases of X , decreases the extent of $R_{\lambda\lambda}$ at $y/\delta = 0.4$ in streamwise and wall-normal direction.

Possibility of decomposing flow into large and small scales using POD has revealed only incomplete answers due to resolution problem in the near wall region. The two-point correlations of large scales at $y/\delta = 0.2$ indicate that the streamwise extension of v component is reduced by increasing the length, X , of rough surface. The correlations for small scales are almost unchanged in the presence of the roughness.

4.3 References

- M. K. Shah, M. Agelinchaab, M. F. Tachie, Influence of PIV interrogation area on turbulent statistics up to 4th order moments in smooth and rough wall turbulent flows, *Experimental Thermal and Fluid Science* **32**, (2008), pp. 722-747
- P. Saarenrinne, M. Piirto and H. Eloranta, Experiences of turbulence measurement with PIV, *Measurement Science and Technology*, **12**, (2001), pp. 1904-1910
- R. J. Volino, M. P. Schultz and K. A. Flack, Turbulence structure in rough- and smooth-wall boundary layers, *J. Fluid Mech*, **592**, (2007), pp. 263-293
- M. R. Head and P. Bandyopadhyay, New aspects of turbulent boundary-layer structure, *J. Fluid Mech*, **107**, (1981), pp. 297-338
- Y. Wu and K. T. Christensen, Spatial structure of a turbulent boundary layer with irregular surface roughness, *J. Fluid Mech*, **655**, (2010), pp. 380-418
- M. S. Chong and E. Perry, A general classification of three dimensional flow fields, *Physics of Fluids A*, **2**, (5), (1990), pp. 765-777
- R. J. Adrian, K. T. Christensen, Z.-C. Liu, Analysis and interpretation of instantaneous turbulent velocity fields, *Experiments in Fluids* **29**, (2000), pp. 275-290
- R. J. Volino, M. P. Schultz and K. A. Flack, Turbulence structure in a boundary layer with two-dimensional roughness, *J. Fluid Mech*, **635**, (2009), pp. 75-101
- J. M. Pedersen, Analysis of Planar Measurements of Turbulent Flows, *PhD Thesis, Department of Mechanical Engineering, Technical University of Denmark*, (2003)
- J. Kostas, J. Soria, M. S. Chong, A comparison between snapshot POD analysis of PIV velocity and vorticity data, *Experiments in Fluids*, **38**, (2005), pp. 146-160
- M. Sen, K. Bhaganagar and V. Juttijudata, Application of proper orthogonal decomposition (POD) to investigate a turbulent boundary layer in a channel with rough walls, *Journal of Turbulence*, **8**, (41), (2007)
- P.-Å. Krogstad, R. A. Antonia, Surface roughness effects in turbulent boundary layers, *Experiments in Fluids*, **27**, (1999), pp. 450-460
- P.-Å. Krogstad, J. H. Kaspersen, Structure Inclination Angle in a Turbulent Adverse Pressure Gradient Boundary Layer, *Journal of Fluids Engineering*, **124**, (2002), pp. 1025-1033
- K. A. Flack, M. P. Schultz & J. S. Connelly, Examination of a critical roughness height for boundary layer similarity, *Physics of Fluids*, **19**, (2007)
- B. Ganapathisubramani, E. K. Longmire & I. Marusic, Experimental investigation of vortex properties in a turbulent boundary layer, *Physics of Fluids*, **18**, (2006)
- F. N. Frenkiel, On the Kinematics of Turbulence, *Journal of the Aeronautical Sciences*, **15**, (1), (1948),
- J. Carlier and M. Stanislas, Experimental study of eddy structures in a turbulent boundary layer using particle image velocimetry, *J. Fluid Mech*, **535**, (2009), pp. 143-188
- M. Raffel, C. Willert, J. Kompenhans, Particle Image Velocimetry,

A practical Guide, *Springer-Verlag*, (1998)

Chapter 5

Summary and Conclusions

The main goal of this work was to reduce the uncertainty in rough wall measurements by determining independently the skin friction, C_f .

To do this we have build a skin friction balance to measure shear force for rough surface. The skin friction balance is a direct method for measuring skin friction. This is a very accurate method but very difficult to deal with. It took around three years to get good results.

The main source of errors is the pressure variation across the floating element. To investigate this we tested our balance under three different pressure gradients: channel flow, zero pressure gradient boundary layer and adverse pressure gradient (diffuser) flow.

The main conclusions are:

- For channel flow the measured value and the theoretical straight-line distribution are in good agreement. The combined error in pressure measurements and u_τ^2 is around 3%.
- For zero pressure gradient the uncertainty in u_τ^2 is around 4%. The agreement between the analytical curve distribution and measured $-\langle uv^+ \rangle$ is seen to be good.
- For adverse pressure gradient we don't have any analytical distribution for shear stress. We know that the shear stress should extrapolate to one; from the measurements we have this trend.

The balance has proved to be reliable and accurate in different conditions. The C_f measured in adverse pressure gradient is almost half of that over a smooth surface. This suggest that the balance can be used also for zero pressure gradient boundary layer over a smooth surface.

Clauser (1956) associated turbulent boundary layer with a "black box". In order to understand the inner mechanism(s) of the "black box" we can apply different inputs and then measure the outputs.

Using this technique we have applied a step change in roughness, from smooth

to rough, to our boundary layer. The skin friction was measured with the floating element balance and the velocity field was measured using a two component LDA and PIV.

The main conclusions from LDA measurements:

- The mean velocity defect profiles, normalized with u_τ , shows the effect of the wall conditions on the outer layer for $X < 2.2\ m$
- The effect of the wall conditions on Reynolds stresses are not noticed outside the internal boundary layer (IBL).
- The growth of the IBL is proportional with $\delta_i \sim x^{0.73}$ and is in good agreement with the Elliot's formula for growth of the IBL, $\delta_i/z_{02} = 0.37 (X/z_{02})^{0.78}$
- The flow has adapted to new wall conditions both in mean and Reynolds stresses after ~ 18 boundary layer thicknesses over the smooth wall.
- The Reynolds stresses $\langle vv \rangle$ and $\langle -uv \rangle$ normalized with U_e show an overshoot for $X < 2.2\ m$
- Reynolds stresses and higher order moments for $X \geq 2.2\ m$ indicate no differences i outer layer, between smooth and rough-surfaces, providing support for the similarity theory.
- The quadrant analysis indicate similarity between sweep and ejection events for smooth and rough-surfaces, except that they are shifted further from the wall for the rough wall. The ratio between the ejection and sweep events are slightly higher on the smooth surface except from the IBL.

The last measurements are the PIV measurements. The conclusions from PIV are affected by:

- Resolution problem, too high Reynolds number
- Small field of view

The main conclusions from PIV measurements are:

- Increasing the length of the rough surface, X , will not affect the R_{uu} and R_{vv}
- The inclination angle of the flow structure is similar for all surfaces.

The POD decomposition of the flow field has revealed that the large scales have a main contribution to the $\langle uu \rangle$ component while the small scale have a main contribution to the $\langle vv \rangle$ component.

A further investigation of the skin friction balance is required to find the source of the $\sim 4\%$ error. An experiment with a gap less than $\sim 0.6\ mm$ should provide an answer if the source of the error is connected with the dimension of the gap. For

PIV measurements is necessary a camera with better resolution and a better field of view compared with the δ . In our PIV measurements we got only incomplete answers.

Appendix A

List of articles

Article 1: V Efros & P-Å Krogstad "A Skin Friction balance applied to rough wall experiments" *Sixth International Symposium on Turbulence and Shear Flow Phenomena, Seoul, Korea, 22-24 June 2009* Vol II

Article 2: P-Å Krogstad & V Efros "Rough wall skin friction measurements using a high resolution surface balance" *International Journal of Heat and Fluid Flow* 31 (2010) 429-433.